eV- & keV-sterile neutrino studies with KATRIN
–
eV- & keV sterile Neutrino Suche mit KATRIN

Master Thesis of

Marc Korzeczek

at the Department of Physics
Institute for Nuclear Physics (IKP)

Reviewer:	Prof. Guido Drexlin
Second reviewer:	Prof. Ulrich Husemann
Advisor:	Dr. Susanne Mertens
Second advisor:	Dr. Thierry Lasserre

11. May 2015 – 24. May 2016

I declare that I have developed and written the enclosed thesis completely by myself, and have not used sources or means without declaration in the text.

Karlsruhe, 24.5.2016

. . . .

(Marc Korzeczek)

Acknowledgment

I would like to thank

- Susanne Mertens for her excellent support and mentorship during the master's thesis, during my stay at Berkeley, as well as during time as a student assistant in Karlsruhe.
- Thierry Lasserre for his great hospitality at CEA-Saclay and his very motivating guidance throughout the thesis.
- Guido Drexlin who enabled me to study and investigate sterile neutrinos with KATRIN, and always supported me, whether working abroad, in Berkeley or in Paris, or working in Karlsruhe.
- Ulrich Husemann for being the second reviewer of this thesis and the enthusiasm he showed for the topic.
- Kai Dolde for his support as a friend, and the great time we had together while working on sterile neutrinos.
- Anton Huber as my supervisor during my students assistance at KATRIN, who was always friendly and forthcoming.
- David Radford, together with the whole TRISTAN-group, for the many fruitful meetings and input during the master's thesis.
- Stefan Groh, Marco Kleesiek, Ferenc Glück and Joachim Wolf, for their support and help concerning software, as well as experimental difficulties.
- Jonathan Gaffiot, Guillaume Mention, Matthieu Vivier, Mathieu Durero and Thibaut Houdy for their warmth during my visit at CEA-Saclay.
- Daniel Maier, Olivier Limousin and Olivier Gevin for their enthusiasm and big support in specifying and measuring the produced detector chips.

Without all of you this thesis would not have been possible!

Abstract

Sterile neutrinos, introduced as right-handed singlets to the Standard Model of particle physics, could explain the smallness of the neutrino mass. Sterile neutrinos would oscillate with the known neutrino flavors and thus produce additional mass eigenstates. The mass range of these, mostly sterile, new states are a-priori unknown. Sterile neutrinos in the eV-mass range for example could resolve some tensions in short baseline experiments, whereas sterile neutrinos in the keV-mass range are viable candidates for Dark Matter, and are well motivated from particle physics, e.g. in the Neutrino Minimal Standard Model.
The KATRIN (KArlsruhe TRItium Neutrino) experiment measures the energy spectrum close to its endpoint, in order to determine the neutrino mass with a sensitivity of $m_\nu = 200\,\mathrm{meV}$ (90% CL). KATRIN also allows to perform both, a search for eV-scale and keV-scale sterile neutrinos. While eV-scale sterile neutrinos are accessible with the nominal mode of operation, the search for keV-scale sterile neutrinos requires changes to the experimental setup and measurement strategy. In particular, the Main Spectrometer must be operated at low retarding potentials, in order to measure the entire β-decay spectrum, and a new detector system is needed, to accommodate for large electron rates and to allow a differential, high-resolution scan of the β-decay energy spectrum. This new mode of operation is investigated in the framework of the TRISTAN project (TRitium Investigation on STerile to Active Neutrino mixing).
The SOX (Short distance neutrino Oscillations with BoreXino) experiment is designed to specifically investigate short-baseline neutrino oscillations and thus directly allows the search for eV-scale sterile neutrinos.
The first part of this thesis thematises eV-scale sterile neutrino searches with the KATRIN and the SOX experiment. For the first time, a combined sensitivity study of KATRIN and SOX prospective data is presented in this work. It is shown, that using the complementary measurements of KATRIN and SOX, preferred parameter space to explain anomalies in short-baseline experiments is fully explored by combining the two experiments. Moreover, in a novel approach, the impact of eV-scale sterile neutrinos on the mass determination of KATRIN is analyzed. Here, the prospective results of SOX are used to constrain the allowed parameters for a sterile neutrino in the KATRIN data analysis. This way, the KATRIN neutrino mass sensitivity becomes largely independent on the possible existence of a light sterile neutrinos.
The second part of this thesis is dedicated to the keV-scale sterile neutrino search with KATRIN. At first, general design studies on the layout of the new TRISTAN detector are presented. To reduce detector related systematic effects such as charge sharing, pile up and backscattering, we deduce that the future TRISTAN detector should have at least 10^4 pixels, and a detector radius of about 200 mm.
Based on extensive studies of detector backscattering with the software package KASSIOPEIA and KESS, a new Monte Carlo simulation program has been developed, which

allows for a fast calculation of the β-decay energy spectrum. Within this framework, the impact of detector backscattering, energy threshold, and the detector dead layer have been studied. It is shown that backscattering and energy loss in the dead layer lead to a significant shift of the energy spectrum to lower energies and thereby smear out the tiny signature of a possible keV-scale sterile neutrino. Consequently detectors with extremely thin dead-layers, fast and efficient magnetic back-reflection of backscattered electrons, a backscattering veto-system, and finally an extremely precise modeling of these effects will be required for a high-sensitivity keV-scale sterile neutrino search with KATRIN. First design considerations of a veto system and optimized magnetic back-reflection are presented in this thesis.
Based on the above-mentioned design properties for a novel detector system for KATRIN, a prototype detector has been developed by the Halbleiter Labor of the Max-Planck-Society in Munich (HLL). In this thesis the very first characterization of this detector, equipped with read-out electronics from CEA, is presented. First measurements with x-ray calibration sources demonstrate the functionality of the detector and read-out system and reveal a good energy resolution (FWHM < 500 eV at 6 keV) as well as an energy response linearity of a few per mille.

Zusammenfassung

Sterile Neutrinos sind rechtshändige Singulett Zustände im Standard Modell der Teilchen Physik und können auf natürliche Weise die Neutrinomasse erklären. Ein steriles Neutrino würde sich mit den bekannten Neutrino Generationen mischen und dadurch einen zusätzlichen Masseneigenzustand erzeugen. Die genaue Größe der sterilen Neutrinomasse ist allerdings nicht bekannt. Ein steriles Neutrino im Massenbereich von wenigen eV könnte zum Beispiel Anomalien bei sogenannten short-baseline Experimenten beheben, sterile Neutrinos im Bereich von keV hingegen sind ein Kandidat für Dunkle Materie und werden zudem in Theorien wie dem "Neutrino Minimal Standard Model"(νMSM) vorgeschlagen.
Das KATRIN (KArlsruhe TRItium Neutrino) Experiment misst das Tritiumzerfallsspektrum in der Nähe des Endpunkts um somit die Neutrinomasse mit höchster Präzision zu vermessen, $m_\nu > 200\,\mathrm{meV}$ (90% CL). Zusätzlich bietet KATRIN die Möglichkeit nach sterilen Neutrinos im eV- als auch keV-Massenbereich zu suchen. Während die Suche nach eV-schweren sterilen Neutrinos mit der nominellen Messstrategie von KATRIN möglich ist, benötigt die Such nach keV-schweren Neutrinos Änderungen am experimentellen Aufbau. Insbesondere muss das Hauptspektrometer bei niedrigem Gegenspannungen betrieben werden, um das gesamte β-Zerfallsspektrum zu messen. Dies erfordert zusätzlich ein neuartiges Detektorsystem, um die erhöhte Zählrate zu detektieren und das Energiespektrum mit hoher Energieauflösung zu vermessen. Dieser neuartige Betriebsmodus wird im Rahmen des TRISTAN Projekts (TRitium Investigation on STerile to Active Neutrino mixing) untersucht.
Das SOX (Short distance neutrino Oscillations with BoreXino) Experiment hat das Ziel „short-baseline“ Neutrinooszillationen zu untersuchen und ermöglicht hierdurch das direkte Erforschen von eV-schweren sterilen Neutrinos.
Der erste Teil dieser Arbeit thematisiert die Suche nach eV-schweren sterilen Neutrinos mit KATRIN und SOX. Erstmalig wurde dazu, im Rahmen dieser Arbeit, eine kombinierte Sensitivitätsanalyse beider Experimente durchgeführt. Dabei konnte gezeigt werden, dass die kombinierte Analyse, aufgrund der Komplementarität der beiden Experimente, den gesamten bevorzugten Parameterbereich (95% CL) aus der „Reactor Antineutrino Anomaly“ mit 90% CL abdecken wird. Außerdem wurde in einem neuartigen Ansatz der Einfluss von eV-schweren sterilen Neutrinos auf die Neutrinomassenbestimmung von KATRIN analysiert. Die Idee ist, bei der Massenanalyse von KATRIN, die Parameter für sterile Neutrinos basierend auf Ergebnissen von SOX einzuschränken. Die Massenbestimmung von KATRIN ist hierdurch weitgehend unabhängig von der Existenz eines eV-schweren sterilen Neutrinos.
Der zweite Teil der Arbeit ist der Suche nach keV-schweren sterilen Neutrinos mit KATRIN gewidmet. Zunächst wurde das generelle Layout eines zukünftigen TRISTAN-Detektors untersucht. Um detektorspezifische systematische Effekte wie „charge sharing“, „pile up“ und Rückstreuung zu reduzieren, sollte der Detektor mindestens 10^4 Pixel und einen

Radius von 200 mm haben.
Anhand von Rückstreuungsstudien mit den Programmen KASSIOPEIA und KESS wurde ein neuartiges Monte Carlo Simulationsprogramm entwickelt, welches eine schnelle Berechnung des β-Zerfallsspektrums ermöglicht. Damit konnte der Einfluss von Rückstreuung, Energieschwelle und Detektortotschicht auf das Zerfallsspektrum untersucht werden. Dabei wird gezeigt, dass diese Effekte zu signifikanten Modifikationen des Zerfallsspektrums führen und dadurch die Detektion der Signatur eines keV-schweren sterilen Neutrinos erschweren. Folglich wird ein Detektor mit geringer Totschicht, mit schneller und effizienter magnetischer Reflektion von zurückgestreuten Elektronen, mit einem Veto-System für rückgestreute Elektronen und eine genaue Modellierung dieser Effekte für die Suche nach keV-schweren sterilen Neutrinos benötigt. Erste Studien zum Design eines Vetosystems und zur Optimierung der magnetischen Rückstreuung wurden in dieser Arbeit durchgeführt.
Anhand der genannten Designeigenschaften für das neuartige KATRIN-Detektorsystem wurde am Halbleiterlabor der Max-Planck-Gesellschaft in München (HLL) ein Detektorprototyp entwickelt. In dieser Arbeit werden die Messungen zur Charakterisierung des Prototyps, welcher mit einem Auslesesystem vom CEA ausgestattet wurde, vorgestellt. Erste Messungen mit radioaktiven Proben zeigten die Funktionsfähigkeit des Detektors und ergaben eine gute Energieauflösung (FWHM $<$ 500 eV at 6 keV) und Linearität auf dem pro Mille Niveau.

Contents

1. Neutrino physics

This chapter gives an overview of the field of neutrino physics. In the first section, a historical review from the discovery of neutrinos up to the cutting-edge research topics is given. The second and third section both focus on so-called sterile neutrinos. The existence of eV-scale sterile neutrinos could explain anomalies in several short baseline experiments, whereas keV-scale sterile neutrino are a viable candidate for Dark Matter.

1.1. History of neutrinos

Discovery of Neutrinos

The idea of neutrinos was first postulated in the year 1930 by W. Pauli [Pau30]. In a letter to the Technical University of Zurich, he suggested a new particle, which he called neutron, explaining the continuous electron energy spectrum of β-decays [Cha14]. This particle was hypothesized to reside inside the nucleus, to be deprived of electric charge and to have a spin of 1/2. Two years later, J. Chadwick discovered the "real" neutron, a neutral particle with a mass similar to the proton, residing in the atomic nucleus [Cha32]. Only thereafter, E. Fermi formulated the first quantum theory of β-decays [Fer34]. Therein, a massive neutral particle, called neutron n, decays into the positive charged proton p, the negative charged electron and into the neutral, massless particle, called neutrino ν, or more specifically an electron antineutrino $\bar{\nu}_\mathrm{e}$.

$$n \longrightarrow p^+ + e^- + \bar{\nu}_\mathrm{e} \tag{1.1}$$

In 1956, C. Cowan [Cow56] could prove the existence of the inverse β-decay

$$p^+ + \bar{\nu}_\mathrm{e} \longrightarrow n + e^+, \tag{1.2}$$

where a proton and an electron antineutrino decay into a positron and a neutron. With the discovery of muon flavored neutrinos in 1962 [Dan62], by J. Steinberger, M. Schwartz and L. Lederman, it became clear that neutrinos appear in different flavors similarly to the flavor generations in the charged lepton sector. For their discovery, they were the first neutrino physicists to be honored with the Nobel prize in physics in 1988 [Nob16]. The last neutrino flavor, namely the tau neutrino, was longely hypothesized before being discovered about 20 years later by the DONUT experiment [Kod01].

Neutrino oscillation

B. Pontecorvo was the first to predict neutrino oscillations [Pon57], while the first experimental evidence was measured about ten years later by experiments such as Homestake, SNO and Kamiokande. One of the first experiments to observe neutrino oscillations was the Homestake Experiment lead by R. Davis [Dav68]. He measured the solar electron neutrino flux and detected a significant deficit of high energy solar neutrinos, compared to the expectation from the solar neutrino model. This deficit, also referred to as solar neutrino problem, was later theoretically explained by Mikheyev, Smirnov and Wolfenstein [Wol78; Mik86]. Their model, the so called MSW-effect, describes the modification of neutrino flavors inside the sun, due to matter effects.
With experimental observations, from solar neutrino experiments [Ahm01] (e.g. SNO), atmospheric neutrino experiments [Fuk98] (e.g. Super-Kamiokande), reactor neutrino experiments [An12] (e.g. Daya-Bay) and beam neutrino experiments [Abe14] (e.g. T2K), the physics of neutrino oscillations was thoroughly investigated.
Mathematically, neutrino oscillation is expressed by

$$\nu_l = \sum_{i=1}^{3} U_{li} \cdot \nu_i \quad \text{or} \quad \begin{pmatrix} \nu_e \\ \nu_\mu \\ \nu_\tau \end{pmatrix} = \begin{pmatrix} U_{e1} & U_{e2} & U_{e3} \\ U_{\mu 1} & U_{\mu 2} & U_{\mu 3} \\ U_{\tau 1} & U_{\tau 2} & U_{\tau 3} \end{pmatrix} \begin{pmatrix} \nu_1 \\ \nu_2 \\ \nu_3 \end{pmatrix}, \tag{1.3}$$

where ν_l ($l = e, \mu, \tau$) denotes the three known neutrino flavor eigentstates, namely electron, muon and tau, ν_i ($l = 1, 2, 3$) denotes the so-called neutrino mass eigenstates and U is the Pontecorvo–Maki–Nakagawa–Sakata matrix [Mak62]. In a simplified oscillation model with only two flavors and mass eigenstates, the probability for a neutrino of flavor ν_x to oscillate into another flavor eigenstate ν_y is

$$P(\nu_\mathrm{x} \to \nu_\mathrm{y}) = \sin^2(2\theta)\sin^2\left(1.27 \cdot \Delta m^2_\mathrm{xy}/\mathrm{eV}^2 \frac{L/\mathrm{km}}{E_\nu/\mathrm{GeV}}\right) \qquad \Delta m^2_\mathrm{xy} = m^2_\mathrm{x} - m^2_\mathrm{y}, \tag{1.4}$$

E_ν denotes the neutrino energy, Δm^2_xy is the difference of the squared masses, corresponding to the appropriate mass eigenstates, L is the distance the electron traveled and θ denotes the mixing angle between the flavor eigenstates.
From neutrino oscillation one can deduce the matrix elements U_{ei}, i.e. the mixing between the neutrino eigenstates, and the relative neutrino masses, i.e. the squared mass differences Δm^2. Moreover, the existence of neutrino oscillation implies a non-zero neutrino mass (eq. 1.4).

Neutrino mass

Current experimental work on the absolute neutrino mass scale is divided into: electron kinematics in β-decay, half-life measurements in neutrinoless double β-decay ($0\nu\beta\beta$) and cosmological observations. While analyzing the β-decay would directly yield the neutrino mass as an observable, other approaches, such as cosmological observations, indirectly measure the sum of all neutrino mass eigenstates. These results depend on the underlying

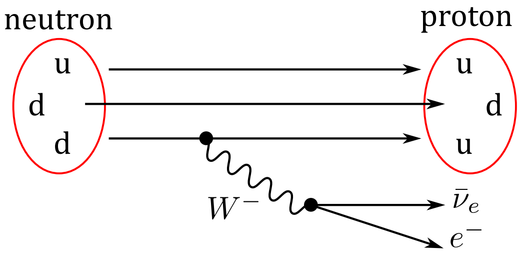

Figure 1.1: Feynman diagram of the β-decay. During the decay of the neutron, an electron and electron antineutrino are emitted. The maximal kinetic energy of the electron is reduced, affecting mainly the energy spectrum near the endpoint.

cosmological model.

- β-DECAY
  The current best limit in β-decay is given by the Troitsk and Mainz experiment [Ase11; Kra05] (eq. 1.5). In β-decay (see figure 1.1), a neutron decays into a proton, thereby emitting a W^--boson, which decays into an electron and an electron antineutrino. Measuring the electron energy spectrum, will hence yield the total decay energy minus the energy of the electron antineutrino. The kinetic energy spectrum of the electron is thus shifted by the effective mass of the electron antineutrino

$$m_{\bar{\nu}_e} = \sqrt{\sum_{i=1}^{3} |U_{ei}| m_{\nu i}^2} \leq 2.05\text{eV } (95\%\text{CL}). \tag{1.5}$$

- NEUTRINOLESS DOUBLE β-DECAY
  A different approach for determining the electron neutrino mass, is the neutrinoless double β-decay. The continuous electron spectrum of double β-decay, i.e. two neutrons decay into two protons, two electrons and two electron antineutrinos, is shifted by two times the electron antineutrino mass.
  If the neutrino is its own anti-particle, i.e. the neutrino is a Majorana particle, then the electron antineutrino might be directly absorbed in the second β-decay within the nucleus (see figure 1.2). The hereby emitted electrons would yield a mono-energetic line at the spectrum endpoint. Since the $0\nu\beta\beta$-decay rate is proportional to the effective Majorana mass $m_{\beta\beta}$, current experiments, such as GERDA [Ago13], KamLAND-Zen [Gan13; Kam16], CUORE [Gor12] and MAJORANA [Xu15], have set a limit on the effective Majorana mass:

$$m_{\beta\beta} = \left| \sum_{i=1}^{3} U_{ei}^2 m_i \right| = \sum_{i=1}^{3} \left| |U_{ei}|^2 \cdot e^{i\delta_{\mathrm{M}i}} \right| m_i \leq 0.12\text{–}0.25\,\text{eV}(90\%\text{CL}). \tag{1.6}$$

  The wide range of possible upper limits mainly arises from uncertainties in the nuclear matrix elements.

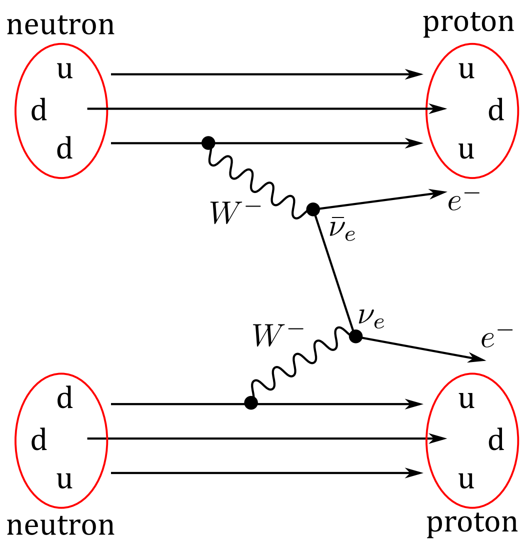

Figure 1.2: Feynman diagram of the neutrinoless double β-decay. The emitted electron antineutrino is directly absorbed as an electron neutrino, which is only possible if neutrinos are Majorana particles.

- Cosmology
  Two examples for cosmological observations are the WMAP [Goo06] and the Planck stallite missions [Ade14], giving an upper limit to the sum of neutrino masses

$$\sum_{i=1}^{3} m_i \leq 0.23\,\text{eV (95\%CL)}, \tag{1.7}$$

  The limit originates from the current cosmological model, the ΛCDM, and combines multiple cosmological observations. Here Planck data, data from WMAP polarization, cosmic microwave background data, and data from baryonic acoustic oscillations were combined [Ade14].

Physics beyond the Standard Model

A natural extension of the Standard Model of Particle Physics (SM) is the introduction of right-handed neutrinos, so-called sterile neutrinos, that are only sensitive to the gravitational interaction. Sterile neutrinos would mix with the known neutrino flavors and thereby form a forth mass eigenstate ν_4, with the eigenvalue m_4:

- $m_4 = \mathcal{O}(\text{eV})$ (see also section 1.2):
  Sterile neutrinos in the range of a few eV [Aba12], could explain anomalous experimental data, such as the Gallium Anomaly [Giu11], the Reactor Antineutrino Anomaly [Men11].

- $m_4 = \mathcal{O}(\text{keV})$ (see also section 1.3):
  keV-scale sterile neutrinos [Adh16] are viable candidates for so called Dark Matter, as they help to solve tensions at small cosmological scales. Moreover, keV-scale sterile neutrinos could be naturally included in some theoretical framework, such as the Neutrino Minimal Standard Model [Asa05a].

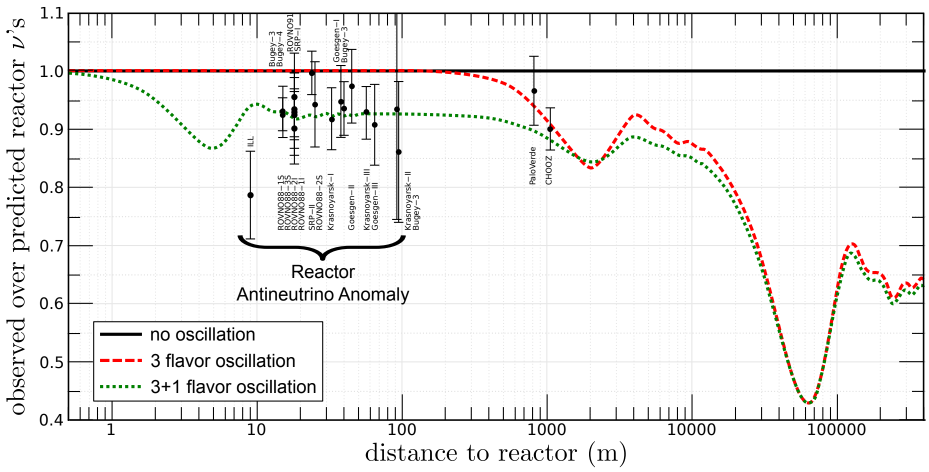

Figure 1.3.: Illustration of the measured reactor neutrino flux over the predicted value (without oscillation). The marker depict the reported fluxes from the reactor experiments ILL-Grenoble, Goesgen, Rovno, Krasnoyarsk, Savannah River and Bugey. The nominal oscillation with 3 flavour eigenstates is depicted with the dashed red line, while the dottet green line shows an adapted 3+1 oscillation picture, $|\Delta m^2_{14}| = 2.2\,\mathrm{eV}^2$ and $\sin^2(2\theta_{14}) = 0.12$. Adapted from [Men11].

- $m_4 = \mathcal{O}(\mathrm{GeV})$:
  Heavy sterile neutrinos, in the range of GeV or at larger mass scale, could explain the small neutrino masses $< eV$ via the see-saw mechanism. Moreover, within the neutrino Minimal Standard Model [Asa05b], GeV-scale sterile neutrinos could explain the matter-antimatter asymmetry in the universe.

This work focuses on sterile neutrinos in the eV- to keV-mass range.

1.2. eV-scale sterile neutrinos

So far, neutrino oscillation experiments with solar, atmospheric and reactor neutrinos could be interpreted in the three neutrino flavor picture.
However, in March 2011, a refined calculation of the predicted reactor neutrino flux, resulted in a small increase of the predicted flux by 3.5%. To good approximation this reevaluation applies to all reactor neutrino experiments. The synthesis of published experiments at reactor-detector distances $< 100\,\mathrm{m}$ thus leads to a ratio of observed event rate to predicted rate of 0.943 ± 0.023, that deviates from unity at 98.6% C.L. This observation is called the Reactor Antineutrino Anomaly (RAA) and illustrated in figure 1.3.

This anomaly could be explained by the existence of a fourth non-standard neutrino state, driving neutrino oscillations at short distances $< 100\,\mathrm{m}$. Within this thesis, this model is referred to as the 3+1 oscillation model, where the +1 depicts the additional sterile neutrino.
Combining the reported deficit from Gallium and SAGE [Giu11], and MiniBOONE [Agu09],

the no-oscillation hypothesis is disfavored at 95% CL (displayed in figure 1.4), for sterile neutrino parameters

$$\Delta m_{14}^2 > 1.5\,\text{eV} \qquad \text{and} \qquad \sin^2(2\theta_{14}) \in [0.06, 0.22]. \tag{1.8}$$

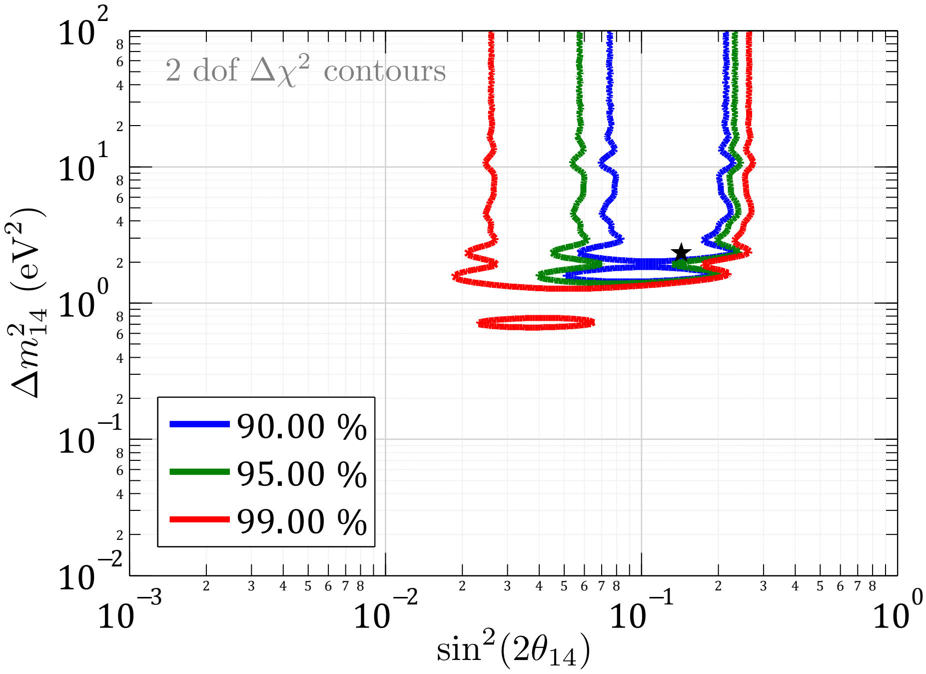

Figure 1.4.: Allowed regions in $\sin^2(2\theta_{\text{new}})$–$|m_{\text{new}}^2|$ plane for a sterile neutrino in a 3+1 oscillation hypothesis. The star represents the best-fit values. The no-oscillation hypothesis is disfavored at 95% CL, for sterile neutrino parameters $\Delta m_{14}^2 > 1.5\,\text{eV}$ and $\sin^2(2\theta_{14}) \in [0.06, 0.22]$. Adapted from [Men11].

1.3. keV-scale sterile neutrinos

Sterile neutrinos in the keV mass range are well motivated in particle physics, as well as in cosmology.

Particle physics

In the Standard Model of particle physics, the fermion sector consists of three generations of letpons and quarks, where all fermions, except the neutrinos, occur in left-handed and right-handed chirality, and are massive. The Neutrino Minimal Standard Model (νMSM)[Asa05a; Asa05b] includes the neutrino masses and adds a right-handed partner, called sterile neutrino, to the neutrino generations (see in figure 1.5).
These sterile neutrinos are singlets under the Standard Model gauge group and hence do not interact with strong or weak forces. This allows to introduce a new mass term, called Majorana mass, to the Lagrangian. Though there is no a-priory favored mass scale for the

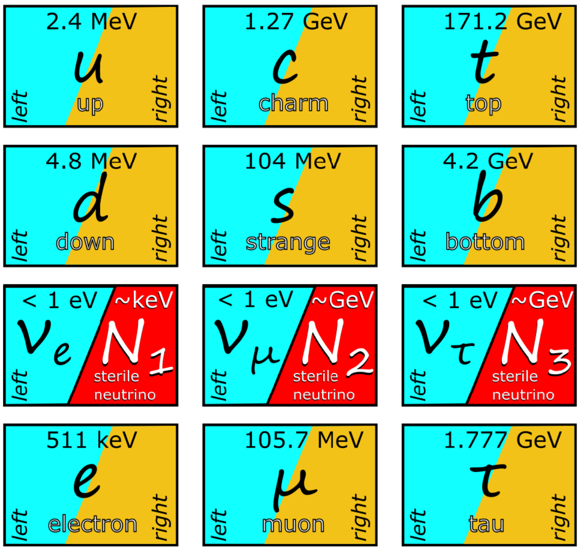

Figure 1.5: Depiction of the fermion sector in the Neutrino Minimal Standard Model (νMSM). To each left handed neutrino, a right handed partner in the keV, GeV and GeV range is added. The keV-scale sterile neutrino would represents the Warm Dark Matter particle. Illustration from [Dol16].

Majorana mass, in the νMSM two different mass scales are chosen in order to explain a maximal number of open questions from the SM:

- $M_1 = \mathcal{O}(\text{keV})$, as a candidate for Cold or Warm Dark Matter, depending on the cosmological production mechanism [Dod94].

- $M_2 = \mathcal{O}(\text{GeV})$ and $M_3 = \mathcal{O}(\text{GeV})$, explaining the smallness of the neutrino mass via the Seesaw mechanism and, if $M_2 \approx M_3 \in (15\,\text{MeV}, 100\,\text{GeV})$, they can account for the baryon asymmetry through oscillation-induced leptogenesis [Adh16; Asa05b].

Cosmology

keV-scale sterile neutrinos in the form of moderate Cold or Warm Dark Matter could solve the missing satellite problem and cusp-core problem in cosmology, and are thus viable candidates for Dark Matter.
The **missing satellite problem** [Kly99; Spr05; Lov12] expresses the tension between the number of observed to the number of predicted satellite galaxies by the cosmological Λ Cold Dark Matter model. Compared to Cold Dark Matter, a Warm Dark Matter particle would yield a larger free-streaming length. A Warm Dark Matter dominated universe would hence hinder structure formation on smaller scales and decrease the number of satellite galaxies.

The investigation of the density profile $\rho = r^{-\alpha}$ of Dark Matter galaxy halos reveal tensions between observation and prediction, which is known as the **cusp and core problem** [Dub91; Ohs11; Nav96; Nav97]. Cosmological Λ Cold Dark Matter simulation yield a cusp density profile $\alpha \approx 1$, i.e. the density profile has a steep increase at low radii, whereas observations yield a cored density profile $\alpha \approx 0.3$. In the case of Warm Dark Matter, halos could naturally produce a cored density profile [Adh16].

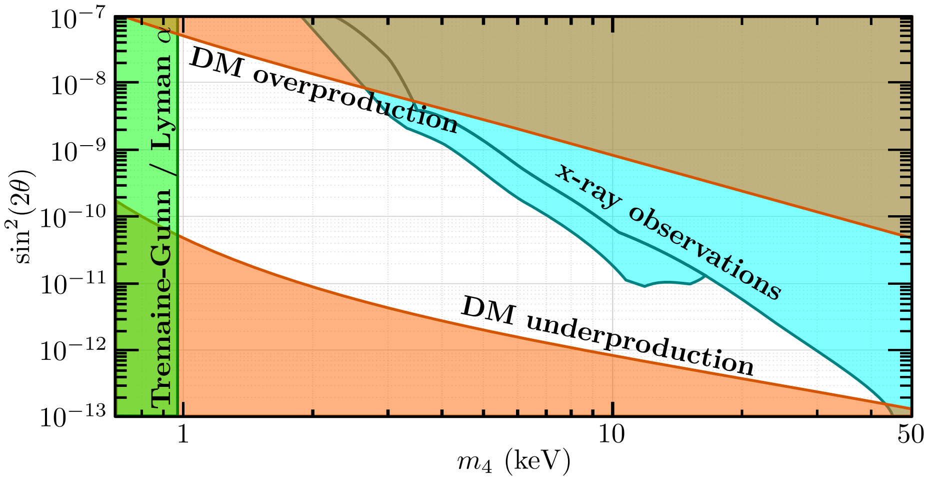

Figure 1.6.: Cosmological constraints on a Dark Matter scenario, solely consisting of keV-scale sterile neutrinos. The white area corresponds to the allowed parameter region for a Dark Matter sterile neutrino.

On the other hand **cosmological** models allow to **constrain** the parameter space of sterile neutrinos (see figure 1.7), by comparing cosmological observations to model simulations with a possible sterile neutrino. An example for such limit is the sterile neutrino production mechanism. In a sterile neutrino scenario with low mixing $\sin^2(2\theta) < 10^{-11}$ ($m_4 = 2$ keV), the number of produced sterile neutrino would be too small, thus the density of sterile neutrinos would be lower than the observed Dark Matter density. Vice versa, for high masses and large mixing angles $\sin^2(2\theta) > 10^{-9}$ ($m_4 = 10$ keV), the density of sterile neutrinos would exceed the observed Dark Matter density, see for example [Sch16] for discussion of resonant production mechanisms.
Other comsological constrains are for example, the non observation of mono-energetic x-ray lines [Boy06; Hor14], the Tremaine-Gunn bound [Tre79], the Lyman-α constraint [Vie13] and also constrains from super novae [Arg16].

2. Experiments

In this chapter two neutrino experiments, SOX and KATRIN, are presented. The SOX experiment focuses on neutrino oscillation with small values of L/E, in order to investigate eV-scale sterile neutrinos, whereas the KATRIN experiment examines the β-decay of tritium, in order to measure the mass of electron antineutrinos.
The first section of this chapter is dedicated to give a short overview of the SOX experiment. The physics background of the experiment as well as the expected sensitivity to eV-scale sterile neutrinos is presented.
In the second section the KATRIN experiment is discussed in detail. This section is further subdivided into the standard operation mode of KATRIN, i.e. using KATRIN as suggested in the design report [Ang05], and a possible new mode of operation to search for both eV- and keV-scale sterile neutrinos.

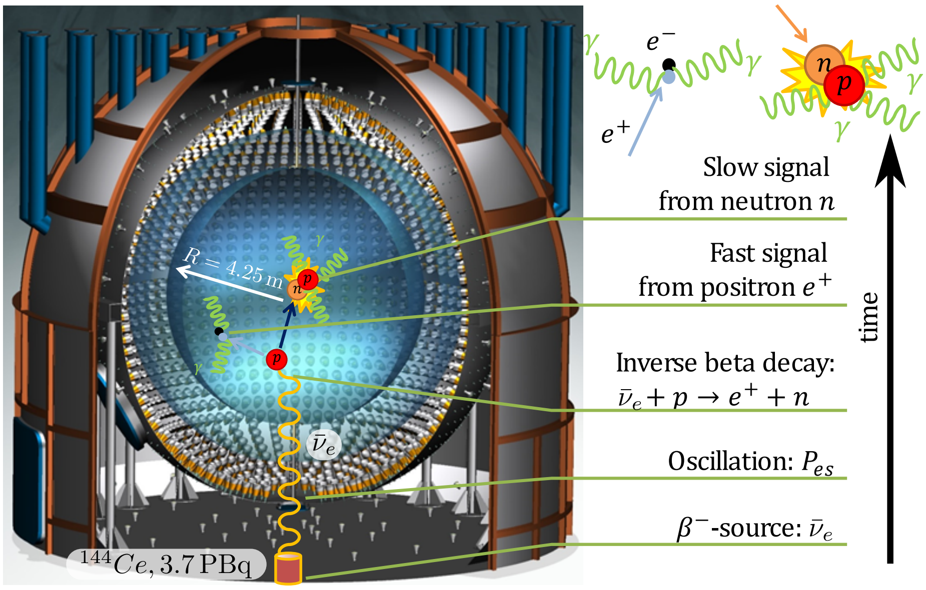

Figure 2.1.: Illustration of the experimental setup of Borexino, including the 3.7 PBq strong ^{144}Ce source, which is positioned in a maintenance chamber directly below the Borexino detector.

2.1. SOX

The Short distance neutrino Oscillations with BoreXino experiment, or in short the SOX experiment, probes neutrino oscillation at small values of $L/E \approx (4.5 \pm 4)\,\mathrm{m/MeV}$ [Cri11],

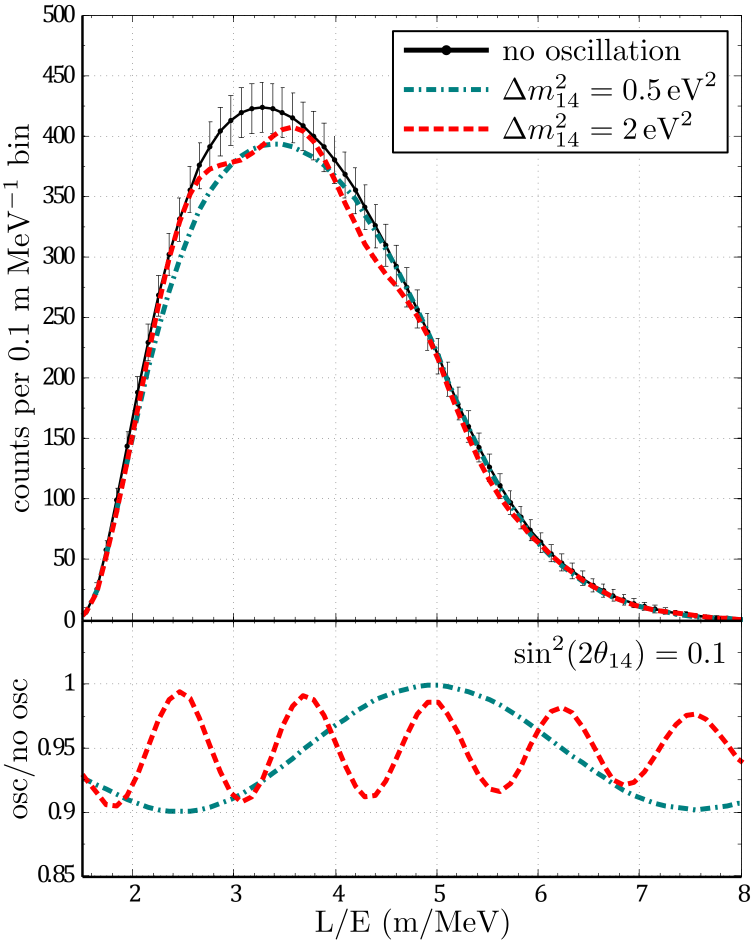

Figure 2.2: (top) Expected electron antineutrino rate vs L/E for the SOX-experiment, with two hypothetical eV-scale sterile neutrino cases $\Delta m^2 = 0.5\,\mathrm{eV}^2$ (green) and $\Delta m^2 = 2\,\mathrm{eV}^2$ (red), both for a mixing of $\sin^2(2\theta_{14}) = 0.1$. (bottom) Dividing the sterile neutrino cases with the 'no oscillation' case, yields the sinusoidal term from equation 1.4. Adapted from [Gaf15]

thus directly testing current experimental tensions, such as the Reactor Antineutrino Anomaly. If SOX measures a disappearance of electron flavored (anti-)neutrinos, i.e. a deficit of the measured neutrino flux (see figure 1.3), then this would strongly indicate the existence of a forth neutrino flavor, a sterile neutrino in the mass range of $\mathcal{O}(\mathrm{eV})$.
The SOX experiment is designed to utilize the Borexino detector to measure the number of electron antineutrinos, emitted by a radio active ^{144}Ce-source, which is placed in the maintenance chamber below the detector. The setup is depicted in figure 2.1. The ^{144}Ce source is a β^- emitter, thus isotropically producing electron antineutrinos. Electron antineutrinos, which undergo an inverse β-decay within the detector, produce a positron and a neutron. The positron quickly annihilates with an electron in the protons in the detector, causing a scintillation signal, whereas the neutron is only absorbed after several elastic scatterings and produces a slow scintillation signal.

The Borexino detector allows to measure the position L and energy E of the electron antineutrinos interacting within the detector medium. If now, on the way between source and detector, the emitted electron antineutrino oscillates into a sterile neutrino flavor, it will not be detected, as it does not interact with baryonic matter. Consequently, the measured electron antineutrino flux would be reduced, compared to the predicted value, where the electron antineutrino does not oscillate into a sterile state.
The expected electron antineutrino rate in the detector medium is depicted in figure 2.2

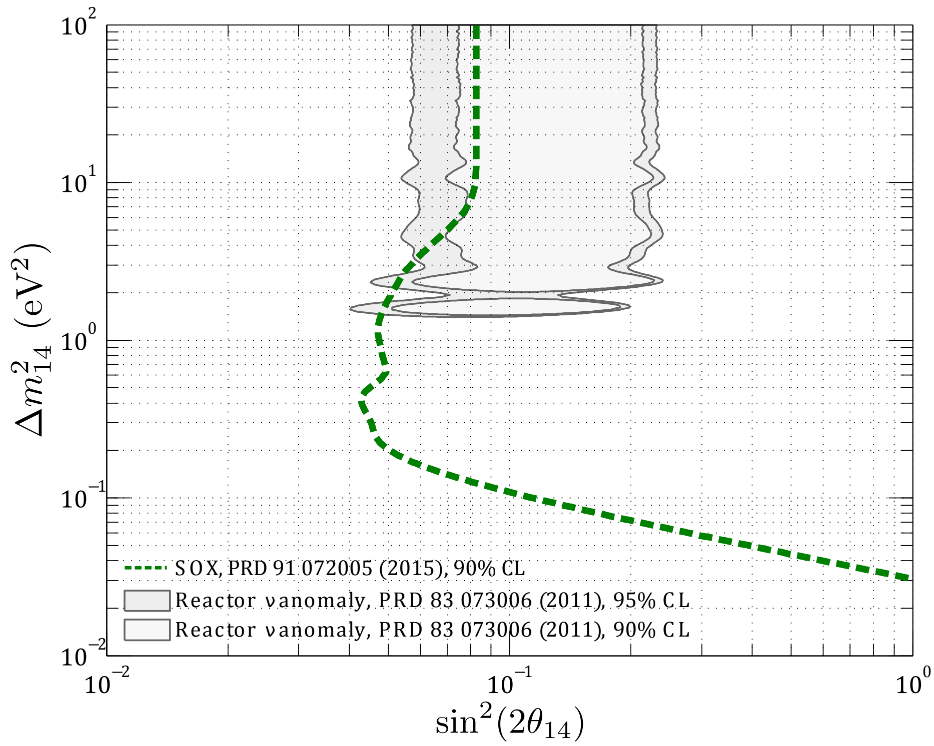

Figure 2.3.: Expected sensitivity of the SOX experiment for measuring 1.5 years, in the plane of the sterile neutrino parameters Δm^2, $\sin^2(2\theta_{14})$. Low masses $\Delta m^2 < 0.2\,\mathrm{eV}^2$ shift the oscillation signal to higher L/E, thus reducing the sensitivity. Adapted from [Gaf15].

(top). Dividing the expected rate for the case of an existing eV-scale sterile neutrino by the typical three flavor prediction, yields the sinusoidal behavior of the detected electron antineutrino rate predicted in equation 1.4 (figure 2.2 (bottom)). A low mass of the sterile neutrino $\Delta m^2 = 0.5\,\mathrm{eV}^2$, yields a low oscillating signal for $L/E \in [0.5\,\mathrm{m/MeV}, 8.5\,\mathrm{m/MeV})$, whereas a high mass $\Delta m^2 = 2\,\mathrm{eV}^2$ yields a quick oscillating signal.

The sensitivity to a sterile neutrino, illustrated in the Δm^2-$\sin^2(2\theta_{14})$ plane (see figure 2.3), would thus yield low sensitivities in the low mass range $\Delta m^2 < 0.1\,\mathrm{eV}^2$, as the oscillation is not visible within $L/E \in [0.5\,\mathrm{m/MeV}, 8.5\,\mathrm{m/MeV})$, and high sensitivities in the high mass range $\Delta m^2 > 0.1\,\mathrm{eV}^2$. However, too high masses $\Delta m^2 > 10\,\mathrm{eV}^2$ lead to an averaging effected of the sinusoidal term in equation 1.4.
The SOX experiment has the possibility to probe a big part of the 95% CL parameter space from the Reactor Antineutrino Anomaly.

2.2. KATRIN

The KArlsruhe TRItium experiment, short KATRIN, aims to determine the mass of the electron antineutrino by measuring the kinetic energy of electrons, that are emitted from a

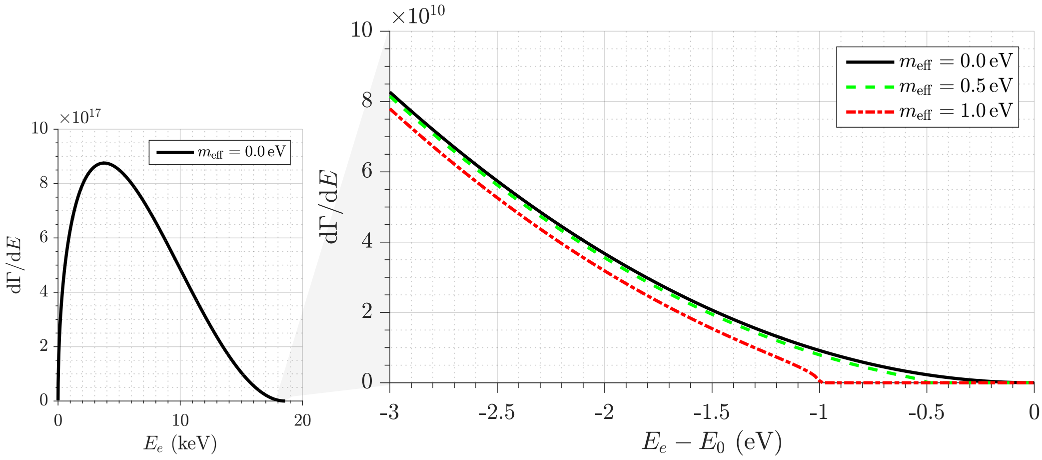

Figure 2.4.: Electron energy spectrum of the tritium β-decay (left) and a magnified illustration near the electron energy endpoint $E_0 = 18.575\,\text{eV}$. For increasing effective neutrino masses, the energy spectrum is shifted to lower energies. Only $2 \cdot 10^{-11}\%$ of the electron decays are expected with energies in the last electron volt region near the endpoint.

high luminous tritium source. In particular, the KATRIN experiment focuses on the energy region near the energy spectrum endpoint, $E - E_0 \in [-30\,\text{eV}, 5\,\text{eV}$, where E_0 denotes the energy endpoint, since in this region the signature of a massive electron antineutrino is the most distinct. A non-zero mass of the electron antineutrino leads to a shift of the electron energy spectrum by the corresponding mass value, illustrated in figure 2.4.

With the Main Spectrometer, used as an energy filter, the tritium β-decay spectrum is analyzed in an integral way. After an effective data taking time of three years — the total experimental time would be roughly five years, including maintenance operations — the KATRIN experiment predicts to measure the mass of the electron antineutrino with a sensitivity of

$$m_{\bar{\nu}_e} = \sqrt{\sum_{i=1}^{3} |U_{ei}| m_{\nu i}^2} \leq 0.2\,\text{eV}\ (90\%\text{CL}), \tag{2.1}$$

thus improving the former sensitivity of direct measurements (eq. 1.5) by about a factor of 10 [Ang05].

In the following the experimental setup of the KATRIN experiment is presented in detail. The sections thereafter are dedicated to the sterile neutrino search in the eV- and keV-mass range. Questions such as, "What is the signature of a sterile neutrino?", "What is the sensitivity to the sterile neutrino?" and "How does a sterile neutrino search affect the experimental setup of KATRIN?", are addressed in these sections.

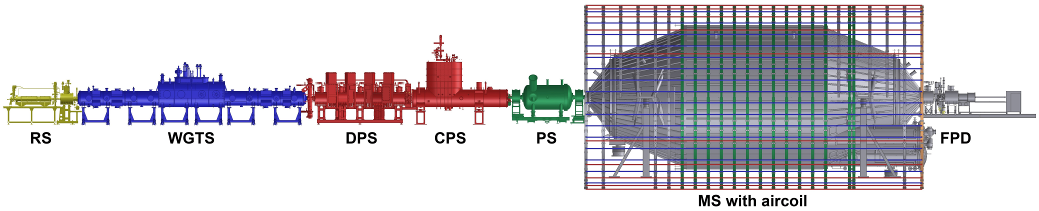

Figure 2.5.: Side view of the, in total about 70 m long, KATRIN experiment. From left to right, the experiment consists of the Rear Section (RS), the Source Section (WGTS), the Transport Section (DPS+CPS), the Spectrometer Section (PS+MS) and the Detector Section (FPD).

2.2.1. Standard operation

KATRIN in standard operation, refers to the investigation of the effective mass of the electron antineutrino and the appropriate experimental setup, illustrated in figure 2.5, presented in the KATRIN design report [Ang05].

Electrons, isotropically emitted from decaying tritium atoms in the Source Section, are adiabatically guided by magnetic fields along the whole experimental setup.

Rear Section

The task of the Rear Section [Bab14] is to monitor the electron plasma in the Source Section [Roe11; Roe13] and to define the electric potential at the rear end of the experimental setup [Bab12]. Moreover, with the help of an calibrational source mounted at the Rear Section, such as an electron gun [Val11], the column density of the tritium source is measured and the energy loss function, due to inelastic scattering of electrons in the Source Section, is determined.

Source Section

The Source Section, also referred to as Windowless Gaseous Tritium Source (WGTS), accommodates the Loop System [Bor06; Stu10; Pri15], the LARA system [Fis14; Sch13] and a dedicated cooling system [Gro11].

- The molecular tritium is injected directly in the center of the WGTS and simultaneously pumped out at both ends via Turbo Molecular Pumps. The injection and pump cycle is called the Inner **Loop System**. The Loop System is required to provide a constant column density of tritium molecules in in the WGTS, and thus a constant decay rate of about 10^{11} decays per second.

- The LAser RAman spectroscopy system, short **LARA system**, monitors the isotopic gas composition in the Source Section. Typically a tritium purity $> 95\%$ is expected.

- The installed **cooling system** reduces the operating temperature to (30 ± 0.03) K, in order to reduce thermal Doppler broadening of the emitted electrons.

Transport Section

The Transport Section, or Pumping Section, is subdivided into the Differential Pumping Section [Ubi09; Win11; Hac15] and the Cryogenic Pumping Section [Gil10; Jan15]. With the help of both stages, the tritium flow from Source to Spectrometer Section is reduced by 14 orders of magnitude.

- The **Differential Pumping Section** (DPS), is equipped with Turbo Molecular Pumps and reduces the tritium flow by five orders of magnitude. By biasing the WGTS and DPS with a known negative voltage, positive ions are prevented to enter the Main Spectrometer. Moreover, two dipole electrodes and two Fourier Transformation-Ion Cyclotron Resonators are installed, to remove and analyze positive ions.

- Tritium molecules are trapped by cryo-sorption at 6 K, on an argon layer in the **Cryogenic Pumping Section** (CPS). The CPS is designed with a small bent, thus increasing the probability of tritium molecules to hit the vessel walls. After an operation of about 60 days, the saturated argon frost layer is renewed, by heating the CPS to 100 K and pumping out of the released tritium molecules.

Spectrometer Section

In total, the KATRIN experiment has three spectrometers: the Monitor Spectrometer [Zbo13], used to monitor the high voltage system of the Main Spectrometer, the Pre Spectrometer [Fla03], employed as retention system for low energy electrons, and the Main Spectrometer (MS) [Ang05; Wan09], used as a high precision energy filter.
The Main Spectrometer is a so called MAC-E filter, which is short for Magnetic Adiabatic Collimation combined with an Electrostatic Filter. The working principle is illustrated in figure 2.6. The magnetic field gradient collimates the electron momenta in axial direction, whereas the electric field reflects electrons with kinetic energies lower than the applied electric field qU, with the charge q and the voltage U of the high voltage system. The energy resolution of the MAC-E filter is given by

$$\frac{\Delta E}{E_e} = \frac{B_{\mathrm{min}}}{B_{\mathrm{max}}} = \frac{3 \cdot 10^{-4}\,\mathrm{T}}{6\,\mathrm{T}}, \tag{2.2}$$

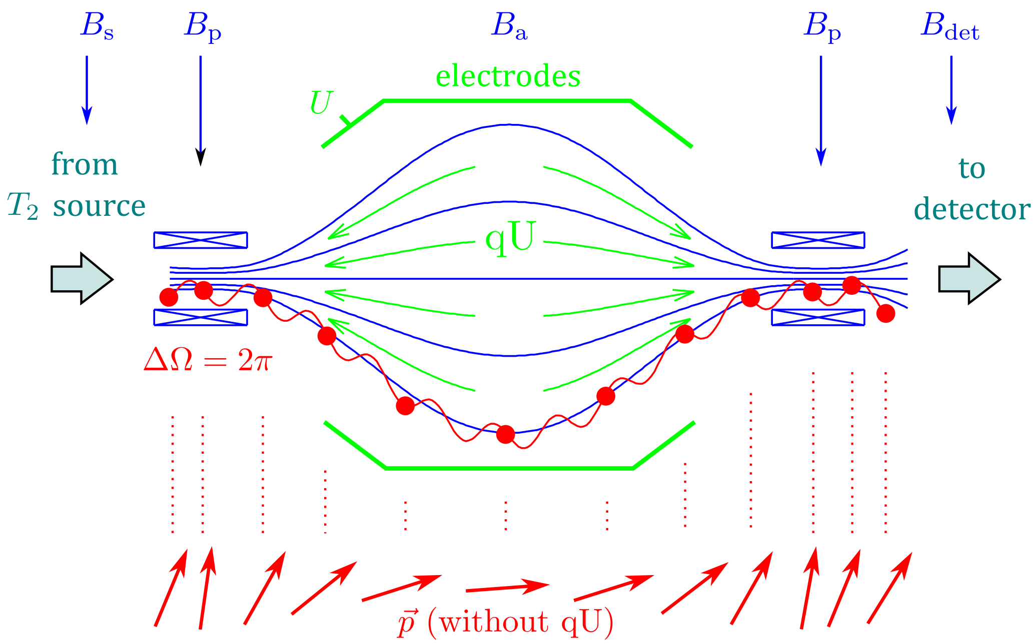

Figure 2.6.: Illustration of the working principle of the MAC-E filter at the KATRIN MS. Electrons are guided along the magnetic field lines, and due to the decreasing magnetic field — until the middle of the MS, referred to as analyzing plane — the electron momenta are collimated into axial direction. At the middle of the MS the electrostatic potential is at its maximum and only electrons with high enough axial momenta can overcome this electrostatic potential to reach the detector.

$B_{min} = B_a$ is the magnetic field in the analyzing plane and $B_{max} = B_p$ is the maximal magnetic field, given by the pinch magnets (see figure 2.6). For electron energies near the spectrum endpoint $E_e = 18.6\,\text{keV}$ the energy resolution is $\Delta E = 0.93\,\text{eV}$.
Moreover, the Spectrometer Section is equipped with an aircoil system [Glu13], installed around the Main Spectrometer, in order to diminish the impact of the terrestrial magnetic field, and an inner electrode system [Val10], within the Main Spectrometer, preventing electrons, emitted from the steel walls of the Main Spectrometer, to enter the sensitive volume in the Main Spectrometer.

Detector Section

The detector section is situated at the rear end of the experimental setup (see figure 2.7). It encompasses the silicon based pin-diode detector, also called Focal Plane Detector (FPD) [Sch14; Ams15] and a post-accleration electrode. Moreover, the Detector Section allows to insert calibration sources for the FPD.
The FPD has a radius of about 4.5 cm and is segmented into 148 pixels with a pixel area of $44\,\text{mm}^2$. Electrons passing the retarding potential U of the MS are later registered by the FPD. Scanning the electron energy spectrum with different retarding potentials, allows to count the number of electrons with energies higher then the retarding potential, and thus

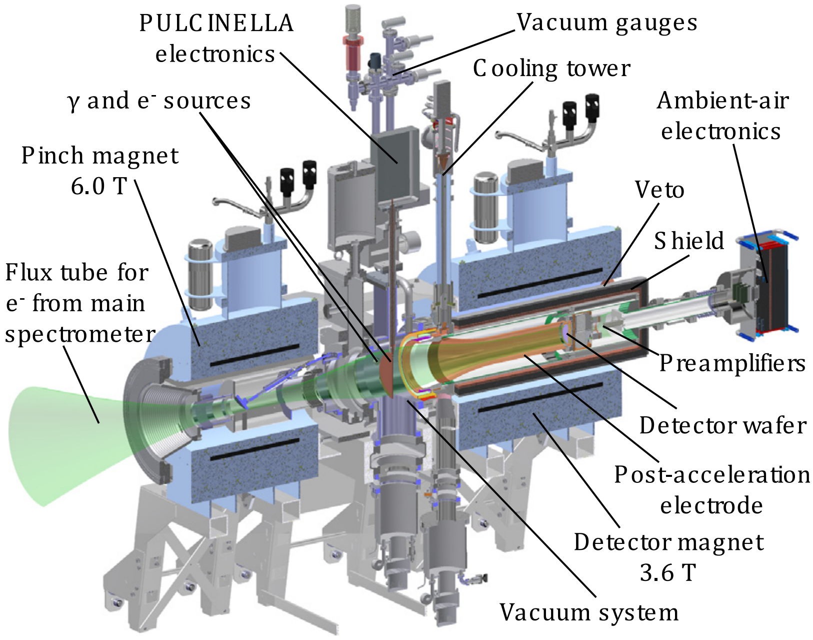

Figure 2.7: Schema of the Detector Section at KATRIN. The Main Spectrometer is situated directly to the left of the schema [Ams15].

allows to measure an integral β-decay energy spectrum.

2.2.2. Model of tritium β-decay spectrum

KATRIN integrally measures the number of electrons arriving at the detector for different values of the retarding potential U. The total number of electron counts is given by

$$N_{\text{tot}}(qU) = N_{\text{s}}(qU) + N_{\text{b}}(qU), \tag{2.3}$$

where N_{s} denotes the electron signal from tritium β-decay and N_{b} denotes the electron background. At the energy spectrum endpoint the electron background rate B is energy independent, thus the number of background related events scales with the time measured Δt_{qU} at a given retarding potential, $N_{\text{b}} = B \cdot \Delta t_{\text{qU}}$. The number of signal electrons at different retarding potentials U is given by

$$N_{\text{s}} \propto \Delta t_{\text{qU}} \int_{\text{qU}}^{E_0} \frac{\mathrm{d}N(E, m_\nu^2)}{\mathrm{d}E} \cdot R(E, qU) \cdot dE \qquad N_{\text{b}} = B \cdot \Delta t. \tag{2.4}$$

Here E_0 is the endpoint energy, $\mathrm{d}N(E, m_\nu^2)/\mathrm{d}E$ is the the differential β-decay energy spectrum and $R(E, qU)$ depicts the experimental response function.

- Response function $R(E, qU)$:
  The response function describes the detection probability of an emitted beta electron as a function of its surplus energy with respect to the retarding potential. It

encompasses all characteristics of the KATRIN experimental setup [Gro15]. The main components are the transmission function $T(E, qU)$ of the MAC-E Filter and inelastic scattering of the β electrons with molecular tritium in the source. The transmission function is given by:

$$T(E, qU) = \begin{cases} 0 & E - qU < 0 \\ \frac{1-\sqrt{1-\frac{E-qU}{E}\cdot\frac{B_\mathrm{s}}{B_\mathrm{a}}}}{1-\sqrt{1-\frac{B_\mathrm{s}}{B_\mathrm{max}}}} & 0 \leq E - qU < \Delta E \\ 1 & E - qU > \Delta E \end{cases} \tag{2.5}$$

Where B_s denotes the magnetic field in the source, B_a denotes the magnetic field in the analyzing plane of the Main Spectrometer and B_max is the maximal magnetic field, which is given by the pinch magnet $B_\mathrm{max} = B_\mathrm{p}$.
The inelastic scattering of β electrons in the source can be expressed with the energy loss function $f(\epsilon)$ per scattering and the probability P_i to undergo i times inelastic scatterings. ($P_0 \approx 0.413, P_1 \approx 0.293, P_2 \approx 0.167, P_3 \approx 0.0791$, etc.)

$$f(\epsilon) = \frac{1}{\sigma_\mathrm{inel}} \frac{\mathrm{d}\sigma}{\mathrm{d}\epsilon} \tag{2.6}$$

ϵ denotes the electron energy loss and σ_inel the inelastic cross section. Therefore the response function to first order is given by the convolutions of the transmission function with the energy loss function, while considering the probability P_i for the i-th time of elastic scattering and self convoluting the energy loss function i times:

$$R(E, qU) = T(E, qU) \otimes [P_0 + P_1 \cdot f(\epsilon) + P_2 \cdot f(\epsilon) \otimes f(\epsilon) + \ldots] \tag{2.7}$$

- β-decay energy spectrum $\mathrm{d}N/\mathrm{d}E$:
  The differential energy spectrum for electrons, considering a neutrino with mass m_ν, is given by:

$$\frac{\mathrm{d}N}{\mathrm{d}E} \propto F(Z, E) \cdot p_e \cdot (E + m_e c^2) \cdot (E_0 - E)\sqrt{(E_0 - E)^2 - m_\nu^2} \cdot \Theta(E_0 - E - m_\nu) \tag{2.8}$$

  With the Fermi function $F(Z, E)$, the electron momentum p_e, the electron mass m_e and the step function $\Theta(E_0 - E - m_\nu)$. The proportionality factor is derived by normalizing the total energy spectrum to the number of decays expected for the given column density of the tritium source ρd and the tritium decay half time τ.

In the case of neutrino mixing, the neutrino mass eigenstates m_i and the neutrino mixing parameters U_{ei} have to be considered. Therefore equation 2.8 has to be modified:

$$\frac{\mathrm{d}N}{\mathrm{d}E} \propto \sum_{i=1}^{N_\nu} |U_{ei}|^2 \sqrt{(E_0 - E)^2 - m_i^2} \cdot \Theta(E_0 - E - m_i) \tag{2.9}$$

The terms, which do not depend on the neutrino mass, were moved into the normalization factor. N_ν depicts the number of neutrino flavors.
For the case of $N_\nu = 3$, i.e. the standard model, the different mass eigenstates splittings are known to be in the sub-eV regime. With an energy resolution $\Delta E < 1$ eV the KATRIN experiment cannot resolve the tiny mass differences, known from neutrino oscillation experiments. Hence the observed spectrum appears as if there would be only a single mass eigenstate, called the effective neutrino mass m_{eff}.

$$m_{\mathrm{eff}} = \sum_{i=1}^{3} |U_{ei}|^2 \cdot m_i^2 \tag{2.10}$$

$$\tag{2.11}$$

In the case of $N_\nu = 4$, we add a fourth mass eigenstate to the β-decay spectrum, the additional mass eigenstate would hence correspond to a mostly sterile neutrino. In this thesis the mass scales of sterile neutrinos range in the eV and keV regime, thus the forth mass eigenstate can no longer be incorporated into an effective mass term as in equation 2.11, but leads to a distinct β-decay spectrum. Using the equations 2.9 & 2.11, and by writing $U_{\mathrm{e,eff}} = \cos^2\theta$ and $U_{\mathrm{e},4} = \sin^2\theta$ we get:

$$\begin{aligned} \frac{\mathrm{d}N}{\mathrm{d}E} \propto \cos^2\theta \cdot \sqrt{(E_0 - E)^2 - m_{\mathrm{eff}}^2} \cdot \Theta(E_0 - E - m_{\mathrm{eff}}) \\ + \sin^2\theta \cdot \sqrt{(E_0 - E)^2 - m_4^2} \cdot \Theta(E_0 - E - m_4) \end{aligned} \tag{2.12}$$

Finally, one needs to consider that the daughter molecule can be left in an electronic or molecular excited state. The excitation energy is missing the β-decay energy and needs to be taken into account. Here we implemented the final state distributions according to [Dos14; Sae00].

For the KATRIN experiment only the last 30 eV of the energy spectrum are of importance and thus scanned with a specific time distribution for each value qU. The reference measurement time distribution is illustrated in figure 2.8 (top) and covers and interval of [−30 eV, 5 eV] around the spectrum endpoint.

Table 2.1.: Standard parameter values used in the spectrum calculation. The measurement time distribution is illustrated in figure 2.8.

effective data time	3 years
background rate	10 mcps
Tritium Q-value	18.575 keV
decay in WGTS	$8.94 \cdot 10^{10}$ cps
detector efficiency	90%
measurement time dist.	reference dist. [−30 eV, 5 eV]
source magnetic field	$B_{\mathrm{WGTS}} = 3.6\,\mathrm{T}$
pinch magnetic field	$B_{\mathrm{pinch}} = 6\,\mathrm{T}$
analysis plane magnetic field	$B_{\mathrm{ana}} = 0.3\,\mathrm{mT}$
energy resolution MAC-E Filter	0.93 meV

2.2.3. eV-scale sterile neutrino search

For the KATRIN experiment, the tritium β-decay energy spectrum is measured in a small region $E_e \in (E_0 - 30\,\mathrm{eV}, E_0 + 5\,\mathrm{eV})$ around the endpoint E_0. Since the impact of eV-scale sterile neutrinos is expected to be in the region of $E_e - E_0 \in (-10\,\mathrm{eV}, 0\,\mathrm{eV})$, the integral measurements of KATRIN would allow to directly investigate the existence of eV-scale sterile neutrinos without changing the experimental setup.

Signature

Similar to the effect of different electron antineutrino masses, the energy spectrum of a sterile neutrino is shifted according to the forth mass eigenvalue m_4 (see figure 2.4). This energy spectrum is superimposed, with a certain mixing angle, to the three flavor scenario energy spectrum, according to equation 2.12.
In order to visualize the energy spectrum branch, originating from the sterile neutrino, it is suitable to divided the 3+1 flavor model by the nominal 3 flavor model, i.e. dividing the case of sterile neutrino mixing with no mixing, as illustrated in figure 2.9. The figure shows a sterile neutrino mixing of $\sin^2\theta = 10\%$, consequently the ratio strongly deviates from the no mixing scenario ($\sin^2\theta = 0\%$) at the position above the impact of the sterile neutrino mass $qU - E_0 > -m_4$. At the position $qU - E_0 < -m_4$ the rate of the additional sterile neutrino energy spectrum starts to increase the total rate, thus increasing the ratio.

Sensitivity

According to equation 2.12, the sterile neutrino is defined by the parameters $\sin^2(\theta)$, also called the mixing amplitude, and the sterile neutrino mass eigenvalue m_4. Hence sensitivity studies span the parameter space of $\sin^2(\theta)$ and m_4, only, to match the commonly used notation from neutrino oscillation, i.e. mixing of $\sin^2(2\theta)$ and the squared mass difference Δm^2_{14} (see figure 2.3), the parameter space is adjusted accordingly:

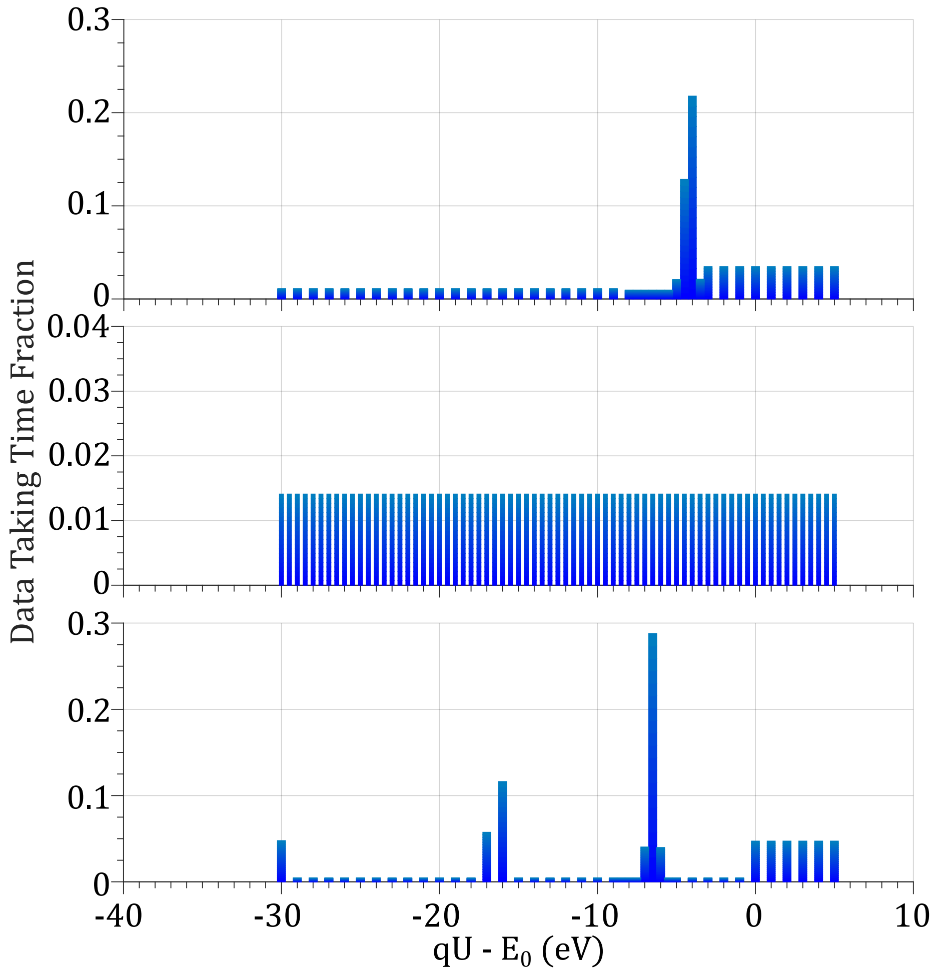

Figure 2.8.: Measurement time distributions for the KATRIN experiment in the region [−30 eV, 5 eV] near the spectrum endpoint. Reference measurement time distribution [Ang05] (top). Flat time distributions in steps of 0.5 V (middle). Optimized time distribution for measuring the active neutrino mass [Kle14] (bottom).

$$\sin^2(2\theta) = 1 - (1 - 2 \cdot \sin^2\theta) \qquad \Delta m^2_{14} \approx m^2_4. \tag{2.13}$$

Sensitivity studies for eV-scale sterile neutrinos typically assume a zero masseigenvalue of $m_1 = 0$ eV. Precedent sensitivity studies can be found in [For11; Rii11; Kle14].
The sensitivity curve is best understood by comparing the sensitivity contour with the corresponding electron statistics (see figure 2.4). For a constant background rate over energy, the signal over noise ratio is worst at the energy spectrum endpoint and best at the highest distance to the spectrum endpoint.

In this thesis, sensitivity studies for eV-scale sterile neutrinos were extended, to include a combined analysis with the SOX experiment (chapter 3. In a dedicated section the impact of experimental parameters and systematical uncertainties, as well as the discovery

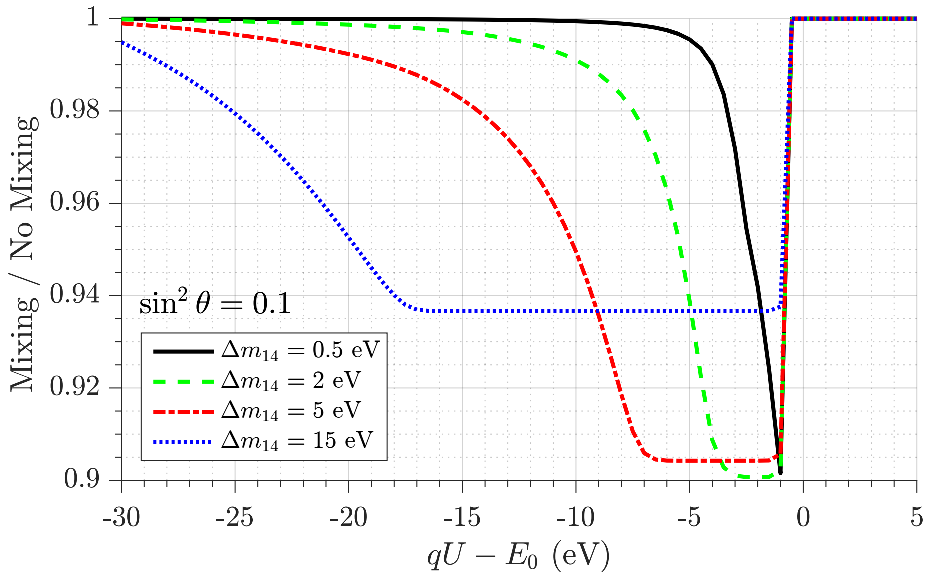

Figure 2.9.: Ratio of spectra with mixing ($\sin^2(\theta) = 0.1$) over no mixing ($\sin^2(\theta) = 0$). With higher Δm_{14} the impact to the rate at the spectrum endpoint $qU - E_0 = 0$ reduces.

potential to best fit value from the React Antineutrino Anomaly is studied (section 3.2). Moreover, in another section, the impact of eV-scale sterile neutrinos to the standard mass measurement of the KATRIN experiment is investigated 3.4.

2.2.4. keV-scale sterile neutrino search

Signature

A keV-scale sterile neutrino affects the tritium β-decay spectrum similar to the eV-scale sterile neutrino. An additional energy spectrum is superimposed to the nominal three flavor spectrum (equation 2.12). The sterile neutrino spectrum is shifted by the mass of the sterile neutrino, thus generating a kink like structure at $E_e - m_4$. A typical superimposed sterile neutrino spectrum is illustrated in figure 2.11.

Typical sterile neutrino parameters, as predicted from cosmological constraints (see figure 1.7), allow mixing angles of $\sin^2(2\theta) \in [10^{-7}, 10^{-13}]$ and mass eigenvalues of $m_4 \in [1\,\text{keV}, 50\,\text{keV}]$.

Sensitivity

Recent sensitivity analysises, a spectral fit approach [Mer15a] and a wavelet approach [Mer15b] show, that, using the full tritium source strength available at KATRIN, statistical sensitivities $\sin^2(\theta) \approx 10^{-8}$ ($m_4 = 10\,\text{keV}$) are achievable (see figure 2.12).

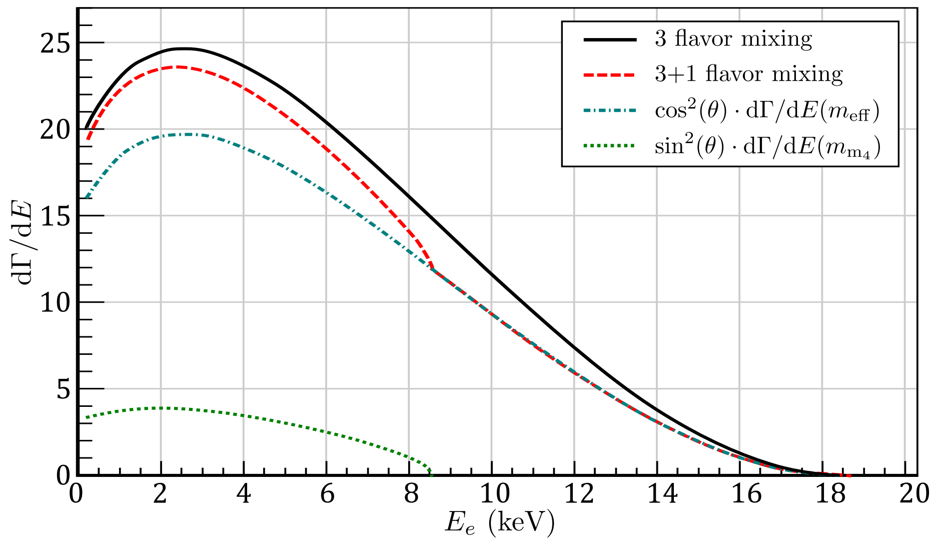

Figure 2.10.: Signature of a keV-sterile neutrino, with an exaggerated mixing angle $\sin^2\theta = 0.1$ and mass $m_4 = 10\,\mathrm{keV}$. A sterile neutrino would induce a kink like structure at $E_0 - m_4$.

The TRISTAN-project

The TRISTAN group at KATRIN, short for TRitium Investigation of STerile to Active Neutrino mixing, investigates the technical realization of the keV-scale sterile neutrino search with KATRIN. TRISTAN allows to investigate a mass range $m_4 \in [0\,\mathrm{keV}, 18.6\,\mathrm{keV}]$, but this would require a measurement of the whole β-decay energy spectrum, and thereby increase the electron rate at the detector by a factor of $> 10^8$. Moreover, in order to be sensitive to mixing angles in the per million regime and less, an unprecedented understanding of systematical effects, such as non adiabaticity [Hub15], non linearities of the electronic read-out [Dol16] and detector backscattering (section 4.1, have to be achieved. Currently, the TRISTAN team considers a two-stage approach:

1. Pre-KATRIN:
   The Pre-KATRIN scenario aims to improve the current laboratory limits after a few days of measurement, by using the KATRIN setup with only slight experimental modifications. In particular, to allow measuring the whole β-decay spectrum, the retarding potential of the spectrometers must be set to a low value $U < 1\,\mathrm{kV}$, and the tritium source strength must be reduced by about factor of 10^5, since the FPD only allows a limited counted rate of 100 kcps.

2. Post-KATRIN
   The Post-KATRIN scenario aims at the regime of mixing angles below $\sin^2(\theta) = 10^{-6}$. Therefore the whole source strength is required, which implies a stark modification of the KATRIN experimental setup, in particular a new detector is needed, which can handle the full electron rate.

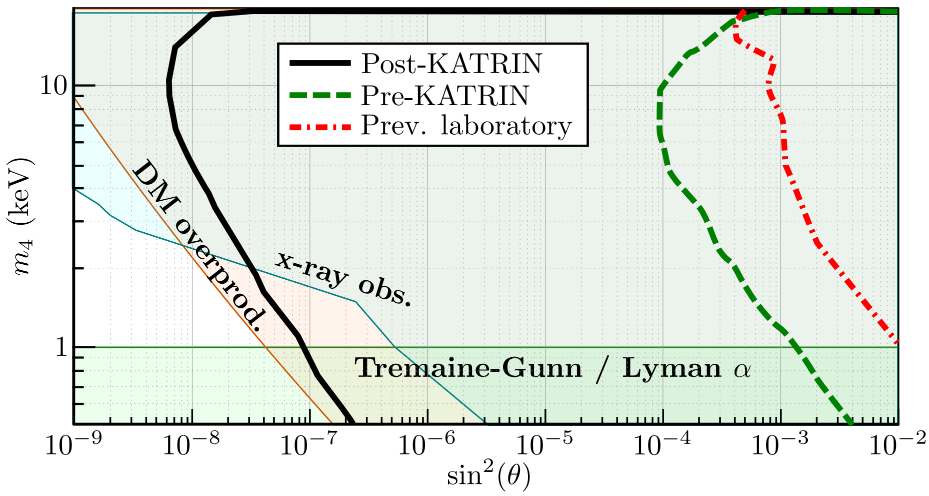

Figure 2.11.: Expected sensitivity to the keV-scale sterile neutrino with KATRIN. The Pre-KATRIN (Post-KATRIN) phase is based on 7 days (3 years) measurement time and a reduced (full) source strength by a factor of 10^5 (1). Current laboratory limits are marked in red. Figure based on analysis from [Mer15a].

The Post-KATRIN detector

In collaboration with the HalbLeiter Labor Munich (HLL) and the Lawrence Berkeley National Laboratory (LBNL), we currently work on new pn-type silicon drift prototype detectors. Each prototype detectors consists of 7 hexagonal pixels, and each pixel has a small read-out contact in the center and several drift rings positioned around the read-out contact. The first batch of prototype detectors from HLL are shown in figure 2.13.

While designing the prototype detectors, we considered the following criteria:

- High rates
  The KATRIN source allows for a maximum decay rate of 10^{11} cps, respectively 10^{10} cps at the detector. Consequently the detector is required to have small processing times for each event, i.e. small shaping times $\lesssim \mathcal{O}(\mu\text{s})$, and to have a large number detector pixels, about $\mathcal{O}(10^4)$.

- Energy resolution
  In order to be sensitive to the kink-like signature of sterile neutrinos [Mer15b], it is viable to have energy resolutions in the regime of FWHM = 300 eV (E_e = 18.6 keV. In order to maximize the detector resolution, the detector is required to have a small dead layer $\mathcal{O}(10\,\text{nm})$ and low electronic noise FWHM = $\mathcal{O}(300\,\text{eV})$. Moreover, post acceleration of the electrons would shift the β-decay energy spectrum to higher energies and thus improve the energy resolution of the detector

$$\text{FWHM} = 2\sqrt{2\ln(2)} \cdot \sqrt{f E_{\text{eh}} E_e}, \tag{2.14}$$

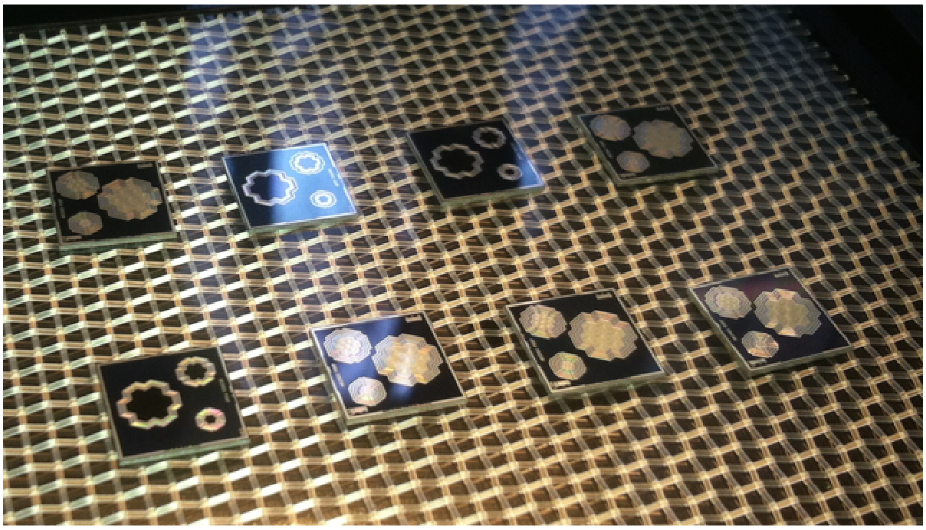

Figure 2.12.: Picture of the prototype detectors produced at the HalbLeiter Labor in Munich (HLL). Each detector chip holds three 7 pixel prototype designs. The designs differ in size and the number of drift rings.

where E_e is the energy of the incident electron, E_{eh} is the energy to produce electron hole charge carriers in the drift detector and f is the Fano factor [Fan47; Ali80].

Within this thesis, the general layout of this new detector is investigated. In particular the effect of electron backscattering is studied in detail.

3. eV-scale sterile neutrino search with KATRIN and SOX

Beyond a direct determination of the neutrino mass with high sensitivity, KATRIN has the potential to search for eV-scale sterile neutrinos.
This chapter first gives an overview of the analysis procedure used to search for the electron antineutrino mass and the eV-scale sterile neutrino with KATRIN. The second section is dedicated to study the sensitivity to eV-scale sterile neutrinos in detail, in particular the impact of experimental parameters and systematical effects are investigated. Moreover, the discovery potential to the best fit eV-scale sterile neutrino from the Reactor Antineutrino Anomaly with the KATRIN experiment is presented.
In the third section the analysis is extended by using prospective SOX data for a joint analysis with KATRIN. Finally the impact of a possibly existing eV-scale sterile neutrino on the neutrino mass sensitivity of KATRIN is presented in section four.

3.1. Analysis method

To determine the sensitivity of KATRIN to both the neutrino mass and sterile neutrinos the χ^2 method is used [Oli14], with regards to an asymptotic data set [Cow11], i.e. an averaged data set is used instead of statistically fluctuating data. The spectrum calculation was implemented according to the procedure described in section 2.2.2 and the corresponding simulation input parameters are listed in table 2.1.
In this section the χ^2 method is introduced, along with the method to calculate the sensitivity of the electron antineutrino, and the sensitivity of the sterile neutrino.

3.1.1. χ^2 test

The χ^2 function is given by:

$$\chi^2 = \sum_i \left(\frac{N_i^{\mathrm{ex}} - N_i^{\mathrm{th}}}{\sigma_i^{\mathrm{th}}} \right)^2 \tag{3.1}$$

N_i^{ex} denotes the experimental data, N_i^{th} denote the theoretical expectation and σ_i^{th} is the theoretical standard deviation. The index i corresponds to the number of independent

Table 3.1: Values of $\Delta\chi^2$ corresponding to a Confidence Level (C.L.) or Gaussian coverage in terms of multiple standard deviations (std. dev.). The parameter m denotes the number of estimated parameters.

C.L. (%)	std. dev. (σ)	m=1	m=2	m=3
68.27	1.000	1.00	2.30	3.53
90.00	1.645	2.71	4.61	6.25
95.00	1.960	3.84	5.99	7.82
95.45	2.000	4.00	6.18	8.03
99.00	2.576	6.63	9.21	11.34
99.73	3.000	9.00	11.83	14.16

measurements. In the case of KATRIN the index i denotes the different retarding potentials U_i used for the measurement.
The confidence region is derived from $\Delta\chi^2$:

$$\Delta\chi^2(\vec{\theta}) \geq \chi^2(\vec{\theta}) - \chi^2_{\mathrm{min}} \tag{3.2}$$

Where $\vec{\theta}$ is a vector of parameters, defining the hypothesis, i.e. parameters that are estimated. For Gaussian distributed measurements the values for $\Delta\chi^2$ can be calculated from a multivariate Gaussian and depend on the number of estimated parameters m and the coverage probability, i.e the confidence level (see table 3.1).

In order to investigate the impact of systematic errors it is useful to introduce nuisance parameters $\vec{\nu}_{\mathrm{p}}$ to the χ^2 function

$$\chi^2(\vec{\theta}) \rightarrow \chi^2(\vec{\theta}|\vec{\nu}_{\mathrm{p}}) \qquad \vec{\theta} \rightarrow \vec{\theta} = \vec{\theta}_0 - \vec{\nu}_{\mathrm{p}}, \tag{3.3}$$

where $\vec{\theta}_0$ denotes a vector of true parameter values. Nuisance parameters add an additional uncertainty during the minimization of the χ^2 function and thus increase the statistical uncertainty.

3.1.2. Analysis for the electron antineutrino

In the following the 90% CL at which a certain neutrino mass can be excluded by the KATRIN experiment will be calculated. The estimated parameter is the neutrino mass m^2_{eff}: $\vec{\theta} = (m^2_{\mathrm{eff}})$. Furthermore, the overall signal rate N, the background rate B, and the energy endpoint Q are used as nuisance parameters $\vec{\nu}_{\mathrm{p}} = (N, B, Q)$, since they are not known with sufficient precision. The test function becomes:

$$\chi^2(m^2_{\mathrm{eff}}|N, B, Q) = \sum_i \frac{\left(\Gamma_{\mathrm{ex},i}(0\,\mathrm{eV}^2|N, B, Q) - \Gamma_{\mathrm{th},i}(m^2_{\mathrm{eff}}|N, B, Q)\right)^2}{\sigma^2_{\mathrm{th},i}(m^2_{\mathrm{eff}}|N, B, Q)}, \tag{3.4}$$

where Γ_i denotes the integral spectrum at different retarding potentials U_i. The test function is minimized with respect to the nuisance parameters for each fixed value of the

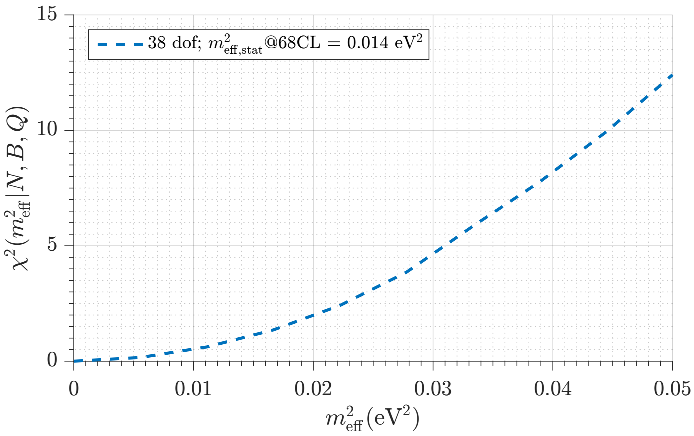

Figure 3.1: Test function $\chi^2(m^2_{\mathrm{eff}}|N,B,Q)$ with the nuisance parameters (N,B,Q) and the test parameter m^2_{eff}. The statistical sensitivity at 68% CL on m^2_{eff} can be derived from the equation $\Delta\chi^2(m^2_{\mathrm{eff}}) \stackrel{!}{=} 1$.

test parameter m^2_{eff}. The result is plotted in figure 3.1.

As expected from equation 3.1, the test function χ^2 increases for larger values of m^2_{eff}. For $m^2_{\mathrm{eff}} = 0\,\mathrm{eV}^2$ the numerator in equation 3.1 becomes zero, while increasing values $m^2_{\mathrm{eff}} > 0$ results in an increasing spectral shift near the endpoint (see figure 2.4) and thus a higher difference in the numerator.
A neutrino mass m_{eff} can be excluded with 68% CL (assuming that experimental data shows a zero neutrino mass), if $\Delta\chi^2$ is equal to one (table 3.1).
Including the systematical error $\sigma^2_{\mathrm{sys}}(m^2_{\mathrm{eff}}) = 0.017\,\mathrm{eV}^2$ as estimated in [Ang05], the total error $\sigma_{\mathrm{tot}}(m^2_{\mathrm{eff}})$ can be calculated.

$$\sigma^2_{\mathrm{tot}} = \sigma^2_{\mathrm{stat}} + \sigma^2_{\mathrm{sys}} \tag{3.5}$$

The 90% CL neutrino mass sensitivity for the antineutrino is then given by:

$$m_{\mathrm{eff}}@90CL = \sqrt{1.645 \cdot \sigma_{\mathrm{tot}}(m^2_{\mathrm{eff}})} \approx 190\,\mathrm{meV} \tag{3.6}$$

The KATRIN design value was calculated with the method of ensemble testing and predicts a mass sensitivity of $m_{\mathrm{eff}}@90CL < 200\,\mathrm{meV}$ [Ang05].

3.1.3. Analysis for the sterile neutrino

In the case of eV-sterile neutrinos, the interesting parameters are the mixing angle $\sin^2(\theta)$ and the sterile neutrino mass m_4. To facilitate the analysis, the effective anti neutrino mass is set to zero $m^2_{\mathrm{eff}} = 0$. We are now looking at the case of two free parameters $m = 2$ and the test function is modified accordingly:

$$\chi^2(m^2_{\mathrm{eff}}|N,B,Q) \xrightarrow{m^2_{\mathrm{eff}}=0\,\mathrm{eV}^2} \chi^2(m^2_4, \sin^2(\theta)|N,B,Q) \tag{3.7}$$

In the case of $m = 2$, the 90% CL can be found at $\Delta\chi^2 = 4.6$, see table 3.1. Figure 3.2 shows the 90% CL sensitivity of KATRIN to eV-scale sterile neutrinos. The sensitivity line

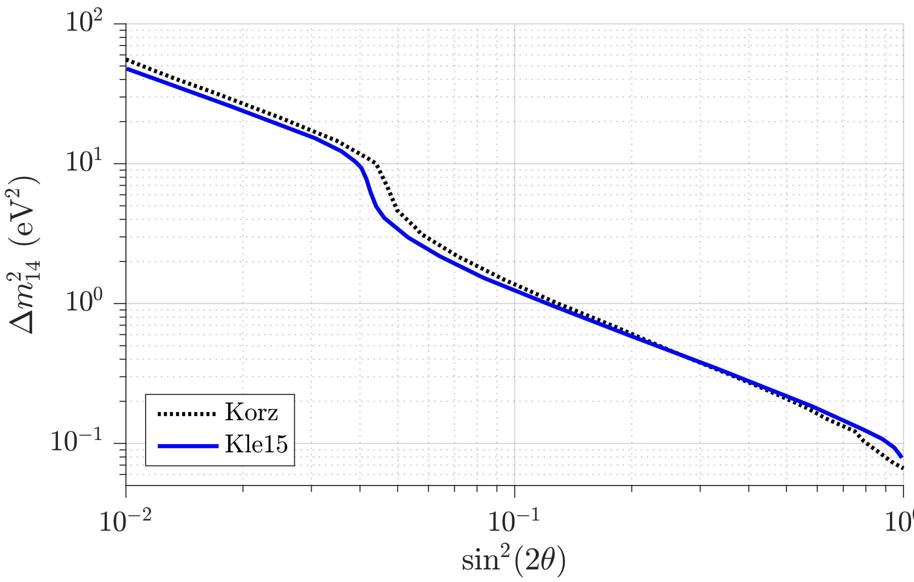

Figure 3.2.: The figure shows the 90% exclusion limit of KATRIN for sterile neutrinos. The axis are scaled to typical observables from neutrino oscillations: $\sin^2(2\theta)$ and $\Delta m^2_{41} = m^2_4 - m^2_1$. The result is in good agreement with [Kle14] and both exclusion curves include a systematic error on the sterile neutrino mass $\sigma^2_{\text{sys}} = 0.017\, eV^2$, added in quadrature.

is intuitively understood by considering the properties of the tritium β-decay spectrum (see figure 2.4). For sterile neutrino masses in the sub-eV region the sterile neutrino signature is near the spectrum endpoint and thus yields only small amount of statistics. For sterile neutrino masses of a few eV, the sterile neutrino signature is further away from the spectrum endpoint and resides in a region of higher electron statistics. The deviation from the nominal is thus better visible and yields higher sensitivities.

3.2. Sterile neutrino sensitivity

Up to this point a zero effective neutrino mass $m^2_{\text{eff}} = 0\,\text{eV}$, a fixed measurement time schedule, a fixed background rate $B = 10\,\text{mcps}$ was assumed.
The first part of this section is dedicated to investigate the impact of experimental parameters, e.g. a non-zero neutrino mass, and systematic uncertainties to the eV-scale sterile neutrino sensitivity. In the second part the discovery potential to the best fit value from the Reactor Antineutrino Anomaly with the KATRIN experiment is discussed.

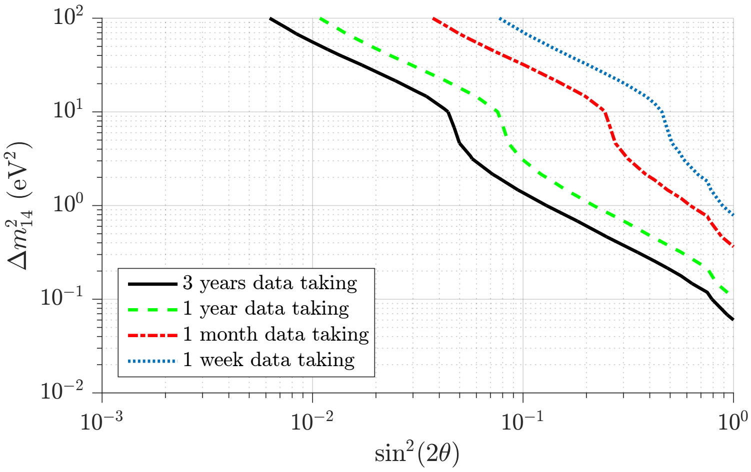

Figure 3.3: Sensitivity to eV-sterile neutrino with regards of the effective data taking time. The sensitivity scales proportional to the square root of the data taking time.

3.2.1. Experimental parameters and systematic uncertainties

Measurement time and distribution

As a first step the impact of the measurement time is investigated. Different measurement times directly result in a change of statistics, and hence the sensitivity improves proportional to the square root of the measurement time. (see figure 3.3)

Figure 3.4 shows the dependence on the used measurement time distribution. The KATRIN measurement time distribution, shown in figure 2.8 (top) is optimized for the neutrino mass measurement. As the signature of a sterile neutrino is not expected at the same position in the spectrum as the signature of the neutrino mass, we investigate whether a modified measurement time distribution can impact the sterile neutrino sensitivity. Here, we consider three different cases:

- Reference time distribution (see figure 2.8 (top)):
  Distribution proposed in the KATRIN design report [Ang05], especially focusing on the region near the endpoint. In this region the signature of the active neutrino mass is expected and the signal over background ratio bigger than one. The background rate is additionally measured at the region of [0 eV, 5 eV] above the energy endpoint E_0.
- Flat time distribution (see figure 2.8 (middle))
  The flat time distribution does not focus on a certain region of the tritium β-decay spectrum. The spectrum is scanned in 0.5 V voltage steps, within the region of [−30 eV, 5 eV] near the endpoint.
- Optimized distribution for active neutrino mass measurement by Marco Kleesiek [Kle14] (see figure 2.8 (bottom))
  This time distribution allows further regions with enhanced focus. The region at −30 eV yields the highest statistics and thus the lowest relative error. Sufficient statistics are needed to precisely determine the energy endpoint of the spectrum E_0. The high data taking time region around −17 eV helps to disentangle the two

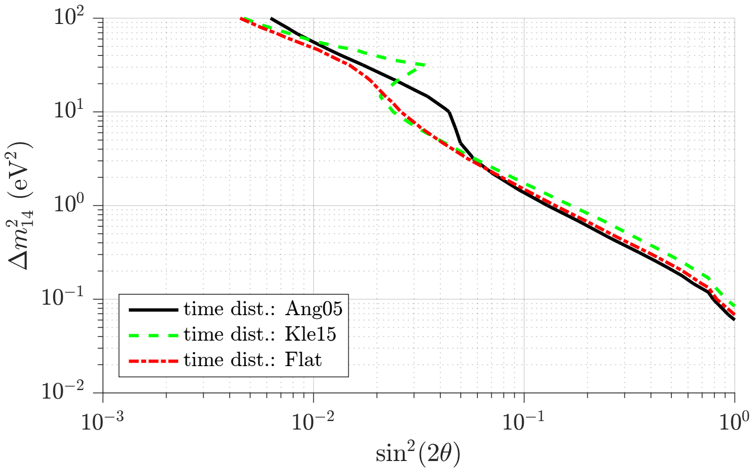

Figure 3.4: Sensitivity to eV-sterile neutrino with regards to the underlying measurement time distribution (see figure 2.8. The flat distribution gives a slight improvement at higher masses Δm^2_{14}, as it does not focus on the low mass regime and thus yields higher statistics at high masses.

parameters spectrum endpoint E_0 and normalization N. The region near the endpoint −8 eV and above the endpoint 0−5 eV focus on measuring the neutrino signature and the background rate.

The different measurement time distributions show only slight sensitivity differences. As expected, the flat distribution improves the limit slightly at higher masses, whereas it is less sensitive for lower masses of the sterile neutrino m_4^2. This directly correlates to the event statistic taken at different retarding potential values U.

Uncertainties on the signal rate, background rate and endpoint value

The overall rate, the background rate, and the energy endpoint will not be known with sufficient precision, hence they are used as nuisance parameters in the fit. Here, the effect of these additional nuisance parameters on the sterile neutrino sensitivity is demonstrated. Figure 3.5 shows the reference sensitivity $\chi^2 \equiv \chi^2(m_4^2, sin^2(\theta)|N, B, Q)$ and the scenarios of only one nuisance parameter, e.g. $\chi^2 \equiv \chi^2(m_4^2, sin^2(\theta)|N)$. The biggest influence originates from the energy endpoint, here denoted with Q, as it can directly mimic the effect of a shifted β-decay spectrum, which normally complies only to non-zero neutrino masses. In comparison the uncertainty on the overall normalization N and on the background rate B is less important, as the impact of the nuisance parameters on the sterile neutrino sensitivity is smaller.

Enhanced background rate

As a next step the impact of the background rate to the sterile neutrino sensitivity is investigated. Only a tiny fraction of all β-decays produce electrons in the region of interest, i.e. close to the spectrum endpoint (10^{-11} % in the last eV). Consequently, the background rate has to be equivalently low. Figure 3.6a shows the signal of a 2 eV sterile neutrino with a mixing angle of $\sin^2\theta = 0.1$, for different background rates. Interestingly, whereas the neutrino mass sensitivity does not too strongly depend on the background rate ($\approx B^{1/6}$) [Ang05], the impact of background on the sterile neutrino signal is crucial (see table 3.2).

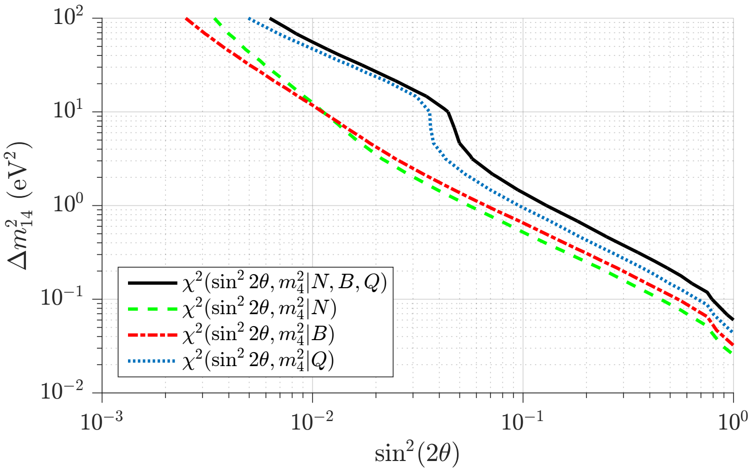

Figure 3.5: Sensitivity to an eV-scale sterile neutrino, with regards to a different set of nuisance parameters $\vec{\nu}_p$. The biggest impact on the sterile neutrino sensitivity originates from the uncertainty on the energy endpoint Q.

The 90% CL, shown in figure 3.6b, is shifted by a factor of ≈ 2 for a background level of $B = 100$ mcps compared to the reference 90% CL sensitivity line with $B = 10$ mcps.

Table 3.2.: Background rate dependence of the active neutrino mass sensitivity.

B (mcps)	0	1	10	100
$\sigma(m^2_{\text{eff}}@90CL)$ (meV)	174	178	190	238

Non zero active neutrino mass

In the previous paragraphs we have assumed the active neutrino mass to be zero. However, a non-zero active neutrino mass can impact the sensitivity to detect sterile neutrinos.

Figure 3.7a shows the ratio of a β-decay spectrum with a sterile neutrino ($m_4 = 2\,\text{eV}, \sin^2\theta = 0.1, m_{\text{eff}} = 0\,\text{eV}$) divided by a reference spectrum without sterile neutrinos but for different effective neutrino masses $m_{\text{eff}} = 0, 0.1, 0.5, 1\,\text{eV}$.
For increasing neutrino masses m_{eff} the area above the ratio lines decreases and is zero when $m_{\text{eff}} = m_4$. Intuitively we can predict that an overlap of the two masses $m_{\text{eff}} = m_4$ also yields a zero sensitivity to the sterile neutrino, since we would not be able to distinguish the sterile from the active neutrino.
In figure 3.7b the 90% CL contours for different effective neutrino masses m_{eff} are illustrated. Again, a mass overlap $m_{\text{eff}} = m_4$ results in zero sensitivity, i.e. mixing angle $\sin^2\theta = 0$. For masses $m_{\text{eff}} \neq m_4$ the sensitivity increases with the distance to the effective neutrino mass. For $\Delta m^2_{14} \gg m^2_{\text{eff}}$ the sensitivity contours converge to the reference sensitivity ($m_{\text{eff}} = 0$).

3.2.2. Discovery potential

So far we have only considered exclusion limits, i.e. the case that KATRIN does not detect a sterile neutrino signal and sets a limit on the sterile neutrino mass and mixing. Here we consider the discovery potential with which KATRIN could detect a sterile neutrino of a certain mass and mixing angle. The discovery potential is calculated with the same

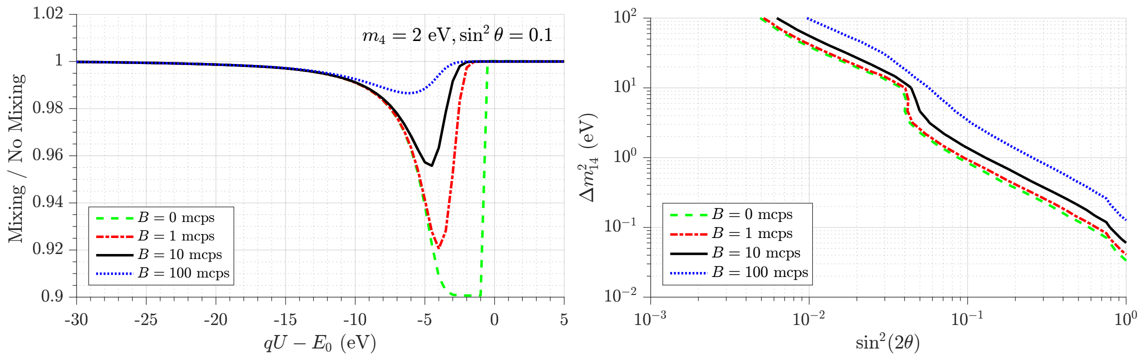

(a) spectrum ratio

(b) sensitivity

Figure 3.6.: a: Influence of the background rate B to the signature of a sterile neutrino with $\sin^2\theta = 0.1$ and $m_4 = 2\,\text{eV}$ (mixing). The label "no mixing" denotes a spectrum without sterile neutrino: $\sin^2\theta = 0$. b: Influence of the total background rate B to the sensitivity of eV-scale sterile neutrinos. The reference background rate is depicted in black, $B = 10\,\text{mcps}$.

method as an exclusion limit, but the zero hypothesis has a non-zero sterile neutrino mass and mixing angle.

$$\chi^2(\sin^2(2\theta), m_4^2|N, B, Q) = \\ = \sum_i \frac{\left(\Gamma_{\text{ex},i}(0.14, 2.3\,\text{eV}^2|N, B, Q) - \Gamma_{\text{th},i}(\sin^2(2\theta), m_4^2|N, B, Q)\right)^2}{\sigma^2_{\text{th},i}(\sin^2(2\theta), m_4^2|N, B, Q)} \tag{3.8}$$

The experimental integral spectrum $\Gamma_{\text{ex},i}$ is calculated with the assumption of an existing sterile neutrino. In this work, we consider the case of the best fit value for the sterile neutrino parameters, based on the Reactor Antineutrino Anomaly [Men11]. Minimizing equation 3.8 and drawing 68/90/99% CL contour lines gives the discovery potential illustrated in figure 3.8.

The discovery region is strongly aligned to the reference sensitivity curve, since the relative uncertainty on the signal rate is lower near the energy spectrum endpoint (see figure 2.4). Comparing the theory to the experiment in the χ^2-test function (equation 3.8), results in lower χ^2-values for $\Delta m^2_{14} < 2$ than for $\Delta m^2_{14} > 2$. Consequently, the discovery potential contour, i.e. the isolines $\Delta\chi^2(\sin^2(2\theta), \Delta m^2_{14}) \stackrel{!}{=} \text{const}$ (equation 3.2), are diagonally deformed in direction of lower masses and mixing angles.
In conclusion, the KATRIN experiment is sensitive to the best fit value of the Reactor Antineutrino Anomaly. In contrast, the KATRIN experiment would not be sensitive to a sterile neutrino, with parameters in the regime of $\sin^2(2\theta) \ll 0.14$ and $m_4^2 \ll 2\,\text{eV}^2$.

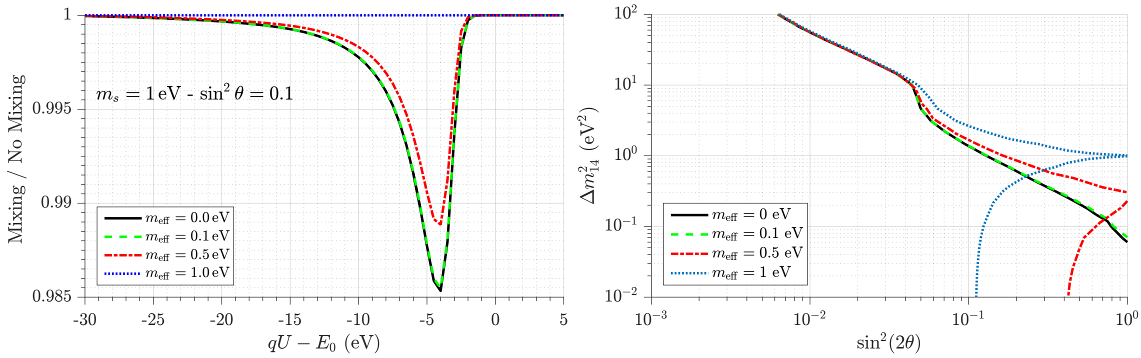

(a) spectrum ratio (b) sensitivity

Figure 3.7.: Effect of a non zero effective neutrino mass to the β-decay spectrum (a) and to the sensitivity to eV-scale sterile neutrinos (b). If the two masses overlap $m_{\mathrm{eff}} = m_4$, the sterile neutrino signature is not visible in the spectral ratio, hence sharply reducing the sensitivity around $m_{\mathrm{eff}} \approx m_4$.

3.3. Combined sensitivity of KATRIN and SOX

Both SOX (fig. 2.3) and KATRIN [Kle14] have the possibility to probe the Reactor Antineutrino Anomaly. Moreover, the two experiments explore different sterile neutrino parameter regimes:

- KATRIN (section 2.2.3):
  For the KATRIN experiment, the mixing amplitude $\sin^2(\theta)$ determines the probability of the creation of a tritium β-decay according to the mass eigenvalue m_4. As the tritium β-decay rate increases further away from the endpoint, KATRIN can probe large values of $\Delta m^2_{14} > 2\,\mathrm{eV}^2$ down to very small mixing angles. For small values of $\Delta m^2_{14} < 2\,\mathrm{eV}^2$ the signal to background ratio of KATRIN becomes too small, thus reducing the sensitivity to a sterile neutrino.

- SOX (section 2.1):
  For the SOX experiment, the scale of L/E, where, depending on the squared mass difference Δm^2_{14}, the oscillation from electron antineutrinos to a sterile flavor occurs (equation 1.4), is of importance. SOX covers L/E range if 1.5–6.5 m/MeV (see figure 2.2). In this regime, the oscillation into sterile neutrinos is most distinct for $\Delta m^2_{14} \approx 0.3$–$1\,\mathrm{eV}^2$. For small values $\Delta m^2_{14} < 0.1\,\mathrm{eV}^2$, the emitted antineutrino has yet to oscillate, resulting in a low sensitivity. For high values $\Delta m^2_{14} > 10\,\mathrm{eV}^2$ the oscillation is not correctly resolved by the detector, resulting in an averaging effect of the sinusoidal term in equation 1.4.

Consequently, the KATRIN experiment is more sensitive when probing large values $\Delta m^2_{14} > 2\,\mathrm{eV}^2$, whereas SOX is more sensitive for smaller values $\Delta m^2_{14} \approx 0.1$–$2\,\mathrm{eV}^2$. This fact strongly motivates a joint eV-sterile neutrino analysis of KATRIN and SOX. Assuming that the two experiments are uncorrelated the test function becomes:

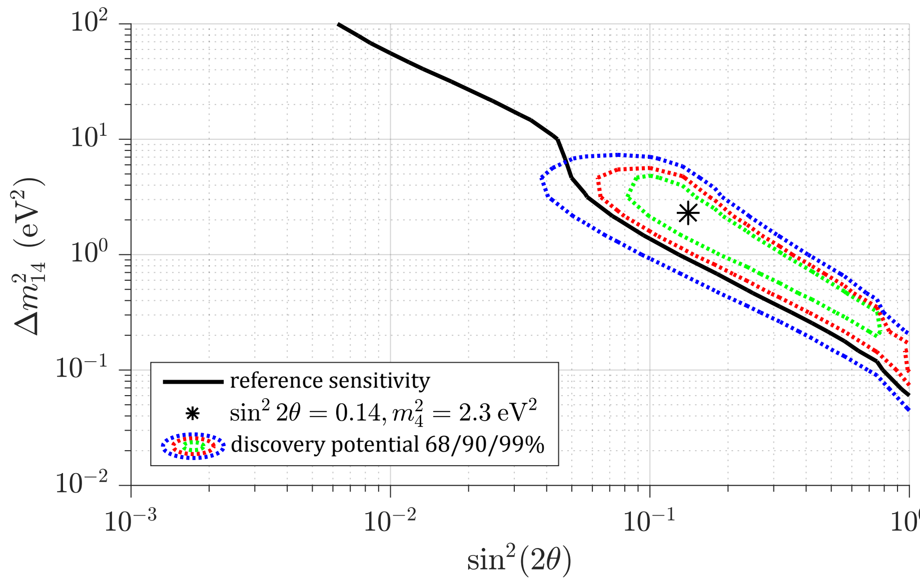

Figure 3.8.: Discovery potential for a sterile neutrino with best fit parameters indicated by the star. The best fit is based on a combination of reactor neutrino experiments, Gallex and Sage calibration sources experiments, MiniBooNE and the ILL-energy spectrum distortion [Men11]. The black solid line is the nominal KATRIN 90% CL exclusion line, whereas the discovery potential contours at a CL of 68, 90, 99% are depicted in green, red and blue.

$$\chi^2_{\text{tot}} = \chi^2_{\text{KATRIN}} + \chi^2_{\text{SOX}} \qquad \Delta\chi^2_{\text{tot}} \stackrel{!}{=} 4.61(90\%CL) \tag{3.9}$$

Figure 3.9 shows the combined sensitivity analysis from KATRIN and SOX, the combined exclusion line gains the most at the intersection point of the 90% CL lines from KATRIN and SOX. In the very low and very high Δm^2_{14} regions the 90% CL is dominated by the more sensitive experiments. Using the data from both experiments, the 95% CL suggested parameter region from the Reactor Antineutrino Anomaly can be fully explored, hence underlining the complementarity of the experiments and motivating to investigate eV-sterile neutrinos with both experiments.

3.4. Impact on the neutrino mass determination with KATRIN

We can now turn the analysis idea around and not compute the sensitivity of eV-scale sterile neutrinos with KATRIN, but estimate the impact of eV-scale sterile neutrinos on measuring the antineutrino mass with KATRIN. In this section an estimation of the minimal and maximal possible effect is presented.

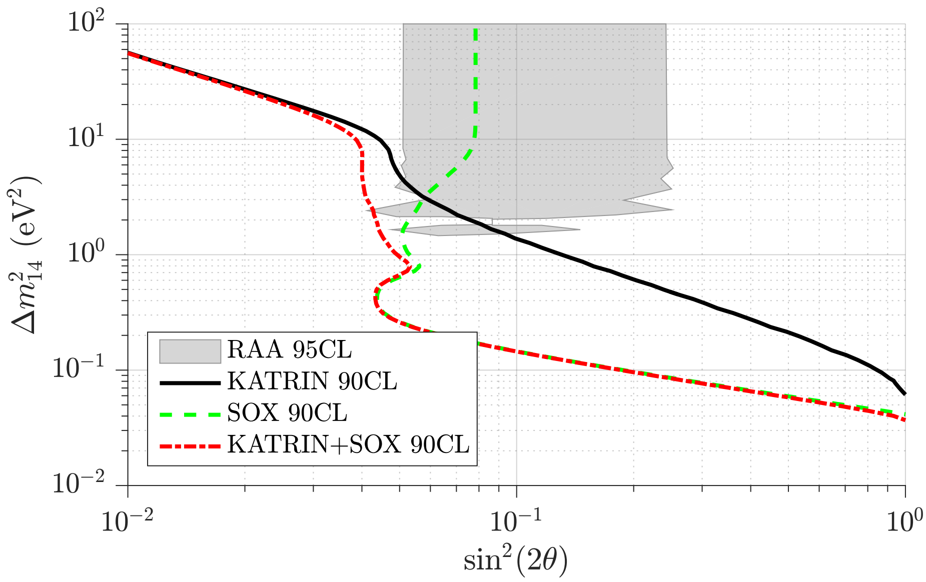

Figure 3.9.: Combined sensitivity study for eV-sterile neutrinos. The combined analysis (red) gains the most sensitivity at the intersection of the 90% CL sensitivity contours of the KATRIN (black) and SOX (green) experiment. The preferred parameter space from 95% Reactor Antineutrino Anomaly is only covered in its entirety by the combined analysis.

3.4.1. Minimal estimation

For the minimal effect estimation we assume the existence of a sterile neutrino with a certain mass and mixing angle. The spectrum including the effect of this sterile neutrino is now used to estimate the neutrino mass sensitivity as explained in section 3.1. The existence of a sterile neutrino deforms the spectrum and slightly reduces the counting rate in the region near the endpoint (see figure 2.9). Consequently, even if the sterile neutrino parameters were perfectly known, the neutrino mass sensitivity would slightly suffer from the existence of a sterile neutrino, solely due to the reduced statistics.
Or more explicitly:

1. Active neutrino mass analysis:
   We are interested in the mass of the active neutrino m_{eff}, thus for calculating the 90% CL for the neutrino mass we can directly follow the steps in section 3.1.2.
   For the calculation we assumed, that the β-decay spectrum solely consists of active neutrino and thus the sterile neutrino has: $\sin^2\theta = 0$ and $m_4 = 0$.

2. Choose sterile neutrino parameters:
   Now assume the existence of a sterile neutrino with the exact parameters $(m_4, \sin^2\theta)$. The corresponding beta spectrum would now include a distortion arising from the sterile neutrino.

$$\Gamma(\sin^2\theta = 0, m_4 = 0) \longrightarrow \Gamma(\sin^2\theta \neq 0, m_4 \neq 0) \tag{3.10}$$

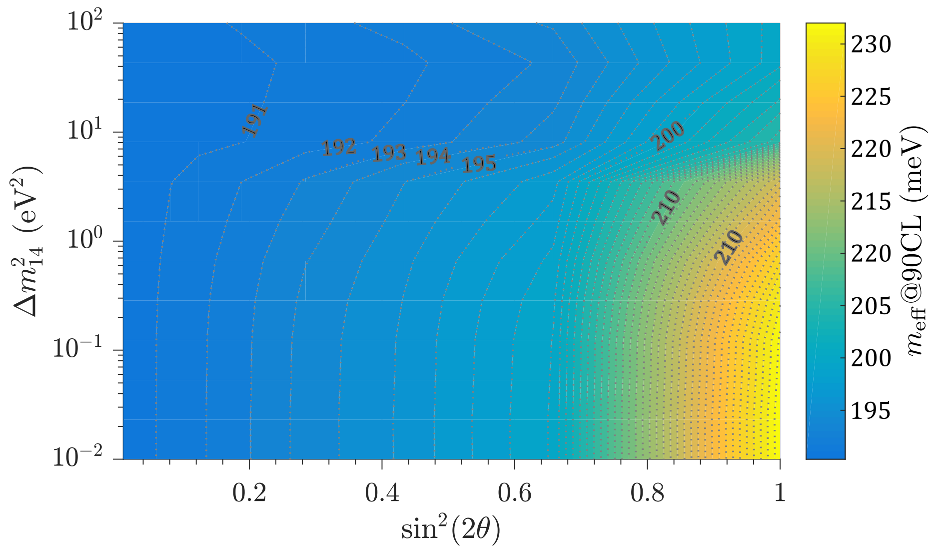

Figure 3.10.: Minimal estimation of the impact of an eV-scale sterile neutrino to KATRIN's mass measurement $m^2_{\rm eff}@90CL$. With respect to the 95% CL region of the Reactor Antineutrino Anomaly an estimate for the largest allowed impact can be deduced $m_{\rm eff}@90CL \approx 193.1\,\text{meV}$ ($\Delta m^2_{14} = 1.2\,\text{eV}^2$, $\sin^2(2\theta) = 0.22$).

x. Repeat 1 & 2:
   Go back to step 1) and repeat the analysis with the modified β-decay spectrum. In step 2) choose a different pair $(m_4, \sin^2\theta)$ and modify the spectrum. Repeat these two steps until the whole $m_4 - \sin^2\theta$ plane is covered.

Figure 3.10 shows the statistical sensitivity to the neutrino mass, assuming the existence of a sterile neutrino with a certain mass and mixing angle. As expected, the statistical neutrino mass sensitivity decreases for larger mixing angles and in particular for small sterile neutrino masses, which are closer to the active neutrino mass.

Considering the best fit value by the Reactor Antineutrino Anomaly ($\Delta m^2_{14} = 2.3\,\text{eV}^2$, $\sin^2(2\theta) = 0.14$), the neutrino mass sensitivity of KATRIN would be reduced by roughly $191.5/190 \approx 0.8\%$. In case of the largest allowed impact based on the Reactor Antineutrino Anomaly ($\Delta m^2_{14} = 1.2\,\text{eV}^2, \sin^2(2\theta) = 0.22$), the sensitivity is reduced by 1.6%. Finally, for the smallest allowed impact ($\Delta m^2_{14} = 1.2\,\text{eV}^2, \sin^2(2\theta) = 0.04$), the sensitivity loss is negligible.

3.4.2. Maximal estimation

The maximal estimation introduces two new nuisance parameters

$$\chi^2 \equiv \chi^2(m^2_{\rm eff}|N, B, Q, m^2_4, \sin^2\theta), \tag{3.11}$$

the mixing angle $\sin^2\theta$ and the squared mass m^2_4, in order to estimate the impact of a sterile neutrino to the analysis of the mass of the electron antineutrino. Details of the fitting procedure are described in appendix A.

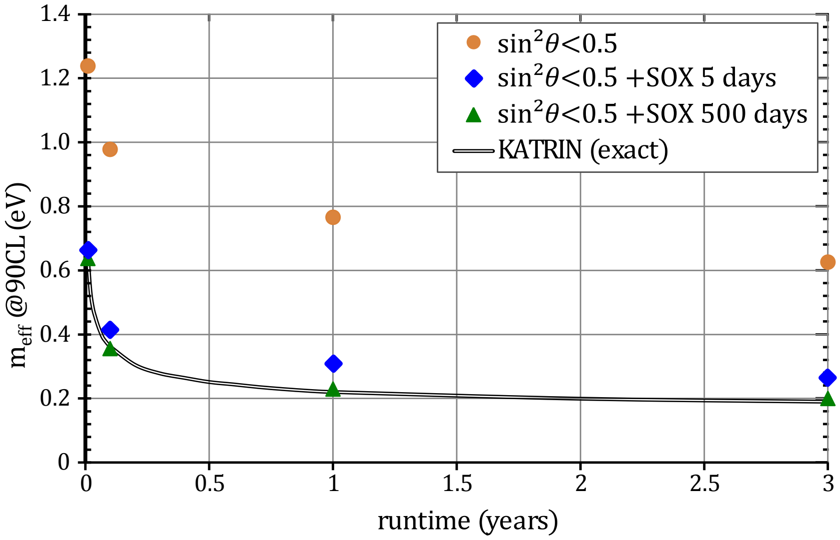

Figure 3.11.: Estimating the maximal impact of a eV-sterile neutrino to KATRIN's mass measurement. The black solid line reflects KATRIN's reference sensitivity. The yellow marker is the sensitivity when marginalizing over $\sin^2\theta$ & m_4 without any further constraints, i.e. $\sin^2(\theta) \in [0, 0.5]$. Using the 500 days χ^2-analysis from SOX [Gaf15], in a joint analysis, KATRIN's sensitivity is mostly recovered (green).

A possibility to constrain the parameter space of m_4 and $\sin^2\theta$ is the usage of physical data. Here, we assume that the SOX experiment would have completed its measurement, would provide the expected exclusion limits before KATRIN, and is uncorrelated to the KATRIN experiment. The SOX output can be then used as a constraint on the squared mass m_4^2 and mixing angle $\sin^2\theta$ in the model used by KATRIN. The test function χ^2 for the neutrino mass determination consequently includes the χ^2_{SOX}-map from SOX:

$$\chi^2 \equiv \chi^2_{\mathrm{KATRIN}}(m^2_{\mathrm{eff}}|N, B, Q, m_4^2, \sin^2\theta) + \chi^2_{\mathrm{SOX}}(\Delta m^2_{14}, \sin^2(2\theta)) \tag{3.12}$$

The relation between the observables in SOX ($\sin^2(2\theta), \Delta m^2_{14}$) and KATRIN ($\sin^2\theta, m_4^2$) is given by equation 2.13. For the lightest neutrino mass eigenstate we assumed $m_1 \ll m_4$, and hence neglect m_1. This step is valid for low effective neutrino masses $m^2_{\mathrm{eff}} = \sum_{i=1}^{3} m_i^2 \lesssim$ 100 meV as shown in figure 3.7b.

Figure 3.11 shows the neutrino mass sensitivity as a function of measurement time of the KATRIN experiment, allowing for the existence of sterile neutrino with different degrees of knowledge about their mass and mixing angle. One can see that allowing for a sterile neutrino with unknown mass and mixing angle in the fit of the tritium beta spectrum drastically reduces the neutrino mass sensitivity. This is due to the fact that the signature of

sterile neutrino and neutrino mass can be completely degenerate for low masses $m < 1\,\text{eV}$. On the other hand, adding information obtained after 5,500 days of SOX data taking on the sterile neutrino parameters, the degeneracy is broken and the neutrino mass sensitivity of KATRIN is restored.
At a runtime of 3 years and with the help of 500 days of SOX data, the relative impact of eV-scale sterile neutrinos to the neutrino mass determination is about 5%.

4. keV-scale sterile neutrino studies

Sterile neutrinos in the keV mass range are viable candidates for Dark Matter. Moreover, the existence of keV-scale sterile neutrinos are predicted in extensions of the Standard Model of Particle Physics (s. 1.3).
A keV-scale sterile neutrino would leave a small kink-like distortion in the β-decay spectrum measured at KATRIN. TRISTAN, a sub-project of KATRIN, explores the possibility of a keV-scale sterile neutrino search and currently investigates the realization of the experimental setup (s. 2.2.4).
In order to asses the tiny signature of a keV-scale sterile neutrino the entire tritium β-decay spectrum has to be recorded with high statistics and small systematic uncertainties. The KATRIN tritium source provides an unprecedented source luminosity, however, the current focal plane detector of KATRIN is not suitable to handle the corresponding counting rates, which would be 12 orders of magnitudes higher than in the normal KATRIN mode. Hence, a novel detector system has to be developed.
The two main aspects of this section are: design simulations, targeted at optimizing the novel detector system, and characterization of a first 7 pixel Si-prototype detector of the desired design.
As a first step we constrain general detector parameters, such as diameter, pixel size and pixel number, based on generic detector effects. Here we consider pile-up, charge sharing, and detector backscattering (section 4.1).
In the next step we use dedicated KASSIOPEIA simulations, to further investigate the backscattering process. Specifically, we simulate the time of flight and angular distributions of backscattered electrons for different detector positions (section 4.4).
Finally, based on these simulations, and data, based on simulations from KESS [Ren11], we develop a method for a fast calculation of the β-decay spectrum. This technique allows to "switch on" effects such as backscattering and energy threshold, and observe their effect on the spectral shape. In this framework we tested the efficiency of a backscattering veto (section 4.2).
The last section of this chapter (section 4.4) is dedicated to the first measurements with a prototype detector produced at HLL, and equipped with read-out electronics from CEA.

4.1. Detector design

In this section we consider a silicon pixel detector with the detector radius r_{det} and the pixel radius r_{px}. The number of pixels N_{px} and the rate per pixel Γ_{px} are then given by:

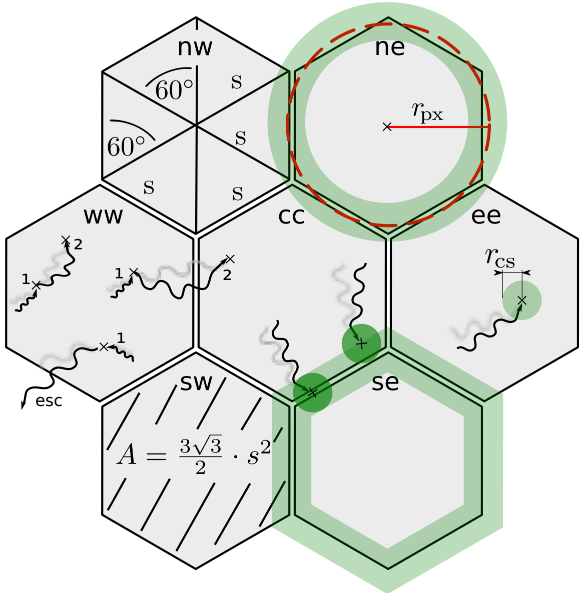

Figure 4.1: Schema of 7 hexagonal shaped pixels. Each pixel is labeled according to cardinal directions: north east *ne*, east *ee*, center *cc*, etc. In pixel *ne* the red dashed line approximates the hexagonal pixel with a round shape of the same area. The green marked regions illustrate charge clouds and sharing areas, whereas pixel *ww* shows two backscattered particles.

$$N_{px} = \frac{r_{det}^2}{r_{px}^2} \qquad \Gamma_{px} = \frac{\Gamma_{det}}{N_{px}}, \tag{4.1}$$

where Γ_{det} is the total rate of electrons at the detector. In this section these parameters are optimized with respect to the general systematic effects: pile up, charge sharing and backscattering (see figure 4.1). These three effects lead to a systematic uncertainties of the measured electron energies. Which would influence the sensitivity of the experiment. Generally, we expect, that …

- …in order to minimize charge sharing a minimal pixel size is required.
- …in order to minimize pile up a minimal number of pixels is required or the total electron rate needs to be limited.
- …in order minimize backscattering, a veto is required, and hence the detector rate is constrained.

Later we will see, that placing the detector in smaller magnetic fields, the probability of backscattering is decreased and the probability magnetic back-reflection is increased.

4.1.1. Optimization with respect to charge sharing

If an incident particle hits the detector surface the energy is deposited through elastic scattering. Adding diffusion, magnetic and electric fields, the corresponding ionized volume is enlarged and called charge cloud. The lateral expension of the charge cloud r_{cs} is in the regime of several microns $\mathcal{O}(20\,\mu\text{m})$ [Mat02] (see figure 4.1 pixel *ee*).
A particle hitting the detector near the pixel boundary, i.e. the neighboring pixel is within

the charge cloud radius r_{cs}, would result in distribution of charge between the pixels. One would thus measure a signal in both pixels.
This process is called charge sharing and depicted in figure 4.1 pixel *se*. The green highlighted area marks the region where an incident particle would trigger the neighboring pixel(s).
One might consider vetoing all events, where two or more pixels received a signal. However, for all pixels, the charge deposited is required to meet a certain threshold. Hence, an electron charge cloud split across several pixels might result in undetected energy depositions for $E_{dep} < E_{th}$.

Charge sharing model

For estimating the probability of charge sharing a simple model with constant charge clouds was used. The hexagonal pixel design presented in section 2.2.4 is approximated with a round geometry as illustrated in figure 4.1. The probability of charge sharing in this model corresponds to the area near the pixel boundary divided by the total pixel area:

$$P_{cs} = \frac{r_{px}^2 - (r_{px} - r_{cs})^2}{r_{px}^2} \tag{4.2}$$

Results

In figure 4.2 the probability of charge sharing in the plane of detector radius and pixel radius is shown. The charge sharing model on the left (right) considers a charge cloud radius of $r_{cs} = 10\,\mu$m ($r_{cs} = 20\,\mu$m). As charge sharing is only dependent on the ratio of boundary to pixel area, it is independent of the detector radius, as can be seen in equation 4.2.
In order to reach charge sharing probabilities of less than 4%, a pixel radius of > 1 mm is needed. With 1 mm pixel radius and 10^4 pixels the total detector radius would be 100 mm. If larger detector radii would be required, either the pixel number or the pixel radius would have to be increased. However, the pixel number is expected to be limited to about 10^4, since a sophisticated and space consuming read-out system is planned for each pixel [Dol16]. The pixel radius is expected to be limited to about < 2 mm to minimize the detector capacity and hence the noise level.
Consequently, the pixel size should be in the regime of millimeters $r_{px} = 1$–2 mm and the detector radius r_{det} should be between 100 mm and 200 mm.
By vetoing coincident signals of neighboring pixels, charge sharing can be vetoed. However charge sharing events with energies below the energy threshold would be missed. As a consequence, the amount of charge sharing should be minimized and a system with possibly low energy threshold needs to be developed.

4.1.2. Optimization with respect to pile up

The time resolution of a detector is mostly determined by the read-out electronics. In general the digitizer output consists of a signal and fluctuating electronic noise. To evaluate

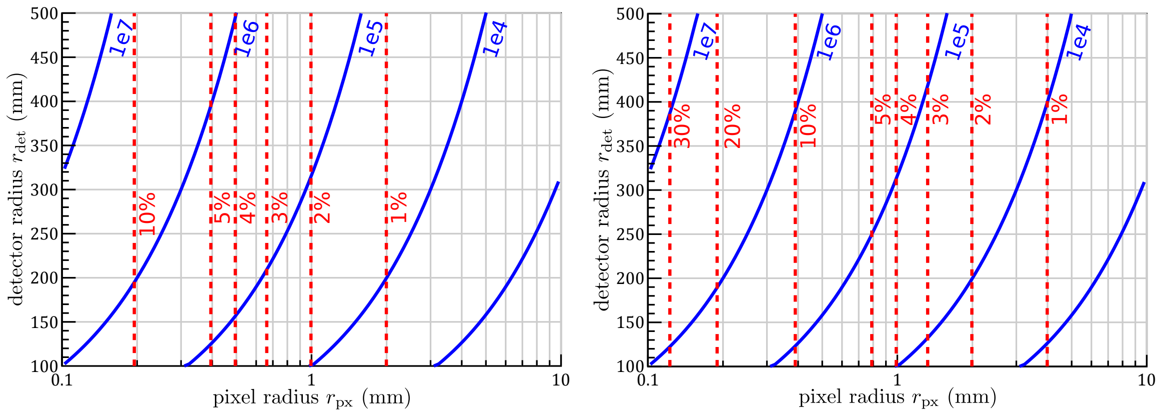

(a) $r_{cs} = 10\,\mu$m (b) $r_{cs} = 20\,\mu$m

Figure 4.2.: In red the percentage of charge sharing events according to equation 4.2 is given. The isolines of constant pixel numbers N_{px} are marked in blue. The charge sharing model is based on a charge cloud radius of $r_{cs} = 10\,\mu$m (a) ($r_{cs} = 20\,\mu$m (b)).

the signal energy, typically a filter is applied.
An exemplary filter is the trapezoidal filter. It basically averages the digitizer output before and after the signal rise and deducts the two values to obtain the signal energy. The averages are calculated within the raise time t_r and are separated by the flat top time t_{ft}. The time resolution is hence given by the total time, called the shaping time t_s.

$$t_s = t_r + t_{ft} + t_r \tag{4.3}$$

If two events occur within the shaping time t_s, the two events cannot be fully resolved and the energy measured E_{ms} would correspond to a sum of both events.

$$E_{ms} = E_1 + \xi \cdot E_2 \tag{4.4}$$

E_1 denotes the energy of the first event, while the energy of the second event E_2 is accounted only partially, $\xi \in [0, 1]$. The factor ξ is only equal to one, if the maximum of the second signal is reached within t_s.
The rate per pixel Γ_{px} is limited by pile up, since a higher rate would imply that the number of events identified as single events, though consisting of multiple events, increases.

Pile-up model

The pile-up model consists of the throughput $f_{th}(r)$ and an efficiency factor ϵ. The throughput is similar to the probability density function (pdf) of the exponential distribution $f(t)$, but parametrized in r. The exponential pdf

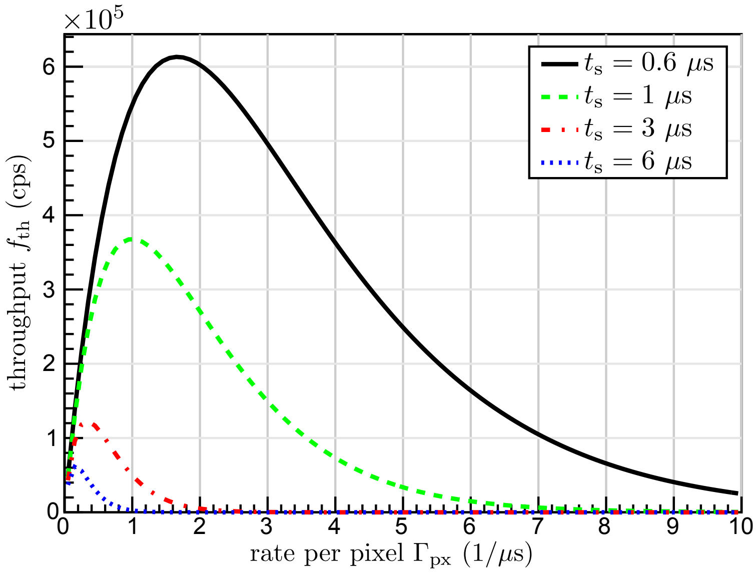

Figure 4.3: Illustration of the throughput for different shaping times t_s. Small shaping times allow higher rates per pixel, before being affected by pile-up.

$$f(t) = \begin{cases} r \cdot e^{-r \cdot t} & t \geq 0 \\ 0 & t < 0 \end{cases}, \tag{4.5}$$

describes the time between two events in a Poisson process, with time t and rate r, and the throughput

$$f_{\mathrm{th}}(r) = r \cdot e^{-r \cdot t} \tag{4.6}$$

describes the rate of non pile-up events (see figure 4.3). For low rates the throughput increases with r, however, for very large r almost every event is piled up with another event and the throughput decreases. The maximum throughput that can be reached depends on the applied shaping time, see figure 4.3.

We are interested in the probability of pile-up events within the time resolution of the detector, the shaping time t_s. Typical values for the shaping time are in the order of μs (section 4.4.1). For the model two different values were tested: $t_s = 0.6\,\mu$s and $t_s = 6\,\mu$s. Thus the pile-up probability, with respect to the pixel rate $\Gamma_{\mathrm{px}} \equiv r$, is given by:

$$P_{\mathrm{pu}} = (1 - \epsilon) \cdot \int_0^{t_s} \Gamma_{\mathrm{px}} \cdot e^{-\Gamma_{\mathrm{px}} \cdot t} \mathrm{d}t \tag{4.7}$$

The efficiency ϵ considers low level pile-up rejection mechanisms, i.e. filters which can resolve two events even though $\Delta t < t_s$. We assume an efficiency of $\epsilon = 90\%$.

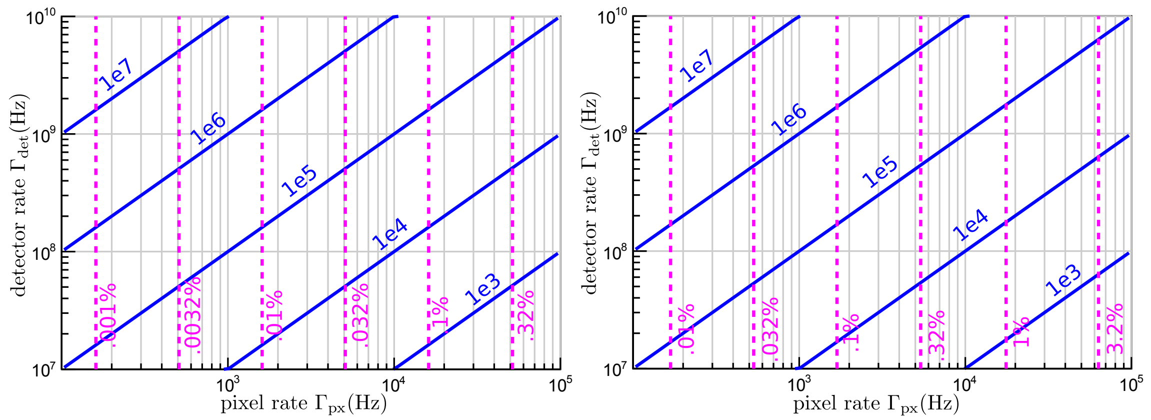

(a) $t_s = 0.6\,\mu$s (b) $t_s = 6\,\mu$s

Figure 4.4.: Optimization results with regards to pile-up in the detector rate Γ_{det} and pixel rate Γ_{px} plane. The percentage of irreducible pile-up ($\epsilon = 0.9$) is marked in pink. The plot assumes a pile-up model according to equation 4.7, and a shaping time $t_s = 0.6\,\mu$s (a) ($t_s = 6\,\mu$s (b)).

Results

Figure 4.6 shows the fraction of irreducible pile-up in the detector rate and pixel rate plane. As shown in equation 4.7, the pile-up probability only depends on the individual pixel rate. Limiting the missed pile-up fraction to less than 1% (see figure 4.4b) constrains the rate per pixel to about $2 \cdot 10^4$ cps. Assuming a maximum number of 10^4 pixels, the the total rate at the detector is limited to $\approx 2 \cdot 10^8$ cps. This is a factor of 50 less, than what can be achieved with the full KATRIN source strength.
Increasing the number of pixels would reduce the rate per pixel and hence decrease the pile-up probability, but for a fixed detector radius, this would in turn increase the effect of charge sharing, see previous section 4.1.1.

4.1.3. Optimization with respect to backscattering

Due to inelastic scattering processes, the incident particle has a non zero probability to scatter in a way that it or a secondary electron leaves the detector. In this case only a part of total energy is deposited in the detector, while the rest remains undetected for this particular event [Ren11].
With the magnetic and electric fields available at KATRIN, it is possible to ensure, that most of the backscattered electrons are directed back to the detector. In pixel *ww* in figure 4.1 three backscattered events are depicted. Redirecting the electrons back to the detector surface, in general, results in a position shift compared to the initial position (see figure 4.15).
Tracking simulations with KASSIOPEIA, described in more detail in section 4.2, show that the position shift is in the regime of a few millimeters $\Delta r_{\mathrm{el}} = \mathcal{O}(\mathrm{mm})$ and the flight time is in the range of sub micro seconds $\Delta t = \mathcal{O}(0.1\,\mu\mathrm{s})$. In the following, the Δr_{el} and Δt distributions obtained from tracking simulations from section 4.2.3 are used, to veto

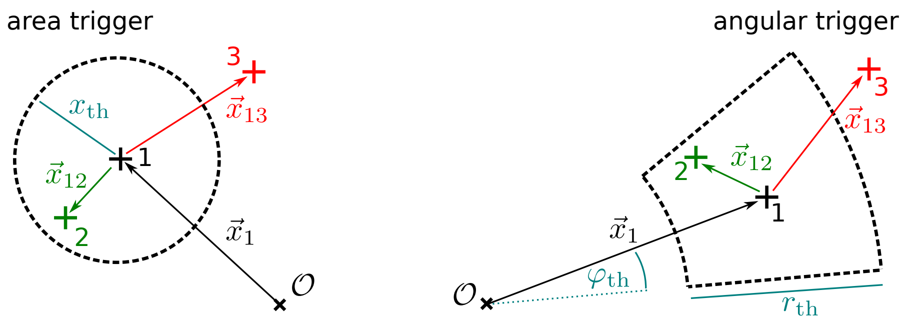

Figure 4.5.: Schema of two possible spatial triggers, which, together with a time trigger, will discard coinciding electron events. The crosses depict electron hits. An electron is successfully triggered (highlighted in green), if it hits within a trigger region constructed around the 1st electron. For the area trigger the region is constructed by x_{th}, whereas the region for the angular trigger is constructed by ϕ_{th} and r_{th}.

backscattered events, and discuss the impact of such vetoes to the total detector rate.

Veto backscattering

If the detector is placed in a magnetic field smaller than the maximal field in the system, backscattered electrons may be magnetically reflected and guided back to the detector, see section 4.2.3. Hence a single electron may hit the detector multiple times at different positions. A method to reduce the number of backscattered electrons is to apply a veto on all events, that arrive in a certain time window and within a certain distance to a previous event. This would simultaneously help to discard charge sharing events.
The veto mechanism would consist of two triggers, a lateral position trigger and a time trigger. Consequently, the events, coinciding in space and time would be discarded. Two different ideas for position triggers are considered (see figure 4.5):

- Area trigger:
  The Area Trigger monitors the absolute distance between events $|\Delta\vec{x}|$ and only triggers if the distance is below a certain threshold value x_{th}.
  The trigger region, i.e. the coincidence area around a particular event is given by:

$$A_{area} = r_{th}^2 \cdot \pi \tag{4.8}$$

- Angular trigger:
  The Angular Trigger monitors the angle $\Delta\varphi$ and the radial Δr differences of every event with respect to the detector center. It triggers, if both are below predefined threshold values φ_{th} and r_{th}.
  The trigger region depends on the actual detector size, since for a constant values of φ_{th} the trigger region A_{ang} is higher at higher radii r:

$$A_{ang} = \frac{2 \cdot \varphi_{th}}{360°} \cdot \left((\bar{r} + r_{th})^2 - (\bar{r} - r_{th})^2\right) \cdot \pi \qquad \bar{r} = 2/3 \cdot r_{det} \tag{4.9}$$

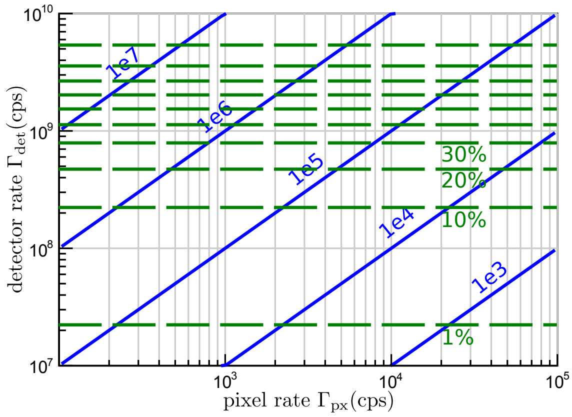

(a) area trigger

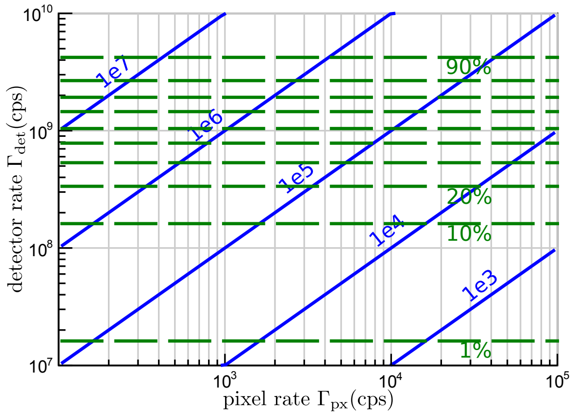

(b) angular trigger

Figure 4.6.: Optimization results with regards to backscattering in the detector rate Γ_{det} and pixel rate Γ_{px} plane. The effect of backscattering is reflected in a way, that by vetoing backscattered electrons, a certain percentage of events is falsely discarded (green). The area trigger is used in (a), whereas the angular trigger is used in (b). In blue are the isolines of constant number of pixels N_{px}.

Here $\bar{r}$ is the mean radius of electrons, that hit the detector surface homogeneously.

The angular trigger is motivated by the guiding center drift, a component of the total position change, of electrons (section 4.2.3). The guiding center drift predicts an electron displacement in direction of the azimuthal unit vetor $\vec{e}_\varphi$ (see figure 4.16). Thus triggering with respect to φ could allow a better discrimination of detector events.

Falsely discarded events

Using vetoes would also result in discarding events that are not subject to charge sharing, backscattering, etc. These events would be falsely discarded and would reduce the statistics.
To quantify the percentage of falsely discarded electrons, a Monte Carlo simulation was performed. The Monte Carlo model randomly generates electrons at the detector surface, according to a certain rate Γ_{det}. We assume that all of the generated electrons are real events, i.e. they do not produce charge clouds, do not backscatter, etc. Using the time and position information of each electron, a veto was applied to search for space and time coincidences. Coinciding events would be discarded and thus lead to events that are falsely discarded. The percentage of falsely discarded P_{fd} events is consequently given by:

$$P_{\text{fd}} = \frac{N_{\text{disc}}}{N_{\text{tot}}} \tag{4.10}$$

With the number of discarded electrons N_{disc} and the total number of simulated electrons N_{tot}.

Table 4.1.: Threshold values for vetoing backscattered electrons for the Post-KATRIN 5 B_{add} scenario. The threshold values are based on simulations in KASSIOPEIA from table 4.5.

quantiles q_{p} (%)	TIME TRIGGER t_{th} (ns)	AREA TRIGGER x_{th} (mm)	ANGULAR TRIGGER r_{th} (mm)	φ_{th} (°)
99.0	131	10.1	7.27	6.24
99.9	190	11.7	8.90	16.1

The threshold values for the time and space triggers were derived from electron tracking simulations in KASSIOPEIA (see section 4.2.3). The veto model threshold values are based on 99% quantiles, i.e. 99% of the backscattered electrons are smaller then the used threshold value (table 4.1). The simulation assumes a detector radius of $r_{\mathrm{det}} \approx 24\,\mathrm{cm}$ and situated in a magnetic field of $B_{\mathrm{det}} = 0.2\,\mathrm{T}$ (table 4.3), referred to as the Post-KATRIN 5 B_{add} scenario.

Results

In figure 4.6 the fraction of falsely vetoed events is shown in the plane of detector rate and pixel rate. As the backscattering veto does not consider the individual pixels, the result is independent on the pixel rate, but only depends on the overall rate. For 10^4 pixels in the Post-KATRIN 5 B_{add} scenario, the pixel radius would about 2 mm, this reduces the charge sharing to $< 1\%$ (see figure 4.4b).
To limit the amount of falsely vetoed events to 10% the total rate can not exceed $\approx 2 \cdot 10^8$ cps. At this rate, for 10^4 pixels the missed pile-up fraction would be $\approx 1.5\%$ (see figure 4.4b).
The angular trigger results in a higher number of falsely discarded events. The deteriorated percentage of falsely discarded events originates from the fact that the trigger region A_{ang} of the angular trigger depends on the radial position of the electron events. Table 4.2 compares the mean angular trigger region (equation 4.9) to the area trigger region (equation 4.8) for different experimental setups.

In summary, one possible configuration of a future detector, referred to as the Post-KATRIN 5 B_{add} scenario, would yield $< 1\%$ charge sharing, $\approx 1.5\%$ missed pile-up and 10% falsely vetoed events.

4.2. Simulation of electrons in the detector section

After the generic considerations in section 4.1, the next step is to simulate the impact on the above mentioned detector effects on the tritium β-decay spectrum. To this end we perform dedicated simulations with the software package KASSIOPEIA [Gro15]. The goal of these simulations is to …

Table 4.2.: 99% spatial trigger regions for the area and angular trigger, based on 99% trigger quantiles (table 4.5. The regions were calculated according to equation 4.9 and 4.8. The different simulation scenarios are introduced in section 4.2.2.

Sim. scenario	r_{det} (mm)	A_{area} (mm^2)	A_{ang} (mm^2)	$A_{\mathrm{ang}}/A_{\mathrm{area}}$
Pre-KATRIN	42	0.27	0.56	2.09
Post-KATRIN 1	47	0.34	0.78	2.27
Post-KATRIN 2	55	0.59	1.39	2.37
Post-KATRIN 3	67	1.34	3.08	2.30
Post-KATRIN 4	95	5.47	11.9	2.17
Post-KATRIN 5	240	231	553	2.39
Post-KATRIN 5 B_{add}	240	320	509	1.59

- …simulate the incident angle distribution of electrons at the detector; since the backscattering probability depends on the incident angle.
- …simulate the fraction of magnetically back reflected electrons; since backscattered electrons that are magnetically back-reflected allow for vetoing mechanisms, which are based on coincident events.
- …simulate the time it takes for an electron to return to the detector; in order to derive the time trigger threshold values.
- …simulate the distance on the detector between the first hit and the second hit of one backscattered and reflected electron; in order to derive the position threshold values.

All these properties are investigated as a function of the detector magnetic field and position. Here we can distinguish two cases: the nominal KATRIN setting and a future KATRIN experimental setup. We refer to a keV-scale sterile neutrino search with the nominal settings as Pre-KATRIN scenario. This scenario requires a reduced counting rate in order to allow the usage of the KATRIN Focal Plane Detector. The future TRISTAN setup, is referred to as Post-KATRIN scenario. Here the detector can be moved to a smaller magnetic field, the detector size can be increased and an additional magnetic coil can be installed. In particular we consider five different experimental setups for the Post-KATRIN scenario (table 4.3).

4.2.1. Pre- & Post-KATRIN detector setup

Pre-KATRIN detector setup

The Pre-KATRIN scenario aims at sensitivity limits on keV-scale sterile neutrino, by analyzing the whole β-decay spectrum of tritium for only a few days. The idea is to use the KATRIN facility with only minor modifications. Consequently the simulated detector setup stays unmodified and is illustrated in figure 4.7.

Table 4.3.: Parameters for the six different simulated experimental setups presented in this section. z denotes the position of the detector, r_{det} is the detector radius, B depicts the magnetic field at the detector position, and $\theta_{\mathrm{p,max}}$ is the maximal expected incident angle, calculated according to equation 4.15. $\theta_{\mathrm{B}}(r)$ accommodates the impact of a divergent magnetic field at the detector position, as illustrated in figure 4.9.

type	z (m)	r_{det} (cm)	B (T)	B/B_{Pre} (%)	$\theta_{\mathrm{p,max}}$ (°)
Pre-KATRIN	13.93	4.24	3.39	100	$49 + \theta_B(r)$
Post-KATRIN 1	14.06	4.74	2.71	80	$42 + \theta_B(r)$
Post-KATRIN 2	14.15	5.47	2.03	60	$36 + \theta_B(r)$
Post-KATRIN 3	14.24	6.70	1.35	40	$28 + \theta_B(r)$
Post-KATRIN 4	14.39	9.48	0.68	20	$20 + \theta_B(r)$
Post-KATRIN 5	14.90	24.10	0.10	3	$8 + \theta_B(r)$
Post-KATRIN 5 B_{add}	15.20	24.10	0.10	3	8

The scheme shows a slice through axial symmetric setup. It starts at the valve connecting to the Main Spectrometer and ends with the vacuum vessel holding the detector flange on the right. The pinch magnet $B_{\mathrm{p}} = 6\,\mathrm{T}$ and the detector magnet $B_{\mathrm{det}} \approx 3.4\,\mathrm{T}$ are depicted as green boxes and generate an almost homogeneous magnetic field within the vacuum steel vessels.

In normal operation mode the electrons are magnetically guided and enter the setup coming from the Main Spectrometer. After a short flight they reach the detector situated within the detector magnet. Due to inelastic scattering in the detector medium, there is a non-zero probability that electrons are backscattered $P_{\mathrm{BS}} > 30\%$ and only deposit part of the energy in the detector. Furthermore the backscattered electrons might escape P_{esc} into the Main Spectrometer and thus lead to missidentification of the deposited energy.

Post-KATRIN detector setup

In contrast to the Pre-KATRIN scenario, the Post-KATRIN measurements aims at high electron statistics and excellent energy resolutions. To measure the signature of a keV-scale sterile neutrino, a good knowledge of the measured spectral shape is necessary.
When designing the detector setup for keV-scale sterile the goal is to reduce the effect of backscattering (P_{BS}) and also to reduce the number of escaped electrons (P_{esc}).

- Probability of detector backscattering P_{BS}:
  The backscattering probability depends heavily on the incident angle θ_{I} of the electron and slightly on the electron energy, as shown in figure B.1. Consequently, to reduce backscattering, low incident angles $\theta_{\mathrm{I}} < 15°$ and high energies $E_{\mathrm{I}} > 10\,\mathrm{keV}$ are preferred.

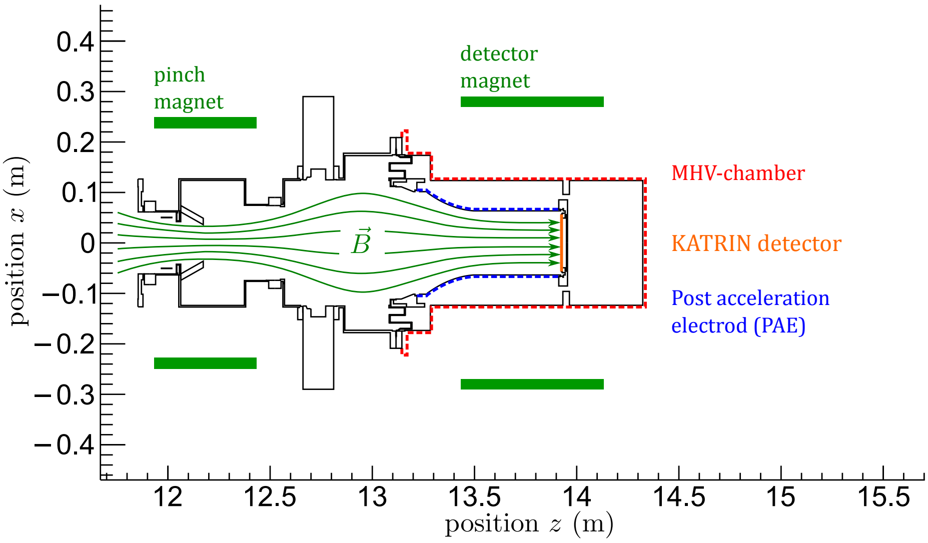

Figure 4.7.: Profile of the detector section of the KATRIN experiment. The Main Spectrometer is situated to the left of the figure. Electrons are generated within the pinch magnet coil (green bar), are guided along the magnetic field lines (green lines) and finally terminated at the detector surface (orange bar).

- Probability of electron escape P_{esc}:
  Electrons, that backscatter from the detector surface, leave the detector with a certain energy E_{BS} (see figure B.2) and under a certain angle θ_{BS} (see figure B.3). With the help of electric (section 4.2.4) and magnetic fields, these electrons can be guided back to the detector, thus reducing the amount of escaped electrons and allowing to veto backscattered events.

The maximum magnetic field of the KATRIN experiment is given at the pinch magnet $B_p = B_{max} = 6\,\mathrm{T}$. Electrons moving to the detector at B_{det} experience a decrease of the magnetic field, reducing the velocity component perpendicular to the magnetic field lines $v_\perp$ and thus also reducing the incident angle θ_I.

$$\sin(\theta_I) = \frac{v_{\perp,I}}{v} < \sqrt{\frac{B_{det}}{B_{max}}} \tag{4.11}$$

Thus lowering the magnetic field at the detector $B_{det} \searrow$ would result in a decrease of the incident angles $\theta_I \searrow$ and thus decrease detector backscattering P_{BS}. On the other hand a decrease of the detector magnetic field $B_{det} \searrow$ implies an increase of the detector radius r_{det}, which is due to the conservation of the magnetic flux:

$$\Phi = B \cdot A = 191\,\mathrm{Tcm}^2 \quad \longrightarrow \quad r_{det} = \sqrt{\frac{\Phi}{B \cdot \pi}} \tag{4.12}$$

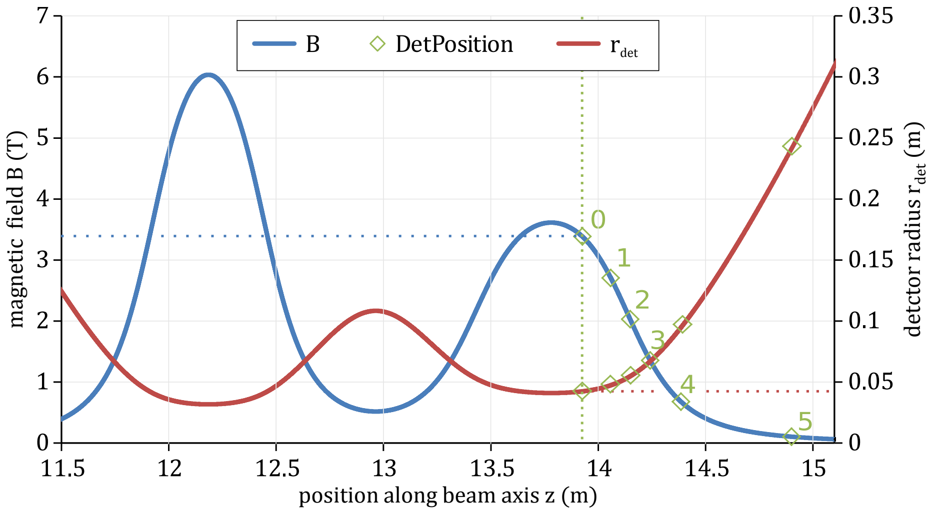

Figure 4.8.: Magnetic field B affecting a test charge along the beam axis z. Due to the conservation of magnetic flux $\Phi = 191\,\mathrm{Tcm}^2$, the electron flux radius r scales reciprocal to to the magnetic field B and determines the detector radius r_{det}. The different simulated detector sections setups are marked with numbers: 0 = Pre-KATRIN, 1 = Post-KATRIN 1, 2 = Post-KATRIN 2, etc.

In order to compensate the increased detector radius r_{det} but still use the same detector magnet, it is necessary to move the detector along the beam axis z. The farther away from the detector magnet $z \nearrow$ the lower the magnetic field $B \searrow$ at the detector. In total 5 different Post-KATRIN scenarios were simulated. The different scenario parameters are presented in figure 4.8.

The highest detector radius used for simulation is $r_{\mathrm{det}} \approx 24\,\mathrm{cm}$ (Post-KATRIN 5), which corresponds to the upper limit derived from the constraint on the number of pixels $N < \mathcal{O}(10^4)$ and pixel size $r_{\mathrm{px}} < \mathcal{O}(\mathrm{mm})$ from figure 4.2 in section 4.1.
The modified experimental detector setup is illustrated in figure 4.9. Both the vacuum chamber (red lines) and the post acceleration electrode (blue lines) need to be extended to accommodate the increased detector size.

4.2.2. Forward electron tracking

The forward tracking simulation yields the incident angle distribution of electrons at the detector. With the help of this distribution the probability of backscattering is calculated. In the simulation electrons were generated at the highest magnetic field within the pinch magnet $z \approx 12.18$. The electrons are created homogeneously, within a circular disc with radius $r \overset{4.12}{\approx} 3.2\,\mathrm{cm}$, and isotropic, thus flying in direction of the detector.

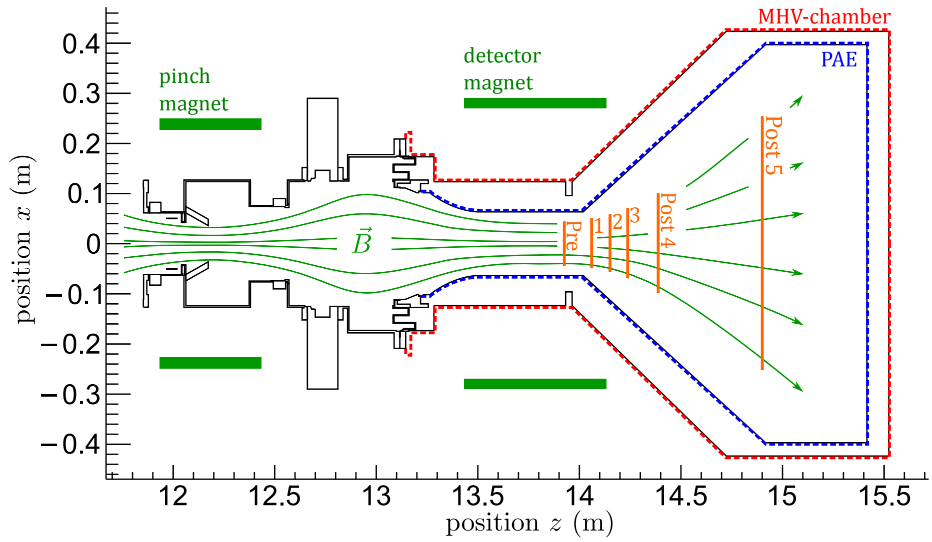

Figure 4.9.: Schema of the simulated detector section setup. The schema includes a modified vacuum chamber (red) and post acceleration electrode (blue). According to the scenarios listed in table 4.3, the detector size r_{det} and position z_{det} are adjusted. The electrons are guided along the magnetic field lines marked in green.

$$\begin{aligned} r_{\text{in}} &\in [0\,\text{cm}, 3.2\,\text{cm})\ \text{homogeneous} & E_{\text{kin,in}} &\in [0.5\,\text{keV}, 20\,\text{keV})\ \text{uniform} \\ \varphi_{\text{in}} &\in [-180^\circ, 180^\circ)\ \text{homogeneous} & \varphi_{\text{p,in}} &\in [-180^\circ, 180^\circ)\ \text{isotropic} \\ z_{\text{in}} &= 12.18\,\text{m} & \theta_{\text{p,in}} &\in [0, 90^\circ)\ \text{isotropic} \end{aligned} \tag{4.13}$$

Upon reaching the detector surface, the electron tracking is stopped and the position and momentum vector recorded.

$$\begin{aligned} r_{\text{fi}} &\in [0\,\text{cm}, r_{\text{det}})\ \text{homogeneous} & E_{\text{kin,fi}} &\in [0.5\,\text{keV}, 20\,\text{keV})\ \text{uniform} \\ \varphi_{\text{fi}} &\in [-180^\circ, 180^\circ)\ \text{homogeneous} & \varphi_{\text{p,fi}} &\in [-180^\circ, 180^\circ)\ \text{isotropic} \\ z_{\text{fi}} &= z_{\text{det}} & \theta_{\text{p,fi}} &\in \text{figure 4.10} \end{aligned} \tag{4.14}$$

The radius r_{det} and position z_{det} corresponds to the underlying simulated detector sections, i.e. the 1x Pre- and 5x Post-KATRIN simulations highlighted in figure 4.8.

Comparing detector positions

Both table 4.3 and figure 4.10 show, that placing the detector further away from the magnet, i.e. in a smaller magnetic field, reduces the incident angle of the electrons.

The bigger the distance to the detector magnet, the smaller the magnetic field, which in principle is expected to reduce the incident angle and thus reduce the backscattering

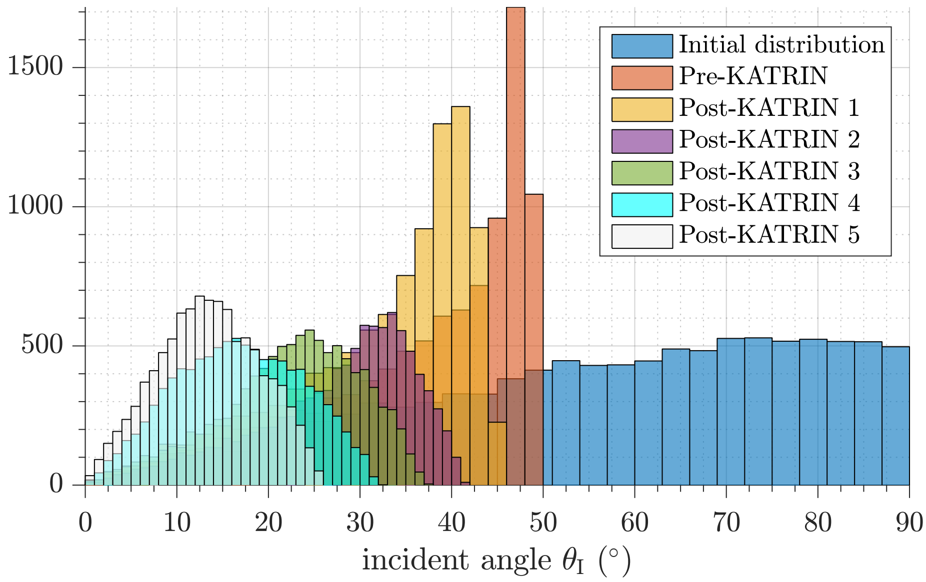

Figure 4.10.: Comparing the initial distribution of the polar angle $\theta_{\mathrm{p,in}}$ to the final distribution of $\theta_{\mathrm{p,fi}}$, for different detector positions as introduced in figure 4.8. In general, the scenarios, in which the detector is placed in a lower magnetic field, result in smaller incident angles $\theta_\mathrm{I} = \theta_{\mathrm{p,fi}}$.

probability. However, as can be seen in figure 4.9, the outer field lines do not hit the detector perpendicularly. Consequently, even though the electrons fly parallel to the magnetic field line, they do not hit the detector perpendicularly. Two solutions are possible: either the detector is constructed in a spherical way, or an additional magnet is used behind the detector, in order to bend the magnetic field lines, such, that they hit the detector perpendicularly. If the angle of the magnetic field line to the detector surface normal is given by θ_B, then the corresponding maximum incident angle is:

$$\theta_{\mathrm{I,max}} = \arcsin\left(\sqrt{\frac{B}{B_{\mathrm{max}}}}\right) + \theta_\mathrm{B}(r) \tag{4.15}$$

Note that the angle θ_B is depending on the position on the detector surface. For outer radii θ_B increases.

Additional detector magnet

A possibility to compensate this effect, is by adding another magnet, which bends the magnetic field lines to be perpendicular to the detector surface. In the simulation presented here, this has been included for the Post-KATRIN 5 case.

Figure 4.11a compares the incident angle $\theta_{\mathrm{p,fi}}$ as a function of r for the two cases. It can be clearly seen that the additional coil removes the radial dependence of the incident

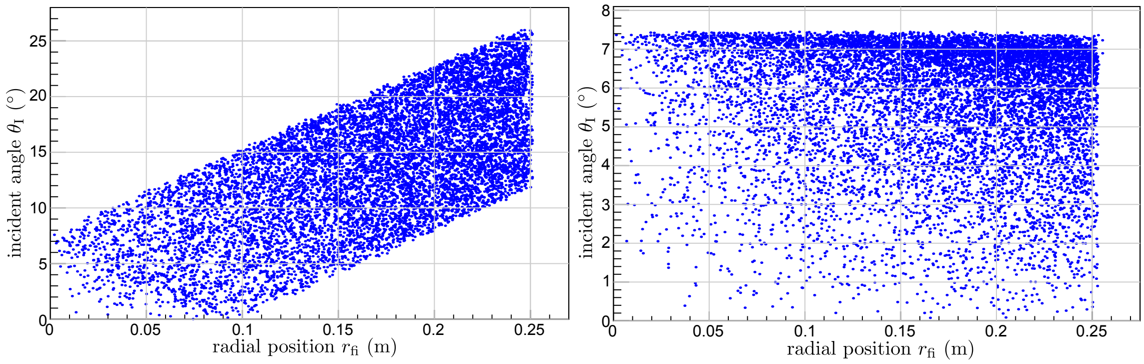

(a) Post-KATRIN 5

(b) Post-KATRIN 5 B_{add}

Figure 4.11.: Scatter plot of the final radial position r_{fi} and final momentum angle θ_{p}. The simulation spans 10^4 electron events, and is based on the Post-KATRIN 5 (a), respectively Post-KATRIN 5 B_{add} (b) setup. The additional magnet, which enforces perpendicular magnet field lines at the detector surface, breaks the correlation between r_{fi} and θ_{p}.

angle.
For further comparison, the distributions of θ_{p} for the Post-KATRIN 5 with and without the additional detector magnet are presented in figure 4.12. The resulting simulated maximal incident angle (yellow histogram) has no radial dependence $\theta_{\mathrm{B}} = 0$ (table 4.3).

4.2.3. Backscattered electron tracking

The goal of this simulation is to track backscattered electrons. In particular, we are interested in the flight time of magnetically reflected electrons and their final position, where the detector is hit for the second time. Here we are only interested in the time and position change corresponding to single backscattering process. The effect of multiple scattering will be implemented in the next section. The knowledge of the expected position change and the backscattered electrons flight time allows to veto backscattered electrons and thus reduce their impact to the keV-scale sterile neutrino search.
In the backscattering simulation electrons are homogeneously generated at the detector surface $z_{\mathrm{in}} = z_{\mathrm{det}}$ with a momentum pointing in direction of the Main Spectrometer.

$$
\begin{aligned}
t_{\mathrm{in}} &= 0\,\mathrm{s} & & \\
r_{\mathrm{in}} &\in [0\,\mathrm{cm}, r_{\mathrm{det}})\ \text{homogeneous} & E_{\mathrm{kin,in}} &\in [0.2\,\mathrm{keV}, 20\,\mathrm{keV})\ \text{uniform} \\
\varphi_{\mathrm{in}} &\in [-180^\circ, 180^\circ)\ \text{homogeneous} & \varphi_{\mathrm{p,in}} &\in [-180^\circ, 180^\circ)\ \text{isotropic} \\
z_{\mathrm{in}} &= z_{\mathrm{det}} & \theta_{\mathrm{p,in}} &\in [90^\circ, 180^\circ)\ \text{isotropic}
\end{aligned}
\tag{4.16}
$$

The generated electrons are then guided along the magnetic field lines. While some of the electrons may escape further detection and fly into the Main Spectrometer, other electrons return after a short flight time Δt back to the detector surface, and are thus detected. Ta-

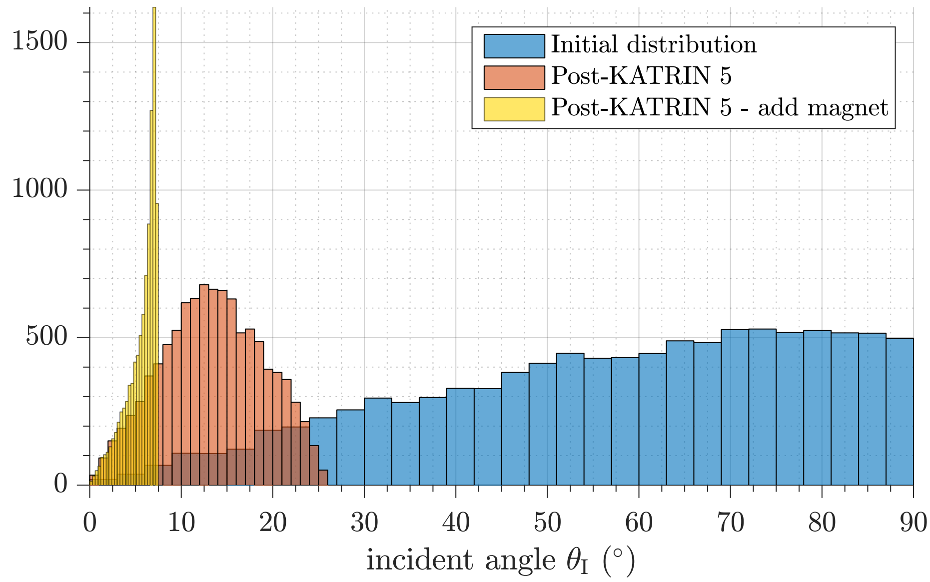

Figure 4.12.: Distribution of the polar angle θ_p. The initial distribution is marked in blue, the final distribution of $\theta_\mathrm{p} = \theta_\mathrm{I}$ for the Post-KATRIN 5 scenario is marked in red, whereas the same setup with an additional detector magnet is marked in yellow. The additional magnet enforces perpendicular magnetic field lines on the detector surface and thus greatly diminishes the radial influence of $\theta_\mathrm{B}(r) \approx 0$ (equation 4.15)

ble 4.4 shows the probability of back-reflected electrons for the different detector scenarios.

The tracking of an electron is terminated, if the simulated electron hits the detector or escapes into the Main Spectrometer $z < 11\,\mathrm{m}$. The escaped electrons are not measured by the detector, hence only the final distributions of the reflected electrons are of importance.

$$
\begin{aligned}
t^\mathrm{r}_\mathrm{fi} &= \Delta t & & \\
r^\mathrm{r}_\mathrm{fi} &\in [0\,\mathrm{cm}, r_\mathrm{det})\ \text{homogeneous} & E^\mathrm{r}_\mathrm{kin,fi} &\in [0.2\,\mathrm{keV}, 20\,\mathrm{keV})\ \text{uniform} \\
\varphi^\mathrm{r}_\mathrm{fi} &\in [-180^\circ, 180^\circ)\ \text{homogeneous} & \varphi^\mathrm{r}_\mathrm{p,fi} &\in [-180^\circ, 180^\circ)\ \text{isotropic} \\
z^\mathrm{r}_\mathrm{fi} &= z_\mathrm{det} & \theta^\mathrm{r}_\mathrm{p,fi} &\in [\theta^\mathrm{r}_\mathrm{p}, 90^\circ)
\end{aligned}
\tag{4.17}
$$

Here Δt denotes the flight time of reflected electrons. The flight depends mostly on the polar angle $\theta_\mathrm{p,in}$ and the electron energy E_in, as illustrated in figure 4.14a and described below.

Fraction of reflected electrons

The electrons that return to the detector are either magnetically guided back, or magnetically reflected.

Table 4.4.: Probability P_r, that backscattered electrons are reflected back to the detector. A lower magnetic field at the detector position, see table 4.3, implies a higher probability of back reflection.

type	P_r (%)
Pre-KATRIN	66
Post-KATRIN 1	74
Post-KATRIN 2	81
Post-KATRIN 3	88
Post-KATRIN 4	94
Post-KATRIN 5	99
Post-KATRIN 5 B_{add}	99

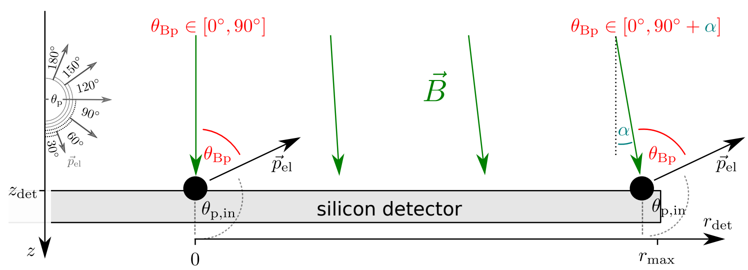

Figure 4.13: A slight magnetic field divergence near the detector edges can magnetically guide a small portion of backscattered electrons ($\theta > 90°$) back to the detector.

- Magnetic back guidance:
  Electrons are guided along the magnetic field lines. For diverging magnetic field at the detector surface, a small amount of electron are generated with an angle $\theta_{\mathrm{Bp}} \in (90°, 90° + \alpha]$, as illustrated in figure 4.13. These electrons will not be guided in direction of the Main Spectrometer, but directly guided back to the detector.

- Magnetic reflection:
  As discussed for equation 4.11, electrons moving in direction of a decreasing magnetic field, are magnetically focused, i.e. the velocity component perpendicular $\vec{v}_\perp$ to the magnetic field lines decreases, $\vec{v}_\perp \searrow$. For electrons moving in direction of an increasing magnetic field, the situation reverses $\vec{v}_\perp \nearrow$. If the polar angle drops below 90°, the electron is reflected. The reflection angle is

$$\theta_{\mathrm{p}}^{\mathrm{r}} = \arcsin\left(\sqrt{\frac{B_{\mathrm{in}}}{B_{\mathrm{max}}}}\right), \tag{4.18}$$

  B_{in} denotes the magnetic field strength at the detector position. Consequently, electrons with polar angle $\theta_{\mathrm{p,in}} \in (90°, 180° - \theta_{\mathrm{p}}^{\mathrm{r}})$ are magnetically reflected.

The fraction of reflected electrons P_r is hence given by the ratio of the number of electrons with a polar angle bigger than $180° - \theta_{\mathrm{p}}^{\mathrm{r}}$ and the total number of simulated electrons. In table 4.3 the fraction of reflected electrons P_r for the different detector

scenarios are noted. The values originate from the Monte Carlo simulation presented in this section.
In conclusion, the Post-KATRIN 5 B_{add} is the preferred Post-KATRIN scenario, as it yields the highest fraction of reflected electrons, namely $P_r = 99\%$ (table 4.4). A detector placed in lower magnetic fields $< 0.1\,T$, would yield higher reflection possibilities, but is technically not feasible (section 4.1.1).

Flight time of reflected electrons

The flight time strongly depends on the initial polar angle of the momentum $\theta_{p,in}$. Depending on this angle, the electron either escapes into the spectrometer, is reflected at the pinch magnet $B_{p,max} = 6\,T$, is reflected at the detector magnet $B_{d,max} = 3.6\,T$ or directly guided back to the detector surface.
In figure 4.14a each simulated event, which is reflected, is illustrated in a scatter plot of flight time versus initial polar angle. The underlying detector setup is the Pre-KATRIN scenario. The detector is situated at a magnetic field of $B_{in} \approx 3.4\,T$. Consequently, for $\theta_{p,in} \in (90°, 105°]$ the electrons are reflected at the detector magnet and for $\theta_{p,in} \in (105°, 132°]$ the electrons are reflected at the pinch magnet. The flight time spread originates from the different electron energies. The electrons escape into the Main Spectrometer for polar angles above 132°.

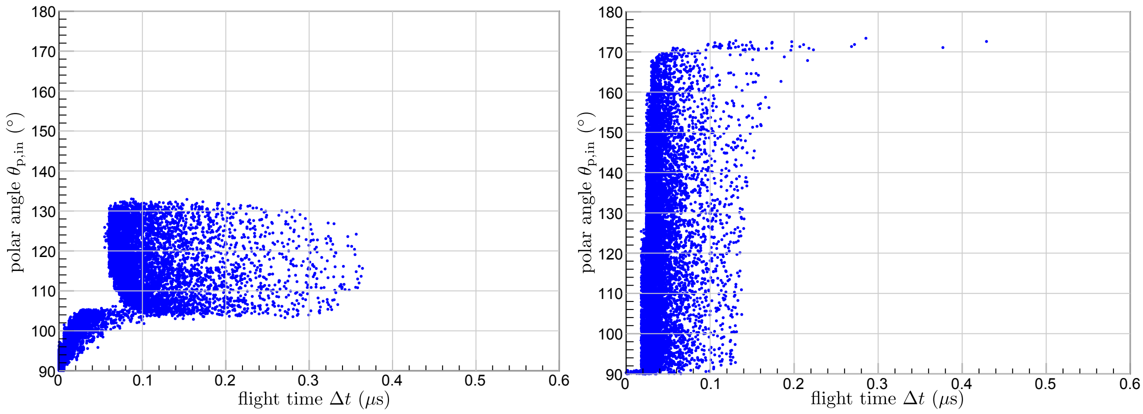

(a) Pre-KATRIN

(b) Post-KATRIN 5 B_{add}

Figure 4.14.: Scatter plot of initial polar angle vs flight time in the Pre-KATRIN (a) and Post-KATRIN 5 B_{add} (b) scenario. The figure shows all of the reflected electron events. The electrons are either reflected at the detector magnet (a: $\theta_{p,in} < 105°$); b: $\theta_{p,in} < 170°$)) or reflected at the pinch magnet.

For vetoing backscattered events, it is necessary, to trigger on all electrons within a certain time frame and spatial distance. For the time trigger, we are consequently interested in time it needs until 99% of the backscattered electrons return to the detector. This time is called the 99% flight time quantile $\Delta t_{99\%}$ and listed in table 4.5.
As discussed in section 4.1.3, when vetoing backscattered electrons, also non-backscattered electrons might be vetoed, which reduces the total statistics. The fraction of falsely dis-

Table 4.5.: Time and position quantiles for the different detector scenarios, derived from simulating 50, 000 electrons. Δt is used for the time trigger. The spatial triggers (section 4.1.3) are the area trigger, which depends on the distance $|\Delta\vec{x}|$ between two events, and the angular trigger, which depends on the radial $|\Delta r|$ and angular $|\Delta\varphi|$ distance between events.

type	Δt (μs)		$\|\Delta\vec{x}\|$ (mm)		$\|\Delta r\|$ (mm)		$\|\Delta\varphi\|$ (°)	
	99%	99.9%	99%	99.9%	99%	99.9%	99%	99.9%
Pre-KATRIN	0.311	0.407	0.291	0.336	0.220	0.260	1.28	3.65
Post-KATRIN 1	0.294	0.403	0.331	0.353	0.269	0.322	1.32	2.81
Post-KATRIN 2	0.275	0.420	0.433	0.462	0.353	0.429	1.55	4.27
Post-KATRIN 3	0.219	0.391	0.653	0.696	0.519	0.629	1.90	5.48
Post-KATRIN 4	0.157	0.323	1.32	1.42	1.03	1.28	2.62	7.83
Post-KATRIN 5	0.0899	0.205	8.59	9.36	6.66	8.19	7.40	15.6
Post-KATRIN 5 B_{add}	0.131	0.190	10.1	11.7	7.27	8.90	6.24	16.1

carded events depends on the time quantile. Hence small 99% time quantile are preferred. Investigating the Post-KATRIN scenarios, the smallest 99% time quantile is found for the Post-KATRIN 5 (B_{add}) case.

Position of reflected electrons

This section focuses on the initial and final position of electrons, that are start at the detector, are magnetically reflected, and, at the end, hit the detector. The knowledge of the relation between the initial and the final position on the detector is needed, in order to veto backscattered electrons.
The distance between the final and the initial position

$$\Delta x = |\vec{x}_{\mathrm{fi}} - \vec{x}_{\mathrm{in}}| = |\Delta\vec{x}_{\mathrm{gm}} + \Delta\vec{x}_{\mathrm{gc}}| \tag{4.19}$$

is divided into a gyromotion component $\Delta\vec{x}_{\mathrm{gm}}$ and guiding center drift component $\Delta\vec{x}_{\mathrm{gc}}$. In figure 4.15 the two component are illustrated.

- Gyromotion:
  An electron in a uniform magnetic field $\vec{B}$ is affected by the Lorentz force

  $$\vec{F} = e \cdot \vec{v} \times \vec{B} \tag{4.20}$$

  and will spiral along the magnetic field lines. Here e denotes the elementary electron charge and $\vec{v}$ is the electrons velocity. The spiral movement is referred to as gyromotion, and the center around which the electron spirals, is called guiding

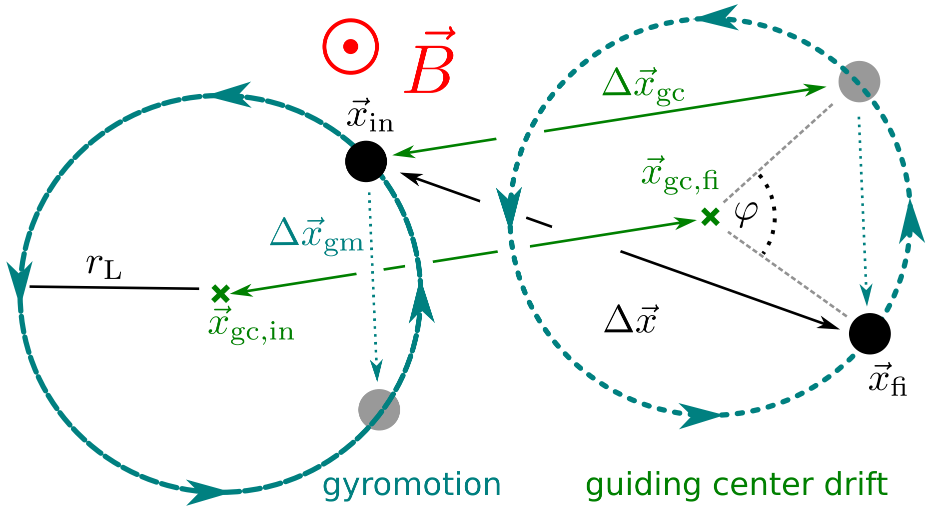

Figure 4.15.: Illustration of initial and final positions (black circles) for a reflected electron affected by gyromotion (cyan) and the guiding center drift (green). Depending on the phase $\phi \in (0°, 360°]$, the effect of gyromotion ranges between zero and two times the Larmor radius r_{L}.

center. The radius of the gyromotion is derived from the equality of Lorentz force and centripetal force, and called the Larmor radius

$$r_{\mathrm{L}} = \frac{m \cdot v_{\perp}}{q \cdot B}, \tag{4.21}$$

where m denotes the mass of the electron, and $v_{\perp}$ indicates the velocity component perpendicular to the magnetic field.

For an electron with 20 keV energy in a magnetic field of 3.4 T (0.1 T), the Larmor radius is about 0.13 mm (4.3 mm). The maximal position change, due to gyromotion, is $|\Delta\vec{x}| = 2 \cdot r_{\mathrm{L}}$ and $\varphi = 180°$.

Using equation 4.12 and 4.1, we can relate the magnetic field to the pixel radius, and thus investigate the ratio of Larmor radius over pixel radius

$$\frac{r_{\mathrm{L}}}{r_{\mathrm{px}}} = \frac{m \cdot v_{\perp}}{q} \cdot \frac{\pi\sqrt{N_{\mathrm{px}}}}{\Phi} \cdot r_{\mathrm{det}}. \tag{4.22}$$

Assuming a constant number of pixels $N_{\mathrm{px}} = 10^4$ for the different KATRIN detector scenarios, and an electron energy of 20 keV, then a backscattered electron, that is magnetically reflected, hits the Pre-KATRIN (Post-KATRIN 5 B_{add}) detector at maximal distance of $|\Delta\vec{x}|/r_{\mathrm{px}} = 2 \cdot r_{\mathrm{L}}/r_{\mathrm{px}} = 0.66$ (3.8) pixels away from the initial position. Consequently, in order to minimize the influence of gyromotion, small detector radii are preferred (equation 4.22).

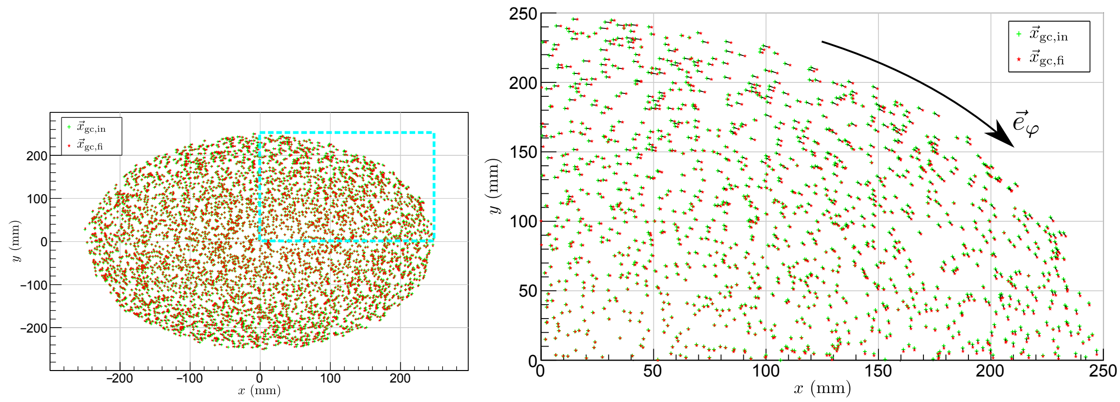

Figure 4.16.: Depiction of the initial and final guiding center position for the Post-KATRIN 5 B_{add} scenario. On the left the whole detector is depicted, whereas the right shows a zoom of the cyan bounded area. It is visible by eye, that drift points in direction of the azimuthal unit vector, emphasized by the black arrow.

- Guiding center drift:
  Regarding solely the magnetic setup, the drift of the guiding center is created from a non-uniform magnetic field. Moreover the drift is further divided into the grad-B drift and the curvature drift. The total shift of the guiding center

$$\Delta\vec{x}_{\mathrm{gc}} = \Delta t \cdot (\vec{v}_{\nabla\mathrm{B}} + \vec{v}_{\mathrm{cur}}) \tag{4.23}$$

  is given as the sum over the grad-B drift and the curvature drift, multiplied with the total flight time. The direction of the guiding center drift for the Post-KATRIN 5 B_{add} case is illustrated in figure 4.16. Because of the axial symmetry, of the KATRIN experiment, the drift points in direction of the azimuthal angle unit vector $\vec{e}_\varphi$.

  - Grad-B drift:
    An electron, moving parallel to magnetic field lines with varying magnetic field strengths, will drift with the velocity

$$\vec{v}_{\nabla\mathrm{B}} = \frac{E_{\mathrm{kin},\perp}}{e \cdot B} \cdot \frac{\vec{B} \times \vec{\nabla} B}{B^2} \tag{4.24}$$

    in direction perpendicular to the magnetic field and to the magnetic field gradient. Because of the axial symmetry the gradient points in azimuthal direction. $E_{\mathrm{kin},\perp}$ denotes the kinetic energy component perpendicular to the magnetic field and e depicts the elementary charge.

– Curvature drift:
  For electrons that follow a curved magnetic field line, the centripetal force requires an additional velocity

$$\vec{v}_{\text{cur}} = \frac{2E_{\text{kin},\parallel}}{eB} \cdot \frac{\vec{r}_{\text{cur}} \times \vec{B}}{r_{\text{cur}}^2 B}, \tag{4.25}$$

  with $\vec{r}_{\text{cur}}$ denotes the outwards pointing radius of curvature. Because of the axial symmetry, the velocity vector points in direction of the azimuthal angle unit vector $\vec{e}_\varphi$.

In figure 4.17 the positional change and the guiding center shift is depicted. The first thing to notice, is that the total change in position between detector hits is about a factor of 3 larger than the guiding center shift. This means that the position change of electrons is dominated by gyromotion.
The guiding center shift is divided in two parts, which originates from the different flight times of the electrons (see equation 4.23). Electrons below an initial polar angle of 105° — highlighted in red in in figure4.17 — are reflected at the detector magnet, whereas the rest is reflected at the pinch magnet and thus travel a longer distance, ergo have longer flight times (see figure 4.14a). The populations with small initial polar angle are depicted in red . The events highlighted in green, illustrate the energy dependence: the Lamor radius is directly proportional to the energy square root (in non relativistic approximation; equation 4.21). Consequently, increasing the energy by a factor of 4 (5 keV($green$) $\longrightarrow$ 20 keV (blue)) shifts the position change by a factor of 2.

Figure 4.18 similarly shows the positional change and the guiding center shift, but for the Post-KATRIN 5 B_{add} scenario. The gyromotion still dominates the position distance between two detector hits, and is in the regime of several millimeters. All the other scenarios are summarized by listing the 99% and 99.9% position quantiles in table 4.5.

4.2.4. The post acceleration electrode

Homogeneously increasing the kinetic energy of all electrons can mitigate both, the effect of backscattering and the energy loss in the dead-layer.
The electric field is generated by an axial symmetric electrode, operated with an elevated voltage U_{PAE}. The electrode is referred to as Post Acceleration Electrode and blue highlighted in figure 4.9.

Post acceleration and the dead layer

The post acceleration electrode, adds a constant energy to every electron flying from the Main Spectrometer to the detector (section 4.2.2). The final kinetic energy shifts is then given by

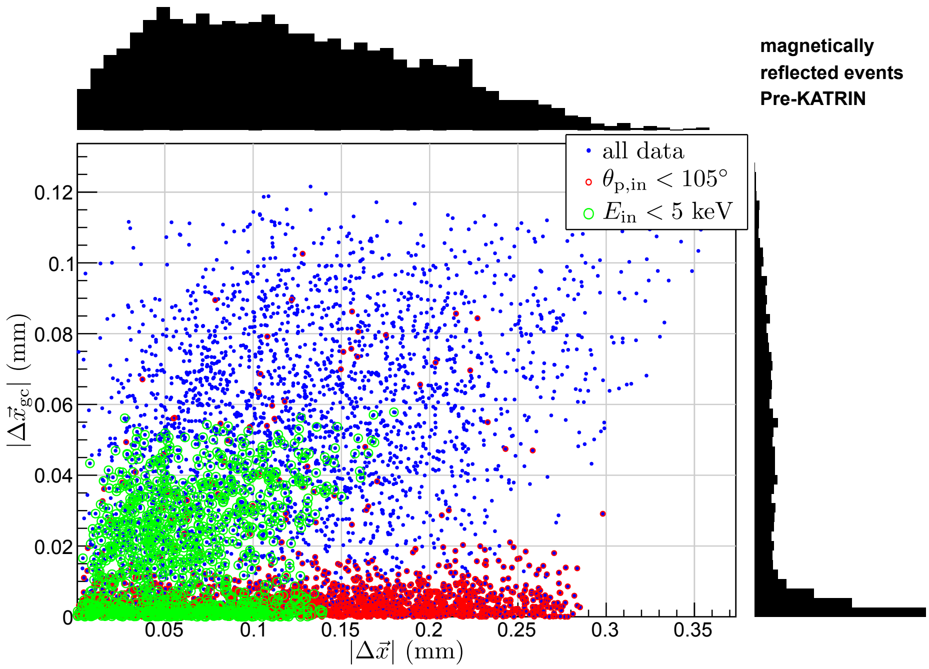

Figure 4.17.: Illustration of the total distance and guiding center shift between the initial and final electron for the Pre-KATRIN scenario. The blue dots depict all reflected electrons, whereas the circles in red (in green) painted around the blue dots, highlight electron events with an initial polar angle $< 105°$ (initial energy $< 5\,\mathrm{keV}$). We see, that the position change is strongly correlated to the initial polar angle and the energy of the backscattered electrons.

$$E_{\mathrm{kin,fi}} = E_{\mathrm{kin,in}} + e \cdot U_{\mathrm{PAE}}, \tag{4.26}$$

with the initial kinetic energy $E_{\mathrm{kin,in}}$. Assuming that every electron loses about 1 keV in the detector dead layer, before arriving in the sensitive area, then, in the case of no post acceleration, all electrons with an energy below 1 keV will not be measured. By shifting the energy spectrum by 10 to 20 keV, the detector becomes sensitive to these electrons. Moreover, in the case of no post acceleration, an electron with 5 keV would only deposit 4 keV in the sensitive detector area, while with $U_{\mathrm{PAE}} = 10\,\mathrm{kV}$, the deposited energy is 14 keV. Since the deposited energy

$$E_{\mathrm{dep}} = N_{\mathrm{eh}} \cdot E_{\mathrm{eh}}, \tag{4.27}$$

where E_{eh} denotes the energy to create an electron-hole pair in the detector, is proportional to the number of generated electron-hole pairs, a higher energy deposited also corresponds to better statistics, a reduced uncertainty and thus better energy resolution.

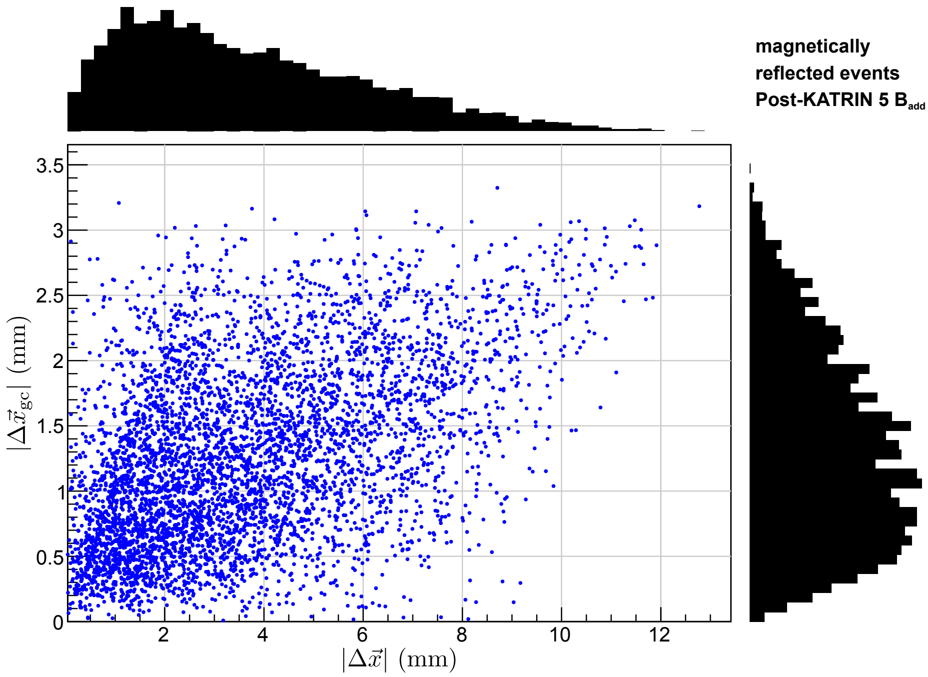

Figure 4.18.: Illustration of the total distance and guiding center shift between the initial and final electron. The blue dots depict the reflected electrons for a simulated Post-KATRIN 5 B_{add} scenario.

Post acceleration and backscattering

The post acceleration affects the backscattering in a 3-fold way: it reduces the probability of backscattering, it increases the probability of magnetic back-reflection, and it improves the discrimination of backscattered electrons from signal electrons.
The **probability of backscattering** is reduced, mainly due to the decrease of the final polar angle (see figure B.1):

$$\sin\theta'_{\mathrm{p,fi}} = \frac{\sqrt{E_{\mathrm{kin,in}}}}{\sqrt{E_{\mathrm{kin,in}} + e\cdot U_{\mathrm{PAE}}}} \cdot \sin\theta_{\mathrm{p,fi}} \tag{4.28}$$

Here $\theta_{\mathrm{p,fi}}$ denotes the final polar angle, as simulated in section 4.2.2. Equation 4.28 assumes a non-relativistic sum of the velocity vector, the post acceleration was added solely to the kinetic energy component, which is parallel to the magnetic field.
Table 4.6 lists impact of the post acceleration to the maximum polar angle, while disregarding the magnetic field divergence. Moreover, the **fraction of reflected electrons** is depicted for the Pre-KATRIN and Post-KATRIN B_{add} case. Backscattered electrons, with energies below the acceleration voltage, are electrically reflected, which leads to a small increase in the probability of reflected electrons. Additionally, the electric field decelerates the parallel velocity component of backscattered. In this way the polar angle is increased, which in turn allows for more electrons to be magnetically reflected.

Table 4.6.: Comparing the scenerios with post acceleration to the case without, as was listed in table 4.3. The maximal expected incident angle is calculated according to equation 4.28, assuming an energy of $(20 + 10_{\mathrm{pae}})$ keV and disregarding $\theta_B(r) = 0$. The percentage of reflected electrons, originates from simulating 500.000 electrons.

type	no post acceleration			$U_{\mathrm{PAE}} = 10\,\mathrm{kV}$	
	B/B_{Pre} (%)	$\theta_{\mathrm{p,max}}$ (°)	P_{r} (%)	$\theta'_{\mathrm{p,max}}$ (°)	P'_{r} (%)
Pre-KATRIN	100	$49 + \theta_B(r)$	66	38	83.5
Post-KATRIN 1	80	$42 + \theta_B(r)$	74	33	-
Post-KATRIN 2	60	$36 + \theta_B(r)$	81	28	-
Post-KATRIN 3	40	$28 + \theta_B(r)$	88	22	-
Post-KATRIN 4	20	$20 + \theta_B(r)$	94	16	-
Post-KATRIN 5	3	$8 + \theta_B(r)$	99	6.2	-
Post-KATRIN 5 B_{add}	3	8	99	6.2	99.5

A further advantage is a reduction of the **fraction of falsely discarded electrons**. Adding a constant energy to every electron, allows to easier discriminate backscattered electrons.
Consider a post acceleration energy of 20 keV. In this case, electrons hit the detector with at least 20 keV. If an electron backscatters, part of the energy is deposited in the detector and the rest is carried away by the backscattered electron. As simulated in [Ren11] (see figure B.2), the deposited energy is either in the range of a few keV or in the region of the initial electrons energy. Either way, one of the two, the energy deposited in the detector or the energy carried away by the electron, would drop below the post acceleration energy. Thus vetoing would now include a trigger for low energy events. This trigger would be added to the time and spatial trigger and hence reduces the number of falsely discarded events.

Simulations with post acceleration of 10 keV

The effect of a post acceleration electrode was simulated for the Pre-KATRIN and Post-KATRIN 5 B_{add} scenarios.
Figure 4.19 shows the reflected electrons in a scatter plot of polar angle vs flight time. Compared to the case without PAE (see figure 4.14) the time of flight is slightly reduced, from $\Delta t_{99,\mathrm{noPAE}} \lesssim 0.35\,\mu$s to $\Delta t_{99,\mathrm{PAE}} \lesssim 0.2\,\mu$s in the Pre-KATRIN scenario.
The Pre-KATRIN case again shows two populations: one reflected at the detector magnet, the other one reflected at the pinch magnet. In case of PAE, the maximal angle that leads to backscattering is increased as compared to the case of no PAE, i.e. more electrons are back-reflected. This is due to the fact, that the electric field tilts the electrons momentum polar angle θ_{p} according to 4.28, with $\theta_{\mathrm{p}} \hat{=} \theta_{\mathrm{p,fi}}$. Solving the equation for an electron energy of 10 keV(20 keV) yields an angle 161° (145°).

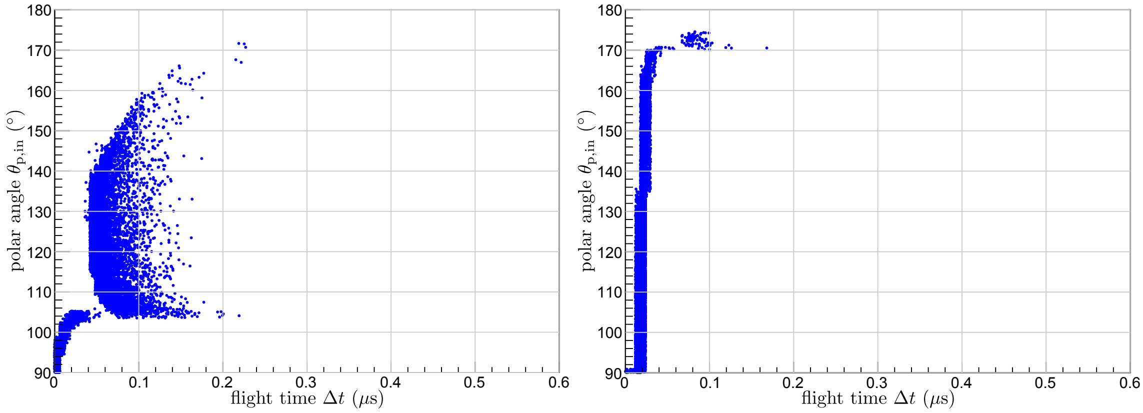

(a) Pre-KATRIN 10 kV

(b) Post-KATRIN 5 B_{add} 10 kV

Figure 4.19.: Scatter plot of polar angle vs flight time for the Pre-KATRIN scenario (a) and the Post-KATRIN 5 B_{add} scenario (b), with an additional post acceleration of 10 kV.

Table 4.7.: Time and position quantiles similar to table 4.5, but with considering a Post Acceleration Electrode with $U = 10$ kV. The values in this table are based on 500, 000 simulated electron events.

type	Δt (μs)		$\lvert\Delta\vec{x}\rvert$ (mm)		$\lvert\Delta r\rvert$ (mm)		$\lvert\Delta\varphi\rvert$ (°)	
	99%	99.9%	99%	99.9%	99%	99.9%	99%	99.9%
Pre-KATRIN	0.290	0.350	0.285	0.330	0.214	0.252	1.24	3.23
Pre-KATRIN 10 kV	0.138	0.184	0.397	0.455	0.309	0.364	1.70	3.34
Post-KATRIN 5 B_{add}	0.172	0.248	10.1	11.8	7.21	8.84	6.18	14.1
Post-KATRIN 5 B_{add}, 10 kV	0.0360	0.0921	15.5	17.5	11.3	13.2	11.0	26.0

Figure 4.20 illustrates the guiding center and position shift of reflected electrons, that return to the detector surface. On the left (right), the Pre-KATRIN (Post-KATRIN 5 B_{add}) scenario is depicted. Comparing to the case without post acceleration in figure 4.17 (4.18), both the guiding center and the position change is increased by about a factor of 1.5. This small increase can be explained by the additional electric field, that changes the drift motion.

4.3. Simulating the β-decay spectrum

Up to now, the simulations only considered generic distributions, i.e. the electrons where generated with a uniform energy distribution and emitted with isotropic momenta.
In order to investigate the impact of effects, such as backscattering and detector dead layer, to the β-decay spectrum, the afore mentioned tracking and backscattering simulations were combined to form a global Monte Carlo simulation.

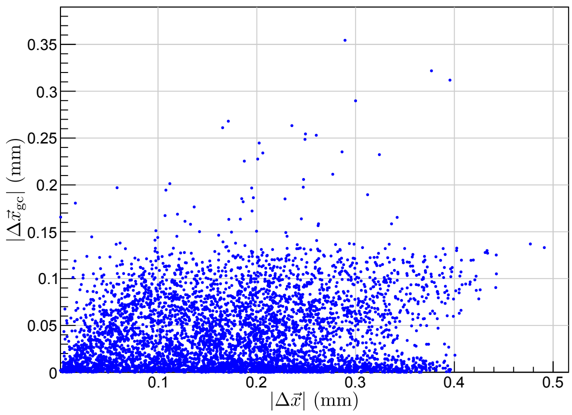

(a) Pre-KATRIN 10 kV

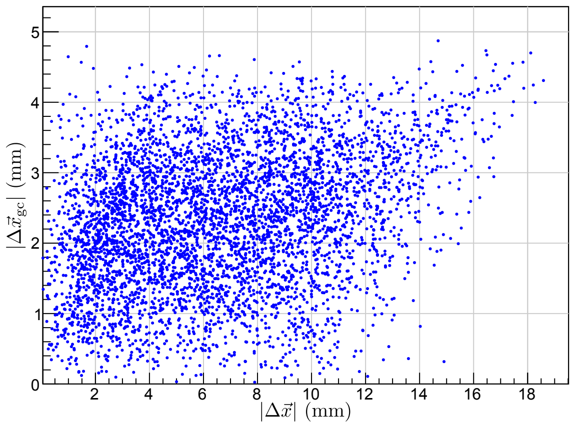

(b) Post-KATRIN 5 B_{add} 10 kV

Figure 4.20.: Scatter plot guiding center shift vs total position change for the Pre-KATRIN scenario (a) and the Post-KATRIN 5 B_{add} scenario (b), with an additional post acceleration of 10 kV.

4.3.1. Simulation method

In order to investigate the small signature of a sterile neutrino, a high statistics MC-simulation of the β-decay spectrum is required. A simulation based on single-electron tracking, would not be feasible to achieve high enough statistics in reasonable time. Consequently, a novel technique to simulate the tritium β-decay spectrum was developed in this work. It is based on Probability Density Functions (PDFs) that are generated via electron tracking prior to the spectrum simulations. To generate the spectrum one samples from these PDFs which is much faster than individual electron tracking. An electron is defined by the parameters

$$t, x, y, z, E_{\text{kin}}, \theta_{\text{p}}, \tag{4.29}$$

where t is the arrival time of the electron at the detector, x, y, z are the position at which the electrons hits the detector, E_{kin} is its kinetic energy and θ_{p} is its momentum polar angle. Due to the axial symmetry, the azimuthal momentum angle φ_{p} is not used. The detector is positioned in the x,y-plane and the beam axis is along z.
The simulation scheme is presented in figure 4.21. The general idea of the simulation is to …

1. …draw an energy according to the tritium β-decay energy distribution, draw an initial position x, y, and draw an incident angle θ_{p} from the distribution, generated via MC-simulation, as presented in section 4.2.2.
2. …dice whether this electron is backscattered based on the backscattering probability as a function of E_{kin} and θ_{p}. Here we use the data from [Ren11], see figure B.1.
    - If not backscattered: save this event, i.e. write the electron parameters (equation 4.29) to an event library. Repeat the procedure from step 1.

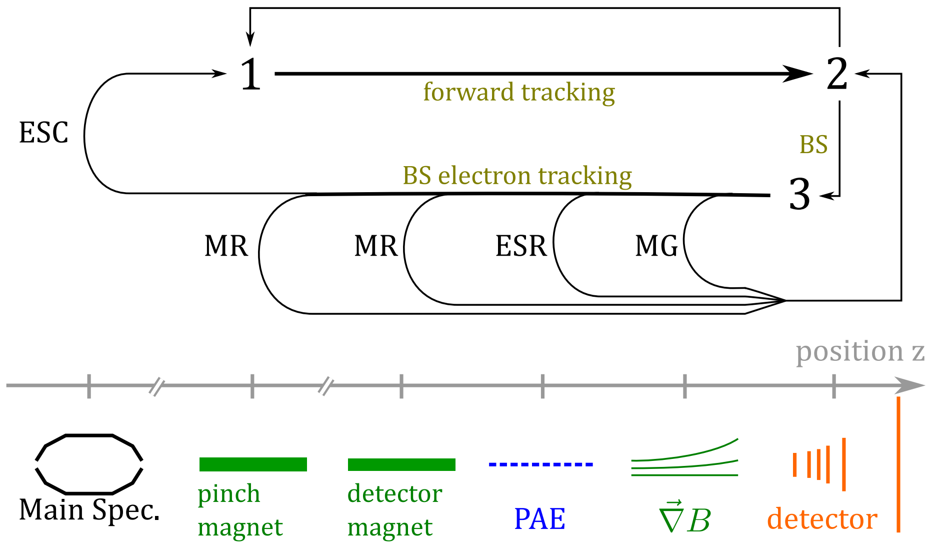

Figure 4.21.: Schema illustrating the algorithm used to build the event library. The yellow text highlights additional tracking and backscattering (BS) simulations with KASSIOPEIA, respectively KESS. If electrons escape (ESC) into the Main Spectrometer, their energy is lost. Otherwise electrons return to the detector due to: magnetic reflection (MR), electrostatic reflection (ESR) or magnetic guidance (MG).

- If backscattered: Draw an angle θ_p according to the angular distribution of backscattered electrons, and an energy E_{bs} according to the energy distribution of backscattered events. Here we use [Ren11], see figure B.3 and B.2. The energy deposited E_{dep} in the detector in the first hit is given by $E_{dep} = E_{kin} - E_{bs}$. Save the deposited energy and the rest of the parameters from the electron hitting the detector in the event library.

3. …based on the angle, energy and radius decide whether the electron will be magnetically back-reflected. This is based on the MC-simulations as presented in section 4.2.3.

   - If not magnetically reflected: the electron escapes into the Main Spectrometer and is not detected. Repeat the procedure from step 1.

   - If magnetically reflected: draw the time Δt after which it arrives again at the detector, and the new position x, y, z from the distributions derived in section 4.2.3. Repeat the procedure from step 2.

Following this algorithm, the database is a list of electron parameters, for electrons, that hit the detector.

$$
\begin{aligned}
&t_1, x_1, y_1, z_1, E_{\text{kin},1}, \theta_{\text{p},1} \\
&t_2, x_2, y_2, z_2, E_{\text{kin},2}, \theta_{\text{p},2} \\
&t_3, x_3, y_3, z_3, E_{\text{kin},3}, \theta_{\text{p},3} \\
&\vdots
\end{aligned}
\tag{4.30}
$$

The advantage of this procedure is, that effects such as backscattering, energy threshold etc. can be easily investigated:

- If we consider the sum of all deposited energies per event, we retrieve the original tritium β-decay spectrum modified by those events, that backscatter and escape.
- If we assume a perfect backscattering veto, we can neglect all events that hit detector more than once, and we see the tritium spectrum with reduced statistics.
- We can also consider a veto based on a position and time cut, as described in section 4.1.3. In this case one can evaluate the fraction of missed events or falsely vetoed events.
- Additionally, we can investigate detector effects, such as the energy threshold or the detector dead layer. For the energy threshold, we do not consider electrons if they deposited an energy below E_{th}, whereas for the detector dead layer, we calculate an effective energy, deposited in the sensitive detector volume.

4.3.2. Impact of detector backscattering

To qualitatively investigate the spectral distortions due to backscattering, compared to the effect of a sterile neutrino, we chose as initial spectrum a tritium β-decay spectrum with the imprint of a sterile neutrino at $m_4 = 8\,\text{keV}$ and a nonphysically large mixing angle of $\sin^2\theta = 0.3$.
Figure 4.22 shows the initial spectrum in black. Plotting every recorded deposited energy in the event library, gives an energy spectrum impacted by detector backscattering, illustrated in green.
backscattered electrons deposit only a part of their energy upon hitting the detector for the first time. If the electrons are then magnetically reflected, they hit the detector again and may backscatter once more. Consequently, the number of detector events counted is higher in the case of backscattering. This especially effects the low energy region $E_{\text{kin}} < 4\,\text{keV}$ of the energy spectrum, since the energy of backscattered electrons is mostly below 1 keV (see figure B.2, and B.3).
The figure furthermore displays a spectrum with a godly veto on backscattered electrons, i.e. all energy deposition that are due to backscattered electrons are omitted. Hence, the number of events decreases.

To better express the sterile neutrino signature, in figure 4.23 the ratio of the energy spectra is built. The denominator spectrum is purely theoretical, i.e. no statistical fluctuations and neutrino mass $m_{\text{eff}} = 0\,\text{eV}$.

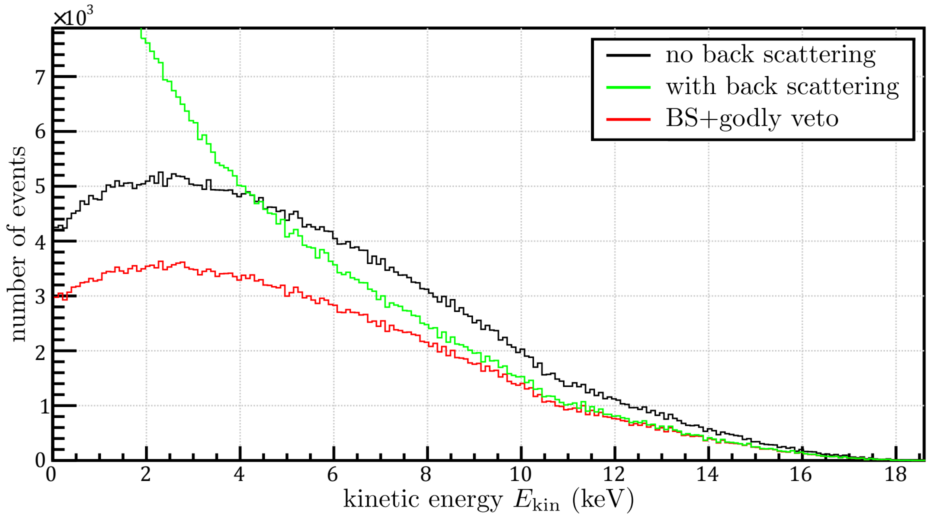

Figure 4.22.: Influence of detector backscattering to the β-decay spectrum for the Post-KATRIN 5 B_{add} scenario. The spectrum includes a sterile neutrino with mass $m_4 = 8$ keV and exaggerate mixing of $\sin^2\theta = 0.3$. Backscattering results in an increase of low energy electrons.

Additionally to the godly veto, a veto mechanism with 99% quantiles (time+area-trigger), as introduced in section 4.1.3, was applied for the Post-KATRIN 5 B_{add} scenario. Depending on the detector rate 10^8 cps (10^9 cps), the fraction of falsely discarded electrons is 4.5% (38%), similar to the estimations in section 4.1.3 figure 4.6a. Surprisingly, the fraction of vetoed events, that originate from backscattering, is smaller as the used 99% time and position quantiles for the triggers (table 4.1):

$$P_{bsv} = \frac{N_{bsv}}{N_{bs,tot}} = 72.9\%(77.3\%) \tag{4.31}$$

Here $N_{bs,tot}$ (N_{bsv}) denotes all events (the number of vetoed events) that are related to backscattered electrons.
The fraction of vetoed backscattered electrons is affected by the position and time trigger from the applied veto mechanism. The applied veto strongly depends on the veto type and the applied trigger threshold values. In figure 4.22 the trigger threshold values applied, were derived from simulations in section 4.2.3. The simulation was based on generic parameter distributions, i.e. uniform energies $E_{kin,in} \in [0.2\,\text{keV}, 20\,\text{keV})$ and isotropic momenta directions $\theta_{p,in} \in [90°, 180°)$. In the case of β-decay electrons …:

- Flight time:
  …electrons in the low energy regime are more probable and $E_{kin,in} \in [0\,\text{keV}, 20\,\text{keV})$. Moreover, backscattered electrons are mostly in an energy regime below 1 keV (see figure B.2). Low energy electrons lead to an increase of electrons with high flight times and consequently shifts the time quantile to higer values. Moreover

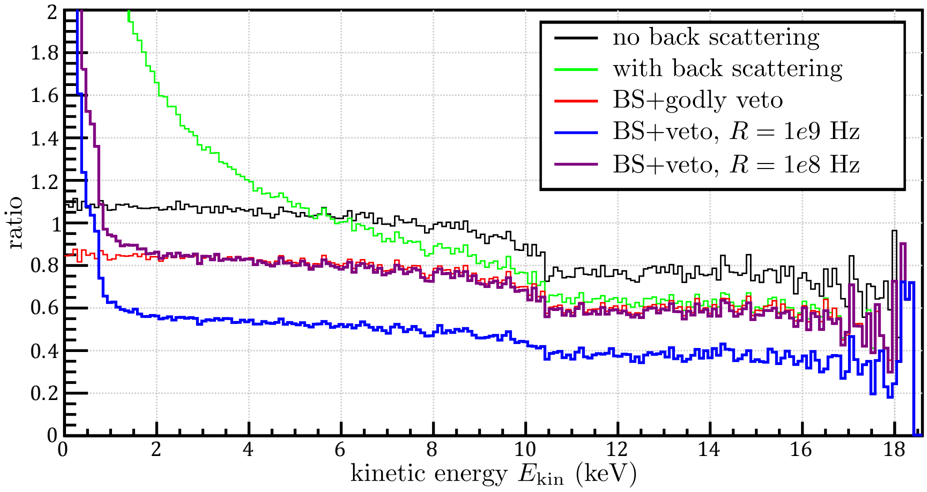

Figure 4.23.: Spectrum ratio for the Post-KATRIN 5 B_{add} scenario, depicting the impact of veto mechanisms on detector backscattering, as introduced in section 4.1.3. The used 99% quantiles are noted in table 4.1. Depending on the detector rate 10^8 cps (10^9 cps), 2.3% (20%) of the non-backscattered events are falsely discriminated.

For increasing detector rates, the fraction of falsely discarded electrons also increases, which is explained by an increase of coincidences in the same time frame. Consequently, some of the electron events will coincide with backscattering related events and hence the fraction of vetoed backscattered events also increases slightly (equation 4.31).

- Position change:
  ...backscattered electrons tend to be emitted not isotropic, but with polar angles below 150° (see figure B.3). Especially in the case of multiple backscattering, the polar angle will shift to shallower angles $90° - 130°$. This impacts the position change due to the guiding center drifts (equation 4.24) and thus increases the position quantile.

In table 4.8, the fraction of falsely discarded events and the fraction of backscattering events correctly vetoed is listed for two simulated detector scenarios and trigger threshold quantiles. We note, that in the Pre-KATRIN scenario, the fraction of falsely discarded electrons is much lower than in the Post-KATRIN 5 B_{add} case. This originates from the position change of backscattered electrons. The position change over pixel radius scales proportional to the detector radius (4.22), thus small detector radii lead to a smaller relative effect of gyromotion. This results in smaller trigger threshold values for vetoing backscattered electrons and thus reduces the fraction of falsely discarded events.

Table 4.8.: Fraction of falsely discarded electron events and fraction of vetoed backscattering events for different applied trigger thresholds, detector rates and detector scenarios. The trigger thresholds are based on simulated quantiles and listed in table 4.7

quantiles		99%		99.9%	
Γ_{det} (cps)		10^8	10^9	10^8	10^9
Pre-KATRIN	P_{fd} (%)	0.312	3.06	0.554	5.22
	P_{bsv} (%)	70.9	71.6	75.1	76.2
Post-KATRIN 5 B_{add}	P_{fd} (%)	4.50	38.0	8.71	60.4
	P_{bsv} (%)	72.9	77.3	84.5	88.9

4.3.3. Impact of the energy threshold

In the previous section, the impact of backscattered electrons to the β-decay spectrum was demonstrated. Now we analyze the impact of the energy threshold to the energy spectrum, i.e. the lowest detectable electron energy. In particular, the energy threshold impacts the β-decay energy spectrum, when applying veto mechanisms for backscattered electrons. It is expected, that the fraction of vetoing backscattered electrons decreases for an increase of the energy threshold. Since the energy of backscattered electrons mostly range in the regime below 1 keV, the respective event may fall below the energy threshold and thus not be detected. Moreover, the veto mechanism searches for particle coincidences, thus backscattered electrons will not be vetoed, if one of the detector hits is not detected.
The impact of the energy threshold to the energy ratio, when applying a backscattering veto, is illustrated in figure 4.24. The underlying simulation setup is the Post-KATRIN 5 B_{add} scenario with a detector rate of 10^8 cps and 99% trigger quantiles. We see that low energy thresholds yield the best vetoing result over the energy range $E_{\mathrm{kin}} \in [0\,\mathrm{keV}, 18.6\,\mathrm{keV}]$.

At a closer look, for energy thresholds of 0, 0.5, 2 keV, the fraction of vetoed backscattered electrons is 72.9, 78.9, 55.5 % and the fraction of falsely discarded electrons is 4.50, 4.30, 3.4 %. For increasing thresholds the fraction of falsely discarded electrons decreases, which results in a decrease of the electron statistics and finally in a decrease of the probability of coincident signals.
Instead the fraction of vetoed backscattered electrons increases for low energy thresholds $E_{\mathrm{th}} < 1\,\mathrm{keV}$ and decreases for higher values $E_{\mathrm{th}} > 1\,\mathrm{keV}$. The increase at $E_{\mathrm{th}} < 1\,\mathrm{keV}$ originates from the fact, that most of the backscattered electron events have energies below 1 keV, which leads to longer flight times. These events are typically not vetoed by the time trigger and reduce P_{bsv} at $E_{\mathrm{th}} = 0$. With a non-zero energy threshold, these events are omitted from detection and thus indirectly improve the veto mechanism. As for the decrease of P_{bsv} at $E_{\mathrm{th}} > 1\,\mathrm{keV}$. Detector backscattered electrons with energies below the energy threshold will not be detected. Consequently the veto mechanism, which discriminates coincident events, will not veto backscattering events, where the backscattered electron has energies below the energy threshold, which decreases the veto mechanism, $P_{\mathrm{bsv}} \searrow$.

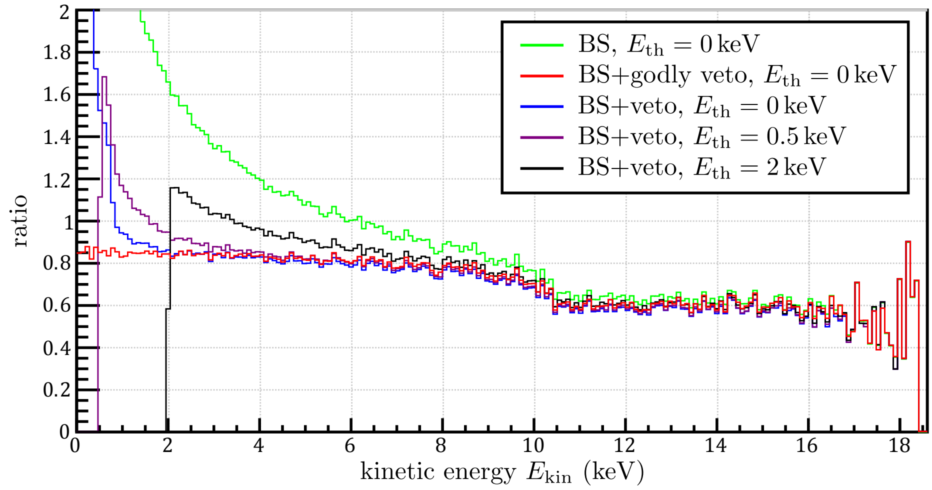

Figure 4.24.: Impact of the energy threshold to the β-decay spectrum and the backscattering veto mechanism for the Post-KATRIN 5 B_{add} scenario. The green line depicts an energy spectrum without any veto mechanism applied. High energy threshold values decrease the fraction of vetoed backscattered electrons.

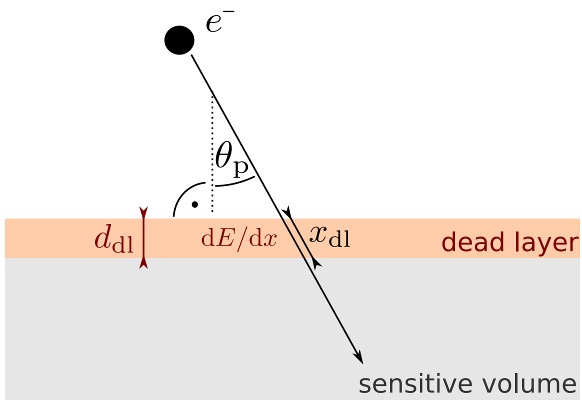

Figure 4.25: Simplistic detector dead layer model, consisting of a constant energy loss. Depending on the incident angle, electron lose a certain amount of energy, while flying through the non sensitive detector layer with thickness d_{dl}.

4.3.4. Impact of the detector dead layer

The detector used in the KATRIN experiment and the TRISTAN-project is a Silicon drift detector. In general, the detector consists of a pn-junction, i.e. a semiconductor divided in two areas, a positive and a negative doted area. By applying an external voltage in reverse bias-mode, the bulk of the detector-medium is depleted of the electric charges. The depleted zone is referred to as depletion region and corresponds to the sensitive detector volume.

An electron incident electron would thus travel through the detector and lose its energy through elastics scattering with the medium. If the electron scatters within the depletion region, the deposited energy is measured. Vice versa, the deposited energy in the region outside of the depletion region is not measured. This region is referred to as the detector dead layer and illustrated in figure 4.25.
To investigate the impact of detector dead layer to the β-decay spectrum, a simple model

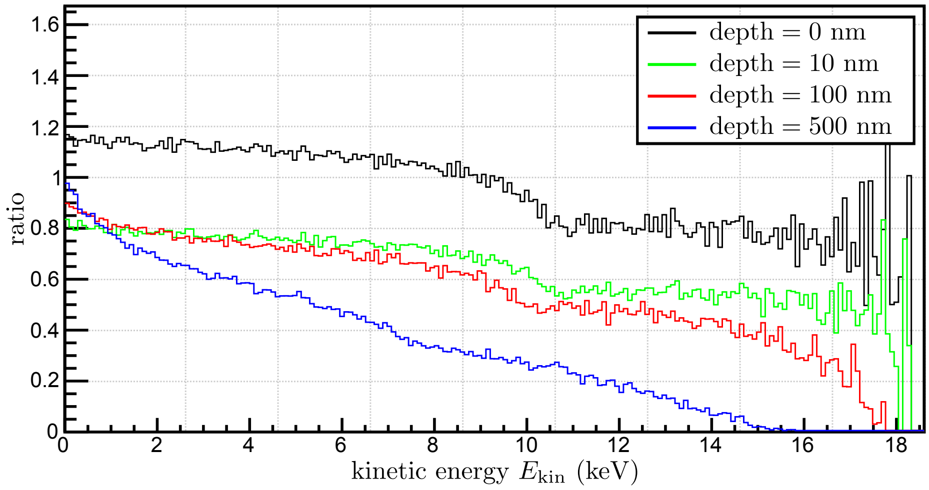

Figure 4.26.: Electron energy spectrum ratio, illustrating the impact of the detector dead layer. With increasing thickness of the dead layer, the spectrum shifts to lower energies and the sterile neutrino signature is smeared.

with constant energy loss along the flight path and a homogeneous dead layer of thickness d_{dl} was implemented. The energy loss in the dead layer is hence given by

$$E_{\mathrm{loss}} = \frac{\mathrm{d}E}{\mathrm{d}x} \cdot x_{\mathrm{dl}} = \frac{\mathrm{d}E}{\mathrm{d}x} \cdot \frac{d_{\mathrm{dl}}}{\cos\theta_{\mathrm{p}}}, \tag{4.32}$$

where x_{dl} denotes the distance traveled in the dead layer and θ_{p} is the incident angle of the electron.

In figure 4.26, the effect of the detector dead layer, in particular the dead layer thickness, is displayed. For a thickness of 100 nm, the sterile neutrino signature shifts by about 0.5 keV, compared to the ratio without dead layer, $d_{\mathrm{dl}} = 0$ nm. Moreover, the sterile neutrino signature is smeared and at a thickness of 500 nm it is not visible anymore.

4.4. Detector & read-out characterization at CEA

On the road of developing the new detector section for the TRISTAN-project, the first silicon drift detectors have been produced and bonded to electronic read-out devices. In order to specify the prototypes, a test bench was constructed at KIT and at CEA. While the test bench at KIT is constructed in corporation with the IPE and will develop the whole read-out electronics along with the silicon drift detector [Dol16], the test bench at CEA is based on already existing read-out devices and allows to quickly specify prototype detectors.

The work presented in this thesis is divided into the introduction of the read-out system, the specification of the read-out ASIC, using an oscilloscope, and the first measured x-ray spectra, recorded with prototype silicon drift detectors built at HLL-Munich.

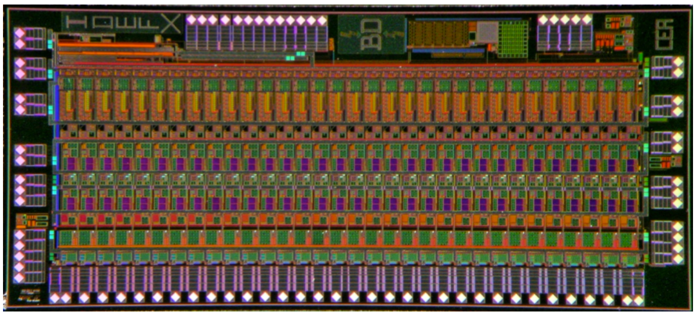

Figure 4.27: Picture of the IDeF-X BD ASIC. Each of the 32 channels has an amplification, a filter and an output stage. The maximum charge of each channel is memorized and returned via a multiplexed output line [Lim11].

4.4.1. The read-out system

The read-out system comprises of the front end and the back end electronics. The front end electronics consist of signal amplifier, energy thresholds and signal filters, whereas the back end electronics encompasses the analogue digital converter (ADC), the slow control as well as the power supply units. The slow control embodies the communication center between the electronic components. The energy threshold of the front end electronics, may be set via the slow control for example.
For the front end read-out electronics we decided to use the IDeF-X BD ASIC ("Imaging Detector Front end in hard X-ray" version "BD"; Application-Specific Integrated Circuit). The ASIC and its different versions have been developed over the last 14 years and have been successfully utilised in satellite missions, such as SVOM, CINEMA or ASTRO-H [Mic10; Gev09].

IDeF-X BD covers an energy range of $\approx 0.3 - 50$keV and allows for both anode and cathode read-out polarity, i.e. the ASIC is programmable via slow control, to work with either negative charges (anode mode) or positive charges (cathode mode). IDeF-X BD provides shaping times between $0.9\,\mu$s and $9.6\,\mu$s, and was designed for detectors with capacities of $2 - 5$ pF and leakage currents below < 1 nA.
Each of the 32 channels memorizes the maximum signal after the amplification and filtering stage, and is equipped with a low level threshold. The ASIC output returns the multiplexed maximum signal of the 32 channels. The output has three different modes: "all channels", "reacted channels only" or "programmed channels". In the "programmed channels" mode, only predefined channels are read out. Furthermore, the ASIC allows to directly view the unshaped and shaped signal of channel 31 on the output line.

In figure 4.28 the definition of the shaping time is illustrated. In general, the shaping time defines the time frame, in which the input signal reaches the maximum value. The shaping time is important, considering the effect of electronic noise. For low shaping times, the impact of $1/f$ noise increases, whereas for higher shaping times electronic noise is dominated by thermal noise.

In order to reduce electronic noise, the ASIC is directly positioned next to the silicon drift detector (see figure 4.29) and only the mid sized geometry is connected to the ASIC, since additional wire bonds might interact and induce further electronic noise.
The board displayed is referred to as the detector PCB (Printed Circuit Board). The connec-

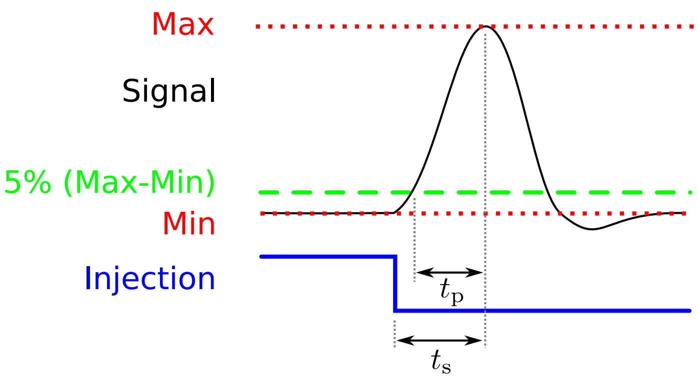

Figure 4.28: Definition of the shaping t_s and peaking time t_p. Low shaping times reduces the thermal noise, while increasing $1/f$ noise and vice versa.

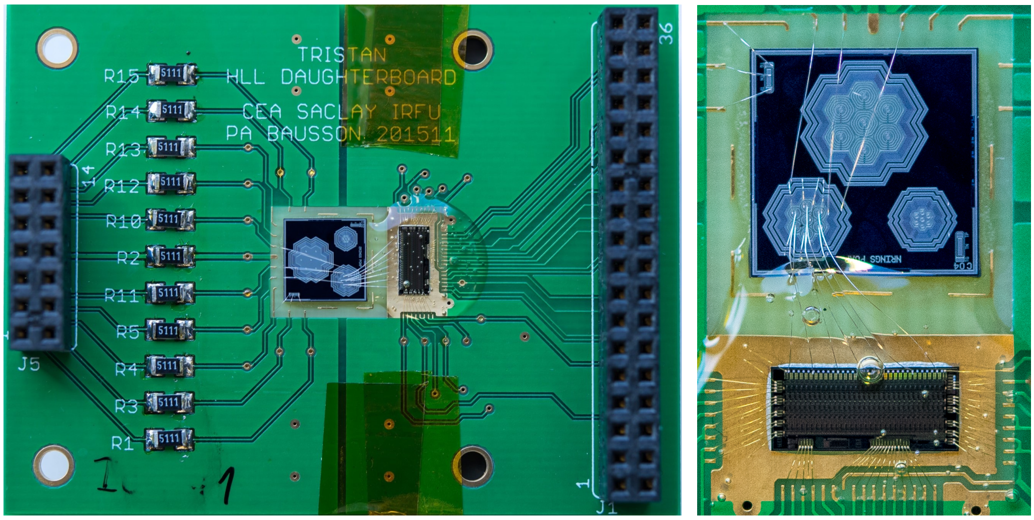

Figure 4.29.: Picture of the 65 mm long detector board with mounted prototype detector chip and IDeF-X BD ASIC (left). The right picture shows a magnified view of the detector and ASIC region. The mid sized geometry on the detector chip and the ASIC are connected by wire bonds.

tors on the right of the detector PCB, lead to the ADC, the slow control and to the ASIC power supply. The connector on the left side of the detector PCB is for the detector power supply, i.e. the bias voltage, the drift ring voltages and voltage for the temperature sensor.

4.4.2. Measurements with the IDeF-X ASIC

Before specifying the prototype detectors, we first investigate the capabilities of the IDeF-X ASIC. In particular we are interested in the energy resolution, i.e. the electronic noise of the IDeF-ASIC.
In a setup as displayed in figure 4.30, an attenuated square-wave voltage U_{inj} was injected into IDeF-X BD. Internally, the square-wave voltage is conveyed to each ASIC channels injection lines, with a corresponding injection capacitance of $C_{\mathrm{inj}} = 200\,\mathrm{fF}$. The connection to the PC allows to switch between the ASIC polarity and the read-out modes, and sets

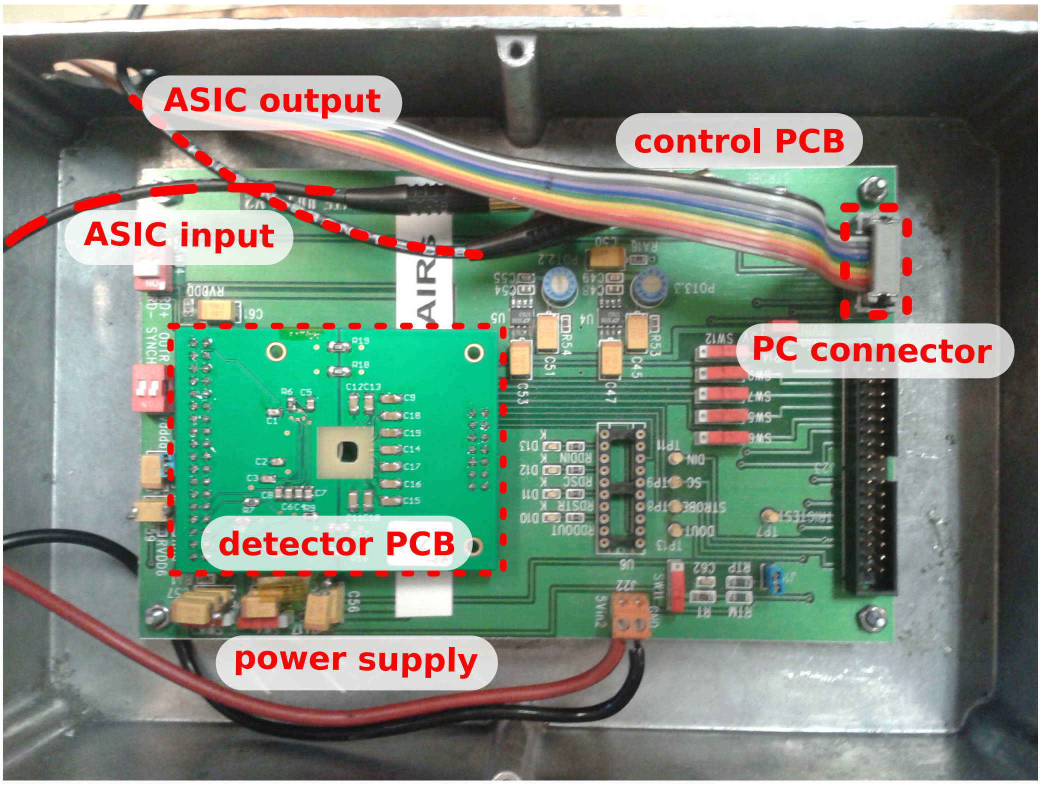

Figure 4.30.: Test setup for investigating the IDeF-X BD ASIC. The ASIC is mounted on the detector PCB and the detector PCB is mounted on the control PCB. The control PCB is used to deliver the different ASIC voltages, to connect the input and the output line, and to allow ASIC programming via the PC connection.

the shaping time and the energy threshold levels.

ENC in anode and cathode mode

A possibility to measure the resolution of the electronic setup is the equivalent noise charge (ENC). The ENC expresses the amount of charges induced due to electronic noise

$$ENC = \frac{\sigma_\mathrm{n}}{U_\mathrm{s}} \cdot \frac{Q_\mathrm{inj}}{e}, \tag{4.33}$$

where σ_n depicts the standard deviation of the fluctuating signal, $Q_\mathrm{inj} = C_\mathrm{inj} \cdot \mathrm{U}_\mathrm{inj}$ denotes the injected charges into the ASIC and U_s is the amplified signal voltage. In order to measure σ_n and U_s, the ASIC is programmed to return only the shaped signal of channel 31. The ASIC output was then analyzed on an oscilloscope.

Figure 4.31 depicts the calculated ENC values for the IDeF-X BD ASIC in anode and cathode mode. The errorbars for the cathode mode depict the sample standard deviation for repeated ENC measurements of six different IDeF-X BD ASICs.
The increased ENC value at shaping times 9.6 μs, originates from the additional power

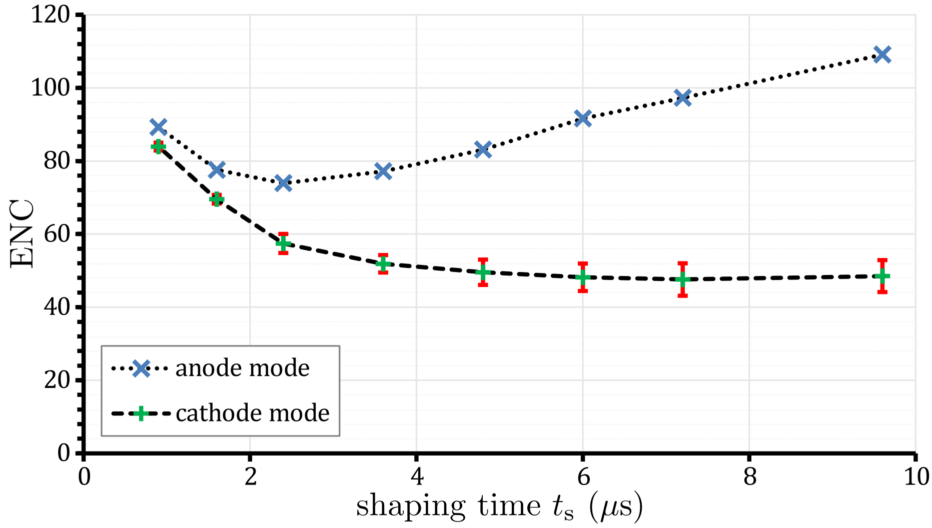

Figure 4.31.: Measured ENC-values for the IDeF-X ASIC in cathode (green) and anode (blue) mode. The errorbars in cathode mode are derived from multiple measurements with different detector PCBs, i.e. different IDeF-X BD ASICs. In anode mode, the ASIC requires an additional injection current — equivalent to a leakage current — to make the ASIC work. The additional current increases the noise and thus the ENC value.

supply for the amplifier. The inbuilt ASIC amplifier requires a small input current $\approx 1\,\mathrm{pA}$ to work properly. This current is typically given by the leakage current of the detector, or, in cathode mode, by the leakage current of two safety diodes at the ASIC input line. In anode mode, the additional power supply was set to the minimal value of 20 pA.
The ENC can be converted to an energy resolution FWHM (Full Width Half Maximum), considering that resolution consists of signal and a noise component:

$$\begin{aligned} FWHM &= 2\sqrt{2\ln(2)} \cdot \sqrt{\sigma_\mathrm{s}^2 + \sigma_\mathrm{n}^2} \\ &= 2\sqrt{2\ln(2)} \cdot \sqrt{f E_\mathrm{eh} E_\mathrm{in} + (ENC \cdot E_\mathrm{eh})^2}, \end{aligned} \tag{4.34}$$

with the energy standard deviation originating from noise σ_n and from the signal σ_s. The signal energy resolution is given with consideration to the mean incident energy E_in, the energy needed to create a charge carrier E_eh, and the fano factor, $f = 0.115$ in silicon [Fan47; Ali80]. The noise energy resolution is based on the fact that the creation of each equivalent noise charge (ENC) needs a certain amount of energy E_eh. In figure 4.32 the energy resolution (equation 4.34) is illustrated for different incident electron energies.

Energy resolution by repeated injections

The ASIC energy resolution may be also derived, by injecting a square-wave voltage with frequency f and memorizing each ASIC output value over a certain time frame. For an injection with amplitude U, the energy resolution would be given by the spread σ_U of

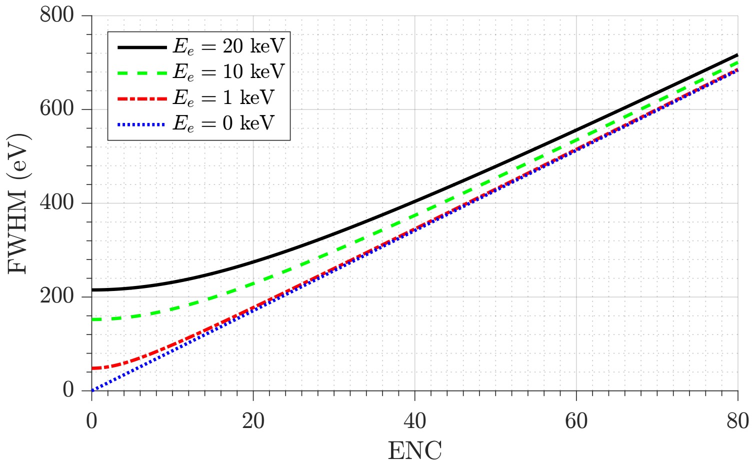

Figure 4.32: Conversion of Equivalent Noise Charge ENC to the energy resolution FWHM, expressed as the full width half maximum, for different incident electron energies in silicon.

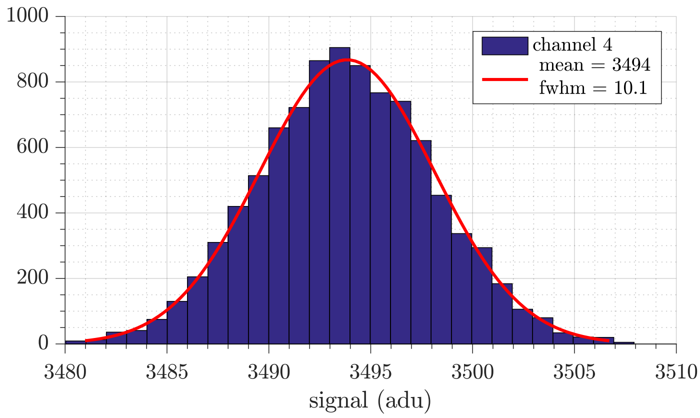

Figure 4.33: Output of the IDeF-X ASIC for channel number 4 in cathode mode, with an injection energy equivalent of 14.3 keV. The x-axis is labeled in numbers of analogue digital units. The output was fitted in order to recover the spread of the distribution and hence the energy resolution.

the recorded values. The recorded values would then follow a Gaussian distribution with mean $\mu = U$ and $\sigma = \sigma_U$.

The energy equivalent to the injected and attenuated square-wave voltage, is derived from the injected charge

$$C_{\text{inj}} \cdot U_{\text{inj}} = Q_{\text{inj}} = \frac{E_{\text{inj}}}{E_{\text{eh}}}, \tag{4.35}$$

where C_{inj} denotes the capacity of the each channel, U_{inj} denotes the attenuated injection voltage at the ASIC input and E_{eh} is the energy needed to create a charge carrier in silicon. In figure 4.34 the energy resolution for each channel is presented for a constant shaping time of 9.6 μs. Each point encompasses a statistic of about 300, 000 memorized injections. Moreover, the graph also displays the two ASIC polarities, anode and cathode mode. As expected from figure 4.31, the anode mode is about a factor of two worse.
Comparing the energy resolution of neighboring channels, a deviation of about 10% is seen. This could originate from an uncertainty of 10% on the injection capacitance for each channel and would affect the energy calibration noted in equation 4.35.

Before mounting the silicon drift detector, the measurements described above were repeated for each detector board. The best board, i.e. the board with the best energy reso-

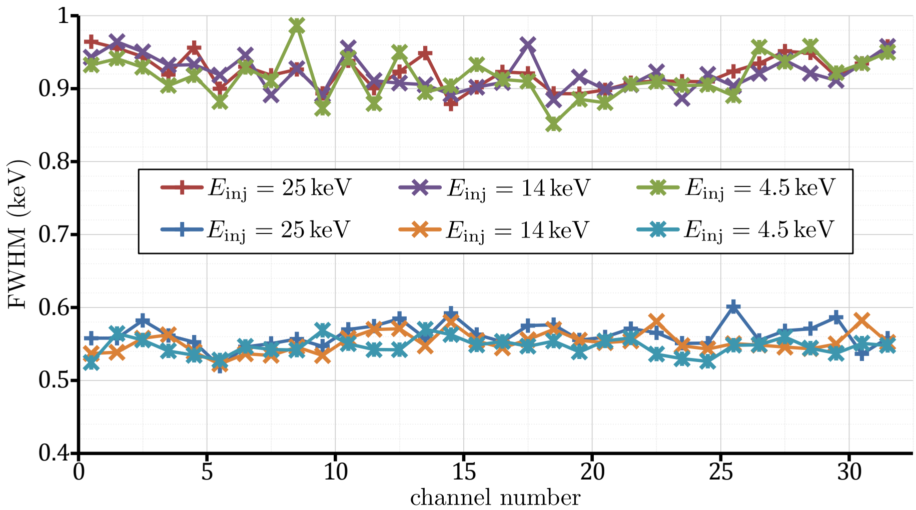

Figure 4.34.: Energy resolution for the IDeF-X ASIC operated in anode mode (upper curves) and cathode mode (lower curves). The shaping time is 9.6 μs.

lution, was then sent to HLL for the detector bonding and is presented in the next section. There the first x-ray spectra of a ^{57}Co- and a ^{241}Am-calibration source are presented.

4.4.3. First spectra

The experimental setup for measuring the first x-ray spectra is similar to the setup illustrated in figure 4.30 and 4.29. The prototype detector is mounted on the detector PCB and the mid sized geometry ($2r_{\text{px}} = 500\,\mu$m) with three drift rings is connected to the IDeF-X ASIC. Lastly, the radioactive source is placed 1 cm of the prototype detector.

In figure 4.35 the measured and calibrated energy spectrum for a ^{57}Co- and a ^{241}Am-calibration source is displayed. For the energy calibration, the position of the decay lines were determined by fitting a Gaussian distribution to the calibration lines in the spectrum. With regards to literature values from [Chu99], a linear regression was then employed, weighted by the width of the decay lines, for converting the digital output into an energy scale.

Interestingly the width of the decay lines, i.e. the energy resolution of the setup, is about $FWHM \approx 500$ eV, which corresponds to an ENC value of about 55 (see figure 4.32). These values match quite good with afore measured values for an ASIC in cathode mode (see figure 4.34 and 4.31 ($t_s = 9.6\,\mu$s)).

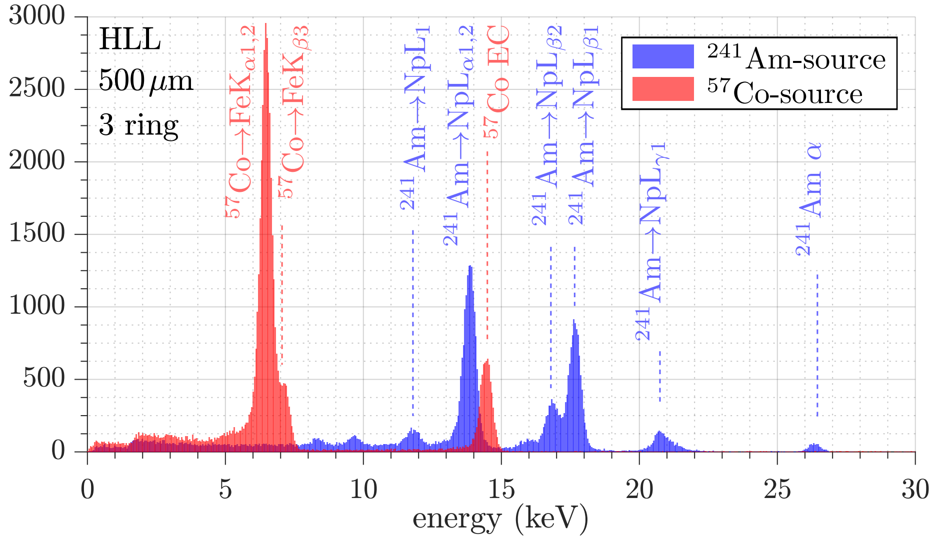

Figure 4.35.: Fully calibrated gamma-spectrum of the ^{57}Co-source (red) superimposed with the ^{241}Am-source (blue) for one detector pixel. The highlighted maxima were used for the energy calibration.

5. Conclusion

Sterile neutrinos are a well motivated extension of the Standard Model of Particle Physics. Sterile neutrinos in the eV-mass range are motivated by several anomalies in short-baseline experiments, and keV-scale sterile neutrinos are viable dark matter candidates. Beyond the determination of the effective neutrino mass, the KATRIN experiment allows to search for sterile neutrinos both in the eV- and keV-mass range.

Within this thesis, the combined sensitivity to eV-scale sterile neutrinos of the KATRIN and SOX experiments was studied for the first time. It is demonstrated, that, due to the complementarity of both experiments, the entire preferred parameter range for sterile neutrinos can be tested by a combined analysis.

Moreover, the impact of the possible existence of an eV-scale sterile neutrino on the neutrino mass sensitivity of KATRIN was studied. Here, a novel approach, using the prospective measurement results of SOX as an input for the KATRIN data analysis was explored. By constraining the sterile neutrino parameters in this way, the degeneracy between the active neutrino mass and sterile neutrino mass and mixing angle can be dissolved. Consequently, KATRIN's neutrino mass sensitivity becomes largely independent of a possible existence of a sterile neutrino.

The second part of the thesis focuses on a keV-scale sterile neutrino search with KATRIN. First detailed design studies for a future detector and read-out system were carried out in this work. Special focus was put on the study of detector systematic effects, arising from charge-sharing, detector backscattering, and pile-up. As a result, general design parameters such as the number of detector pixels, detector radius, and detector position were optimized. Furthermore, the effectiveness of a potential backscattering veto-system was analyzed.

Finally, in this work the first characterization of a prototype for the future KATRIN detector was carried out. The thin-deadlayer, multi-drift ring Si-detector, produced at the Halbleiterlabor of the Max-Plank-Society, was equipped with an ASIC preamp of CEA. During a 4-month research stay at CEA, the system was commissioned, the electronics were tested, and later the first physics spectra of x-ray calibration sources were analyzed. These first tests demonstrate the functionality of the detectors and a reveal a good energy resolution and linearity of the system. These measurements and the above-mentioned simulation studies will be essential in determining the path towards the final multi-pixel Si-detector system for a keV-scale sterile neutrino search with KATRIN.

List of Figures

List of Tables

Bibliography

[Aba12] K. N. Abazajian et al. "Light Sterile Neutrinos: A White Paper". In: (2012). arXiv: 1204.5379 [hep-ph].

[Abe14] K. Abe, J. Adam, H. Aihara, et al. "Precise Measurement of the Neutrino Mixing Parameter θ_{23} from Muon Neutrino Disappearance in an Off-Axis Beam". In: *Phys. Rev. Lett.* 112 (18 2014), p. 181801. DOI: 10.1103/PhysRevLett.112.181801.

[Ade14] P. A. R. Ade, N. Aghanim, C. Armitage-Caplan, et al. "Planck 2013 results. XVI. Cosmological parameters". In: *Astronomy & Astrophysics* 571 (2014), A16. DOI: 10.1051/0004-6361/201321591.

[Adh16] R. Adhikari et al. "A White Paper on keV Sterile Neutrino Dark Matter". In: *Submitted to: White paper* (2016). Ed. by M. Drewes et al. arXiv: 1602.04816 [hep-ph].

[Ago13] M. Agostini, M. Allardt, E. Andreotti, et al. "Results on Neutrinoless Double-β Decay of ^{76}Ge from Phase I of the GERDA Experiment". In: *Physical Review Letters* 111 (12 2013), p. 122503. DOI: 10.1103/PhysRevLett.111.122503.

[Agu09] A. A. Aguilar-Arevalo et al. "Unexplained Excess of Electronlike Events from a 1-GeV Neutrino Beam". In: *Phys. Rev. Lett.* 102 (10 2009), p. 101802. DOI: 10.1103/PhysRevLett.102.101802.

[Ahm01] Q. R. Ahmad, R. C. Allen, T. C. Andersen, et al. "Measurement of the Rate of $\nu_e + d \to p + p + e^-$ Interactions Produced by ^8B Solar Neutrinos at the Sudbury Neutrino Observatory". In: *Physical Review Letters* 87 (7 2001), p. 071301. DOI: 10.1103/PhysRevLett.87.071301.

[Ali80] R. C. Alig, S. Bloom, and C. W. Struck. "Scattering by ionization and phonon emission in semiconductors". In: *Physical Review B* 22 (12 1980), pp. 5565–5582. DOI: 10.1103/PhysRevB.22.5565.

[Ams15] J. F. Amsbaugh, J. Barrett, A. Beglarian, et al. "Focal-plane detector system for the KATRIN experiment". In: *Nuclear Instruments and Methods in Physics Research Section A: Accelerators, Spectrometers, Detectors and Associated Equipment* 778 (2015), pp. 40–60. ISSN: 0168-9002. DOI: 10.1016/j.nima.2014.12.116.

[An12] F. P. An, J. Z. Bai, A. B. Balantekin, et al. "Observation of Electron-Antineutrino Disappearance at Daya Bay". In: *Physical Review Letters* 108 (17 2012), p. 171803. DOI: 10.1103/PhysRevLett.108.171803.

[Ang05] J. Angrik et al. "KATRIN Design Report 2004". In: *FZKA Scientific Report 7090* (2005). URL: http://bibliothek.fzk.de/zb/berichte/FZKA7090.pdf.

[Arg16] C. A. Argüelles, V. Brdar, and J. Kopp. “Production of keV Sterile Neutrinos in Supernovae: New Constraints and Gamma Ray Observables”. In: (2016). eprint: `arXiv:1605.00654`.

[Asa05a] T. Asaka, S. Blanchet, and M. Shaposhnikov. “The νMSM, dark matter and neutrino masses”. In: *Physics Letters B* 631 (4 2005), pp. 151–156. ISSN: 0370-2693. DOI: `10.1016/j.physletb.2005.09.070`.

[Asa05b] T. Asaka and M. Shaposhnikov. “The νMSM, dark matter and baryon asymmetry of the universe”. In: *Physics Letters B* 620.1—2 (2005), pp. 17–26. ISSN: 0370-2693. DOI: `10.1016/j.physletb.2005.06.020`.

[Ase11] V. N. Aseev, A. I. Belesev, A. I. Berlev, et al. “Upper limit on the electron antineutrino mass from the Troitsk experiment”. In: *Physical Review D* 84 (11 2011), p. 112003. DOI: `10.1103/PhysRevD.84.112003`.

[Bab12] M. Babutzka, M. Bahr, J. Bonn, et al. “Monitoring of the operating parameters of the KATRIN Windowless Gaseous Tritium Source”. In: *New Journal of Physics* 14.10 (2012), p. 103046. URL: `http://stacks.iop.org/1367-2630/14/i=10/a=103046`.

[Bab14] M. Babutzka. “Design and development for the Rearsection of the KATRIN experiment”. PhD thesis. Karlsruhe Institut für Technologie, 2014.

[Bor06] B. Bornschein. “The closed tritium cycle of KATRIN”. In: *Progress in Particle and Nuclear Physics* 57 (2006), pp. 38–48. DOI: `10.1016/j.ppnp.2005.12.004`.

[Boy06] A. Boyarsky et al. “Constraints on sterile neutrinos as dark matter candidates from the diffuse X-ray background”. In: *Monthly Notices of the Royal Astronomical Society* 370.1 (2006), pp. 213–218. DOI: `10.1111/j.1365-2966.2006.10458.x`.

[Cha14] J. Chadwick. “Intensitätsverteilung im magnetischen Spektrum der Betastrahlen von Radium B+C”. In: *Verhandlungen der Deutschen Physikalischen Gesellschaft* 16 (1914), pp. 383–391.

[Cha32] J. Chadwick. “Possible Existence of a Neutron”. In: *Nature* 129 (1932), p. 312. DOI: `10.1038/129312a0`.

[Chu99] S.Y.F. Chu, L.P. Ekström, and R.B. Firestone. *The Lund/LBNL Nuclear Data Search*. 1999. URL: `http://nucleardata.nuclear.lu.se/toi/` (visited on 05/08/2016).

[Cow11] G. Cowan et al. “Asymptotic formulae for likelihood-based tests of new physics”. In: *The European Physical Journal C* 71.2 (2011), pp. 1–19. ISSN: 1434-6052. DOI: `10.1140/epjc/s10052-011-1554-0`.

[Cow56] C. L. Cowan et al. “Detection of the Free Neutrino: a Confirmation”. In: *Science* 124.3212 (1956), pp. 103–104. ISSN: 0036-8075. DOI: `10.1126/science.124.3212.103`.

[Cri11] M. Cribier, M. Fechner, T. Lasserre, et al. “Proposed Search for a Fourth Neutrino with a PBq Antineutrino Source”. In: *Physical Review Letters* 107 (20 2011), p. 201801. DOI: `10.1103/PhysRevLett.107.201801`.

[Dan62] G. Danby, J-M. Gaillard, K. Goulianos, et al. "Observation of High-Energy Neutrino Reactions and the Existence of Two Kinds of Neutrinos". In: *Physical Review Letters* 9 (1 1962), pp. 36–44. DOI: 10.1103/PhysRevLett.9.36.

[Dav68] R. Davis, D. S. Harmer, and K. C. Hoffman. "Search for Neutrinos from the Sun". In: *Physical Review Letters* 20 (21 1968), pp. 1205–1209. DOI: 10.1103/PhysRevLett.20.1205.

[Dod94] S. Dodelson and L. M. Widrow. "Sterile neutrinos as dark matter". In: *Phys. Rev. Lett.* 72 (1 1994), pp. 17–20. DOI: 10.1103/PhysRevLett.72.17.

[Dol16] K. Dolde. "Detector and read-out development to search for sterile neutrinos with KATRIN". MA thesis. Karlsruher Instituts für Technologie, 2016.

[Dos14] N. Doss. "Calculated final state probability distributions for T_2 β-decay measurements". PhD thesis. University College London, 2007.

[Dub91] J. Dubinski and R. G. Carlberg. "The structure of cold dark matter halos". In: *The Astrophysical Journal* 378 (1991), pp. 496–503. ISSN: 0004-637X. DOI: 10.1086/170451.

[Fan47] U. Fano. "Ionization Yield of Radiations. II. The Fluctuations of the Number of Ions". In: *Physical Review* 72 (1 1947), pp. 26–29. DOI: 10.1103/PhysRev.72.26.

[Fer34] E. Fermi. "Versuch einer Theorie der β-Strahlen. I". In: *Zeitschrift für Physik* 88.3 (1934), pp. 161–177. ISSN: 0044-3328. DOI: 10.1007/BF01351864.

[Fis14] S. Fischer. "Commissioning of the KATRIN Raman system and durability studies of optical coatings in glove box and tritium atmospheres". PhD thesis. Karlsruhe Institut für Technologie, 2014.

[Fla03] B. Flatt and J. Wolf. "Design of the KATRIN pre-spectrometer". In: *Nuclear Physics B - Proceedings Supplements* 118 (2003), p. 483. ISSN: 0920-5632. DOI: 10.1016/S0920-5632(03)01373-2.

[For11] J. A. Formaggio and J. Barrett. "Resolving the reactor neutrino anomaly with the KATRIN neutrino experiment". In: *Physics Letters B* 706.1 (2011), pp. 68–71. ISSN: 0370-2693. DOI: 10.1016/j.physletb.2011.10.069.

[Fuk98] Y. Fukuda et al. "Evidence for Oscillation of Atmospheric Neutrinos". In: *Physical Review Letters* 81 (8 1998), pp. 1562–1567. DOI: 10.1103/PhysRevLett.81.1562.

[Gaf15] J. Gaffiot, T. Lasserre, G. Mention, et al. "Experimental Parameters for a Cerium 144 Based Intense Electron Antineutrino Generator Experiment at Very Short Baselines". In: *Physical Review D* 91 (2015). DOI: 10.1103/PhysRevD.91.072005.

[Gan13] A. Gando, Y. Gando, H. Hanakago, et al. "Limit on Neutrinoless $\beta\beta$ Decay of ^{136}Xe from the First Phase of KamLAND-Zen and Comparison with the Positive Claim in ^{76}Ge". In: *Physical Review Letters* 110 (6 2013), p. 062502. DOI: 10.1103/PhysRevLett.110.062502.

[Gev09] O. Gevin et al. "IDeF-X ECLAIRs: An ultra low noise CMOS ASIC for the readout of Cd(Zn)Te Detectors". In: *Transactions on Nuclear Science* 56 (2009), pp. 2351–2359. DOI: 10.1109/TNS.2009.2023989.

[Gil10] W. Gil, J. Bonn, B. Bornschein, et al. “The Cryogenic Pumping Section of the KATRIN Experiment”. In: *IEEE Transactions on Applied Superconductivity* 20.3 (2010), pp. 316–319. ISSN: 1051-8223. DOI: 10.1109/TASC.2009.2038581.

[Giu11] C. Giunti and M. Laveder. “Statistical significance of the gallium anomaly”. In: *Physical Review C* 83 (6 2011), p. 065504. DOI: 10.1103/PhysRevC.83.065504.

[Glu13] F. Glück, G. Drexlin, B. Leiber, et al. “Electromagnetic design of the large-volume air coil system of the KATRIN experiment”. In: *New Journal of Physics* 15.8 (2013), p. 083025. URL: http://stacks.iop.org/1367-2630/15/i=8/a=083025.

[Goo06] A. Goobar et al. “The neutrino mass bound from WMAP 3 year data, the baryon acoustic peak, the SNLS supernovae and the Lyman-α forest”. In: *Journal of Cosmology and Astroparticle Physics* 2006 (2006), p. 019. DOI: 10.1088/1475-7516/2006/06/019.

[Gor12] P. Gorla et al. “The CUORE experiment: status and prospects”. In: *Journal of Physics: Conference Series* 375 (2012), p. 042013. URL: http://stacks.iop.org/1742-6596/375/i=4/a=042013.

[Got94] K. Goto et al. “True Auger spectral shapes: A step to standard spectra”. In: *Surface and Interface Analysis* 22(1-12) (1994), pp. 75–78. DOI: 10.1002/sia.740220119.

[Gro11] S. Grohmann et al. “Precise temperature measurement at 30 K in the KATRIN source cryostat”. In: *Cryogenics* 51.8 (2011), pp. 438–445. ISSN: 0011-2275. DOI: http://dx.doi.org/10.1016/j.cryogenics.2011.05.001.

[Gro15] S. Groh. “Modeling of the response function and measurement of transmission properties of the KATRIN experiment”. PhD thesis. Karlsruher Instituts für Technologie, 2015.

[Hac15] M. Hackenjos. “Die differentielle Pumpstrecke des KATRIN-Experiments- Inbetriebnahme und Charakterisierung des supraleitenden Magnetsystems”. MA thesis. Karlsruhe Institut für Technologie, 2015.

[Hor14] S. Horiuchi, P. J. Humphrey, et al. “Sterile neutrino dark matter bounds from galaxies of the Local Group”. In: *Physical Review D* 89 (2 2014), p. 025017. DOI: 10.1103/PhysRevD.89.025017.

[Hub15] A. Huber. “Search for keV-Scale Sterile Neutrinos with KATRIN”. MA thesis. Karlsruher Instituts für Technologie, 2015.

[Jan15] A. Jansen. “The cryogenic pumping section of the KATRIN experiment - Design studies and experiments for the commissioning”. PhD thesis. Karlsruhe Institut für Technologie, 2015.

[Kam16] KamLAND-Zen Collaboration. “Search for Majorana Neutrinos near the Inverted Mass Hierarchy region with KamLAND-Zen”. In: (2016). eprint: arXiv:1605.02889.

[Kle14] M. Kleesiek. “A Data-Analysis and Sensitivity-Optimization Framework for the KATRIN Experiment”. PhD thesis. Karlsruhe Institut für Technologie, 2014.

[Kly99] A. Klypin et al. "Where Are the Missing Galactic Satellites?" In: *The Astrophysical Journal* 522 (1999), p. 82. DOI: 10.1086/307643.

[Kod01] K. Kodama et al. "Observation of tau neutrino interactions". In: *Physics Letters B* 504.3 (2001), pp. 218–224. ISSN: 0370-2693. DOI: 10.1016/S0370-2693(01)00307-0.

[Kra05] Ch. Kraus, B. Bornschein, L. Bornschein, et al. "Final results from phase II of the Mainz neutrino mass searchin tritium β decay". In: *The European Physical Journal C - Particles and Fields* 40.4 (2005), pp. 447–468. ISSN: 1434-6052. DOI: 10.1140/epjc/s2005-02139-7.

[Lim11] O. Limousin. *IDeF-X, une technologie française de pointe exportée aux U.S.A.* 2011. URL: http://irfu.cea.fr/Sap/Phocea/Vie_des_labos/Ast/ast.php?t=actu&id_ast=3071 (visited on 05/07/2016).

[Lov12] M. R. Lovell, V. Eke, C. S. Frenk, et al. "The Haloes of Bright Satellite Galaxies in a Warm Dark Matter Universe". In: *Monthly Notices of the Royal Astronomical Society* 420 (2012), pp. 2318–2324. DOI: 10.1111/j.1365-2966.2011.20200.x.

[Mak62] Z. Maki, M. Nakagawa, and S. Sakata. "Remarks on the Unified Model of Elementary Particles". In: *Progress of Theoretical Physics* 28 (1962), pp. 870–880. DOI: 10.1143/PTP.28.870.

[Mat02] K. Mathiesona et al. "Charge sharing in silicon pixel detectors". In: *Nuclear Instruments and Methods in Physics Research Section A: Accelerators, Spectrometers, Detectors and Associated Equipment* 487 (2002), pp. 113–122. ISSN: 0168-9002. DOI: 10.1016/S0168-9002(02)00954-3.

[Men11] G. Mention, M. Fechner, Th. Lasserre, et al. "Reactor antineutrino anomaly". In: *Physical Review D* 83 (7 2011), p. 073006. DOI: 10.1103/PhysRevD.83.073006.

[Mer15a] S. Mertens, T. Lasserre, S. Groh, et al. "Sensitivity of next-generation tritium beta-decay experiments for keV-scale sterile neutrinos". In: *Journal of Cosmology and Astroparticle Physics* 2015.02 (2015), p. 020. DOI: 10.1088/1475-7516/2015/02/020.

[Mer15b] S. Mertens, K. Dolde, M. Korzeczek, et al. "Wavelet approach to search for sterile neutrinos in tritium β-decay spectra". In: *Phys. Rev. D* 91 (4 2015), p. 042005. DOI: 10.1103/PhysRevD.91.042005.

[Mic10] A. Michalowska et al. "IDeF-X HD: A low power Multi-Gain CMOS ASIC for the readout of CD(Zn)Te Detectors". In: *Nuclear Science Symposuim & Medical Imaging Conference* (2010), pp. 1556–1559. DOI: 10.1109/NSSMIC.2010.5874037.

[Mik86] S. P. Mikheev and A. Y. Smirnov. "Resonance Amplification of Oscillations in Matter and Spectroscopy of Solar Neutrinos". In: *Soviet Journal of Nuclear Physics* 42 (1985), pp. 913–917.

[Nav96] J. F. Navarro, C. S. Frenk, and S. D. M. White. "The Structure of Cold Dark Matter Halos". In: *The Astrophysical Journal* 462 (1996), pp. 563–575. DOI: 10.1086/177173.

[Nav97] J. F. Navarro, C. S. Frenk, and S. D. M. White. “A Universal Density Profile from Hierarchical Clustering”. In: *The Astrophysical Journal* 490 (2 1997), p. 493. DOI: 10.1086/304888.

[Nob16] Nobel Media. *Official Nobel Prize web site*. URL: http://www.nobelprize.org/nobel_prizes/physics/laureates/1988/ (visited on 05/11/2016).

[Ohs11] S.-H. Oh, W. J. G. de Blok, E. Brinks, et al. “Dark and Luminous Matter in THINGS Dwarf Galaxies”. In: *The Astronomical Journal* 141.6 (2011), p. 193. DOI: 10.1088/0004-6256/141/6/193.

[Oli14] K. A. Olive et al. “Review of Particle Physics”. In: *Chin. Phys.* C38 (2014), p. 090001. DOI: 10.1088/1674-1137/38/9/090001.

[Pau30] W. Pauli. *Scientific Correspondence with Bohr, Einstein, Heisenberg a.o. Volume II: 1930–1939*. Meyenn, K.v., 1985. ISBN: 978-3-540-78801-0.

[Pon57] B. Pontecorvo. “Mesonium and anti-mesonium”. In: *Soviet Physics Journal of Experimental and Theoretical Physics* 6 (1957), p. 429. URL: http://www.jetp.ac.ru/files/pontecorvo1957_en.pdf.

[Pri15] F. Priester, M. Sturm, and B. Bornschein. “Commissioning and detailed results of KATRIN inner loop tritium processing system at Tritium Laboratory Karlsruhe”. In: *Vacuum* 116 (2015), pp. 42–47. ISSN: 0042-207X. DOI: 10.1016/j.vacuum.2015.02.030.

[Ren11] P. Renschler. “KESS - A new Monte Carlo simulation code for low-energy electron interactions in silicon detectors”. PhD thesis. Karlsruher Instituts für Technologie, 2011.

[Rii11] A. S. Riis and S. Hannestad. “Detecting sterile neutrinos with KATRIN like experiments”. In: *Journal of Cosmology and Astroparticle Physics* 2011.02 (2011), p. 011. DOI: 10.1088/1475-7516/2011/02/011.

[Roe11] M Röllig. “Studien zu einem Röntgendetektorsystem zur Überwachung der KATRIN Tritiumquelle”. MA thesis. Karlsruhe Institut für Technologie, 2011.

[Roe13] M. Röllig, F. Priester, M. Babutzka, et al. “Activity monitoring of a gaseous tritium source by beta induced X-ray spectrometry”. In: *Fusion Engineering and Design* 88.6–8 (2013), pp. 1263–1266. ISSN: 0920-3796. DOI: 10.1016/j.fusengdes.2012.11.001.

[Sae00] A. Saenz, S. Jonsell, and P. Froelich. “Improved Molecular Final-State Distribution of HeT^{+} for the β-Decay Process of T_2”. In: *Physical Review Letters* 84 (2000), p. 242. DOI: 10.1103/PhysRevLett.84.242.

[Sch13] M. Schlösser, H. Seitz, S. Rupp, et al. “In-Line Calibration of Raman Systems for Analysis of Gas Mixtures of Hydrogen Isotopologues with Sub-Percent Accuracy”. In: *Analytical Chemistry* 85.5 (2013), pp. 2739–2745. DOI: 10.1021/ac3032433.

[Sch14] J. Schwarz. “The detector system of the KATRIN experiment - Implementation and first measurements with the spectrometer”. PhD thesis. Karlsruhe Institut für Technologie, 2014.

[Sch16] A. Schneider. "Astrophysical constraints on resonantly produced sterile neutrino dark matter". In: (2016). eprint: arXiv:1601.07553.

[Spr05] V. Springel, S. D. M. White, A. Jenkins, et al. "Simulations of the formation, evolution and clustering of galaxies and quasars". In: *Nature* 435 (2005), pp. 629–636. ISSN: 0028-0836. DOI: 10.1038/nature03597.

[Stu10] M. Sturm. "Aufbau und Test des Inner-Loop-Systems der Tritiumquelle von KATRIN". PhD thesis. Karlsruher Instituts für Technologie, 2010.

[Tre79] Scott Tremaine and James E. Gunn. "Dynamical Role of Light Neutral Leptons in Cosmology". In: *Physical Review Letters* 42 (6 1979), pp. 407–410. DOI: 10.1103/PhysRevLett.42.407.

[Ubi09] M. Ubieto-Díaz, D. Rodríguez, S. Lukic, et al. "A broad-band FT-ICR Penning trap system for KATRIN". In: *International Journal of Mass Spectrometry* 288.1–3 (2009), pp. 1–5. ISSN: 1387-3806. DOI: 10.1016/j.ijms.2009.07.003.

[Val10] K. Valerius. "The wire electrode system for the KATRIN main spectrometer". In: *Progress in Particle and Nuclear Physics* 64.2 (2010), pp. 291–293. ISSN: 0146-6410. DOI: 10.1016/j.ppnp.2009.12.032.

[Val11] K. Valerius, H. Hein, H. Baumeister, et al. "Prototype of an angular-selective photoelectron calibration source for the KATRIN experiment". In: *Journal of Instrumentation* 6.01 (2011), P01002. DOI: 10.1088/1748-0221/6/01/P01002.

[Vie13] M. Viel, G. D. Becker, J. S. Bolton, et al. "Warm dark matter as a solution to the small scale crisis: New constraints from high redshift Lyman-α forest data". In: *Physical Review D* 88 (4 2013), p. 043502. DOI: 10.1103/PhysRevD.88.043502.

[Wan09] N. Wandkowsky. "Design and Background Simulations for the KATRIN Main Spectrometer and Air Coil System". MA thesis. Karlsruhe Institut für Technologie, 2009.

[Win11] A. Windberger. "Berechnungen und Simulationen zum Verhalten von Ionen in der differenziellen Pumpstrecke des KATRIN-Experiments". MA thesis. Karlsruhe Institut für Technologie, 2011.

[Wol78] L. Wolfenstein. "Neutrino oscillations in matter". In: *Physical Review D* 17 (9 1978), pp. 2369–2374. DOI: 10.1103/PhysRevD.17.2369.

[Xu15] W. Xu, N. Abgrall, F. T. Avignone III, et al. "The Majorana Demonstrator: A Search for Neutrinoless Double-beta Decay of 76 Ge". In: *Journal of Physics: Conference Series* 606.1 (2015), p. 012004.

[Zbo13] M. Zbořil, S. Bauer, M. Beck, et al. "Ultra-stable implanted 83 Rb/ 83 m Kr electron sources for the energy scale monitoring in the KATRIN experiment". In: *Journal of Instrumentation* 8.03 (2013), P03009. DOI: 10.1088/1748-0221/8/03/P03009.

A. Analysis method for maximal impact estimation of eV-scale sterile neutrinos

In the fit the mixing angle was limited to: $\sin^2(\theta) < 0.5$. [1] Furthermore the fitter found different minima depending on the initial value of the nuisance parameters for the fit. Thus to ascertain a global minimum, for the mass sensitivity simulation, the fit was repeated over 1000 times with random initial nuisance parameters for each point of $\chi^2(m^2_{\mathrm{eff}})$.

$$\begin{aligned} N &= |N_0 - \nu_{\mathrm{p,N}}| && \text{uniform in } -1 < \nu_{\mathrm{p,N}}/N_0 < 1 \\ B &= |B_0 - \nu_{\mathrm{p,B}}| && \text{uniform in } -0.5 < \nu_{\mathrm{p,B}}/B_0 < 0.5 \\ Q &= |Q_0 - \nu_{\mathrm{p,Q}}| && \text{uniform in } -0.5 < \nu_{\mathrm{p,Q}}/Q_0 < 0.5 \end{aligned} \tag{A.1}$$

N_0, B_0 and Q_0 denote the reference values for the simulated parameters, e.g. $B_0 = 10\,\mathrm{mcps}$. The nuisance parameters allow to probe the region around the reference values.

In figure A.1 the repeated initialization of 1000 times to search for a global minimum is depicted. The histogram displays three major local minima found by the fitter. The global minimum is located at roughly $\chi^2 = 0.7$. In the analysis procedure, this global minimum would corresponds to a single point of $\chi^2(m^2_{\mathrm{eff}})$ in figure 3.1.

[1] If $\sin^2\theta$ is not constrained, then the fitter will find a minimum for χ^2 at $\sin^2\theta = 1$ and thus neglect the active neutrino branch.

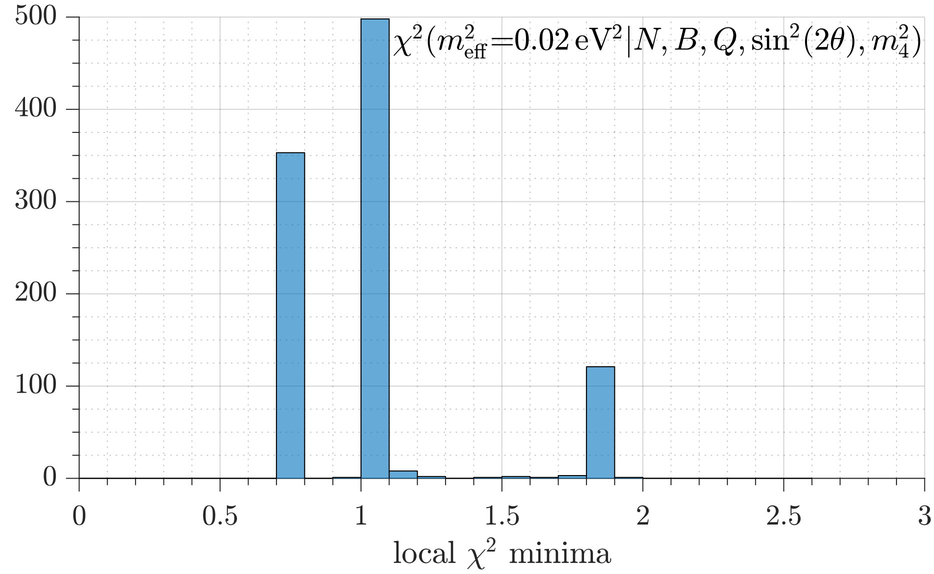

Figure A.1.: Result of 1000 χ^2 evaluations with random initialization of nuisance parameters.

B. Backscattering simulations with KESS

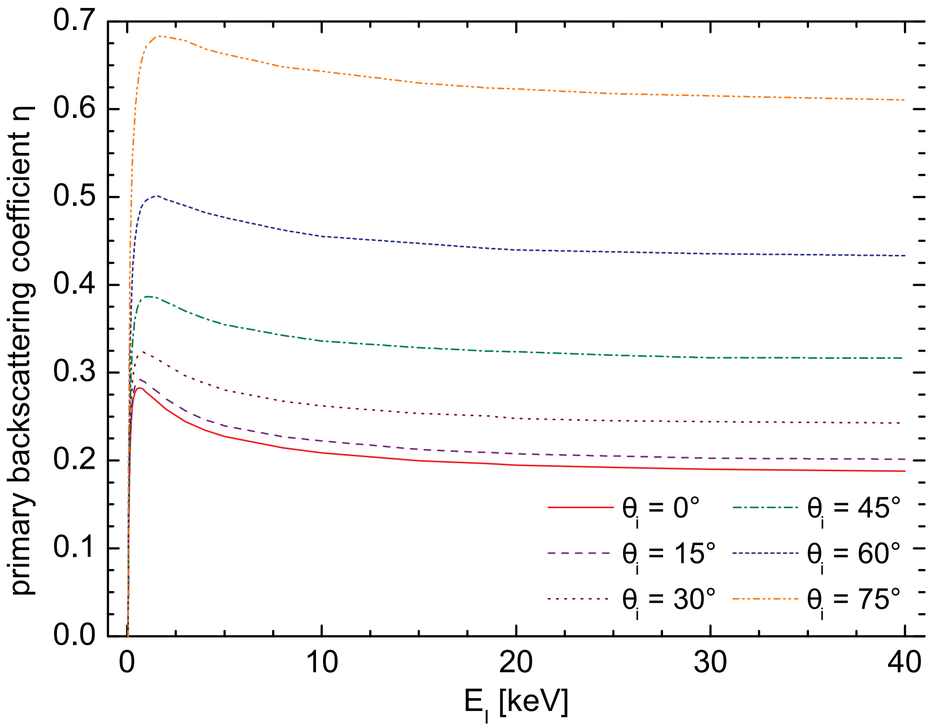

Figure B.1.: The primary backscattering coefficient η for electron incidence on silicon calculated with KESS. η is for incident energies $E_I < 40\,\text{keV}$ and incident angles $\theta_I < 75°$. [Ren11]

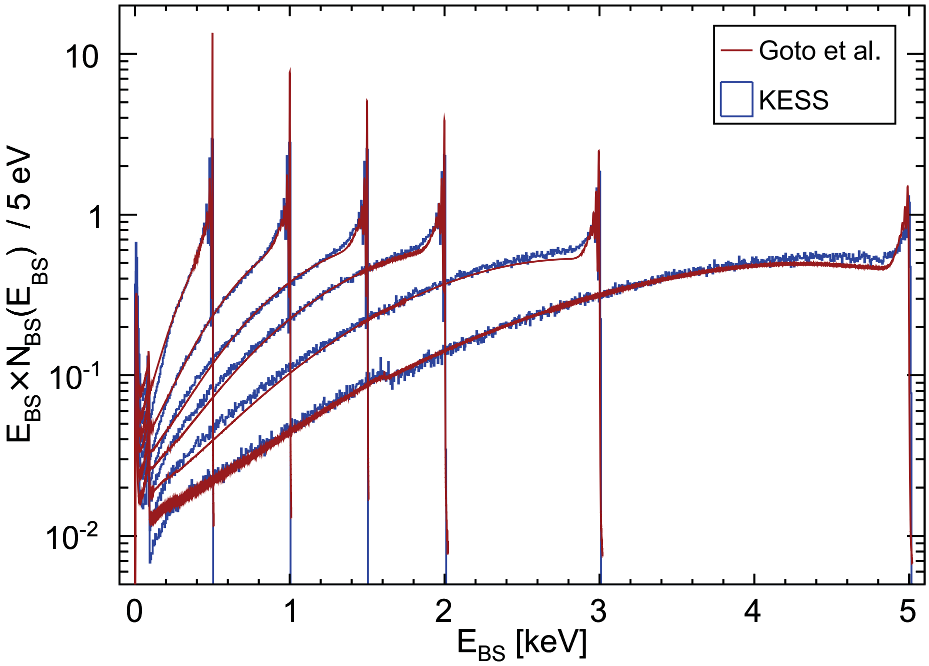

Figure B.2.: Energy spectrum of backscattered electrons in dependence on the electron incident energy $E_\mathrm{I} = 0.5, 1, 1.5, 2, 3, 5\,\mathrm{keV}$ for normal incidence. KESS results obtained with Penn's inelastic collision cross sections, and knock-on secondary angle model based on spherical symmetry (SPS) are compared to measurements from [Got94]. [Ren11]

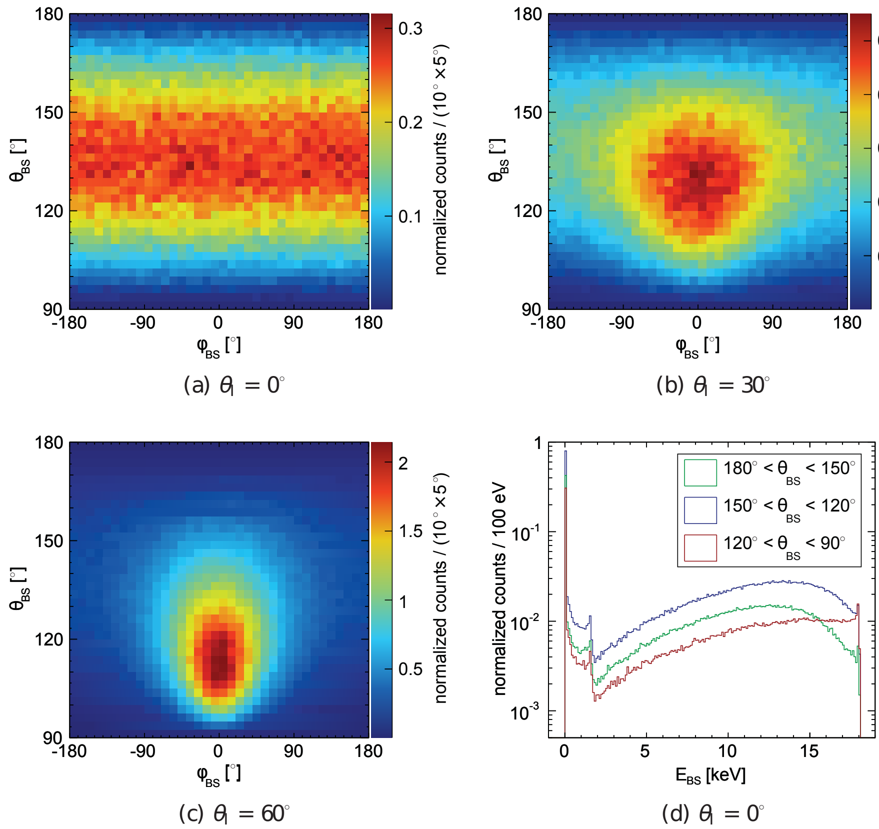

Figure B.3.: Angular distribution of backscattered electrons for an electron beam with incident energy $E_I = 18$ keV, azimuthal incident angle $\varphi_I = 0°$ and polar incident angle (a)+(d) $\theta_I = 0°$, (b) $\theta_I = 30°$ and (c) $\theta_I = 60°$. All plots are normalized to the number of incident electrons N_I. In (a)-(c) the polar angle of backscattered electrons θ_{BS} is plotted over the azimuthal angle φ_{BS}. (d) The energy spectrum of backscattered electrons with respect to their polar angle θ_{BS} for $\theta_I = 0°$. It can be concluded from (d) that primary electrons are preferentially scattered into shallow θ_{BS}. [Ren11]